Shear strength of saturated sand-steel interfaces

Geotechnical issues found at landfall operations

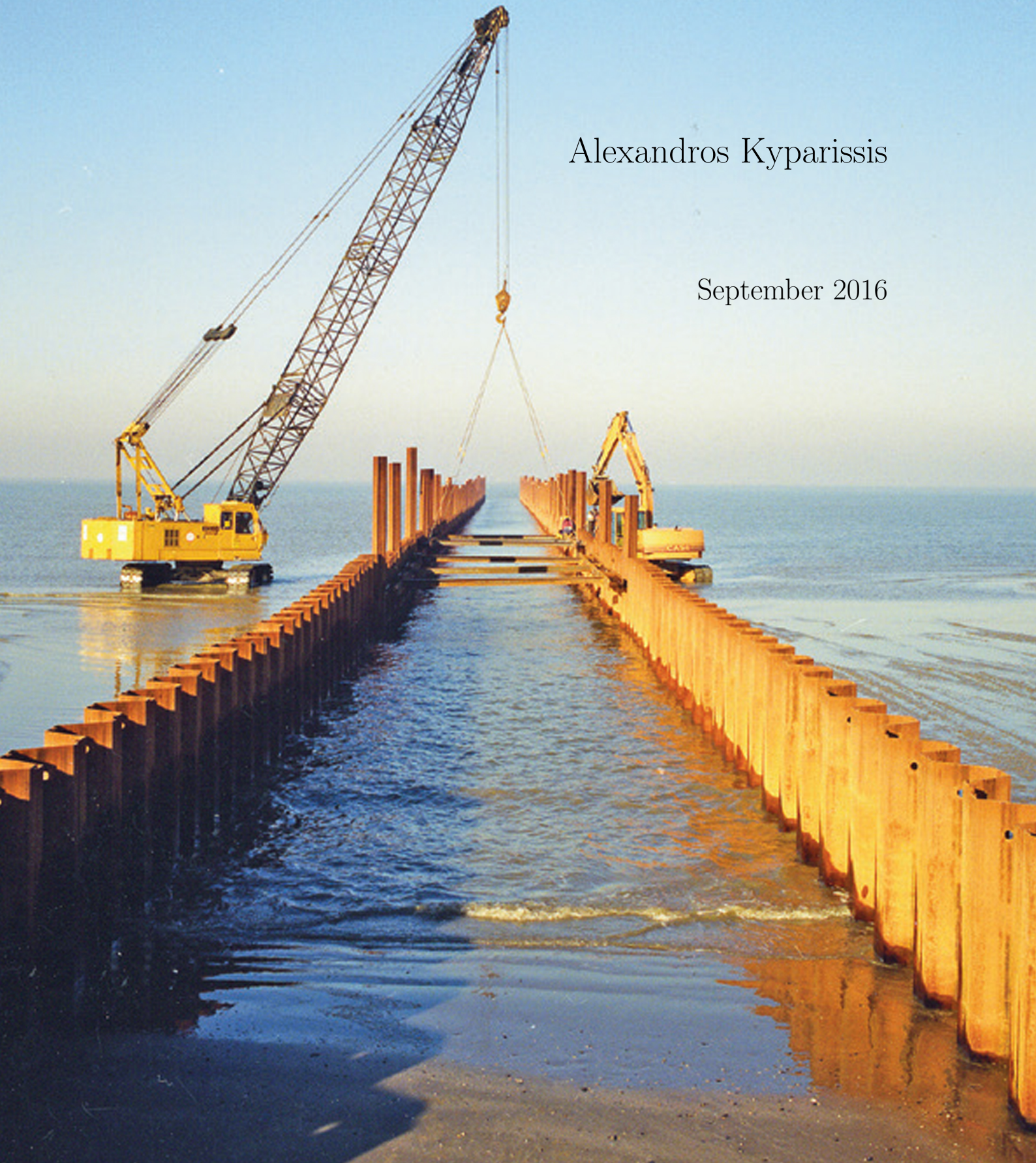

Alexandros Kyparissis

September 2016

The cover image is courtesy of Jan De Nul Group and depicts the construction of a mechanically retained wall.

Shear strength of saturated sand-steel interfaces

Geotechnical issues found at landfall operations

by

Alexandros Kyparissis

to obtain the degree of Master of Science
at the Delft University of Technology,
to be defended publicly on Tuesday September 20, 2016 at 16:00 PM.

Student number:	4405919	
Project duration:	November 9, 2015 – September 20, 2016	
Thesis committee:	Dr. A. Askarinejad	TU Delft, supervisor
	Prof. Dr. M.A. Hicks	TU Delft, head of committee
	Dr. Ir. D.J.M. Ngan-Tillard	TU Delft, supervisor
	Dr. F. Pisanò	TU Delft, supervisor
	Ir. H.J. van der Waa	Allseas Engineering BV, supervisor

Shear strength of saturated sand-steel interfaces

Geotechnical issues found at landfall operations

Alexandros Kyparissis

Abstract

Landfall operations are conducted for connecting an offshore pipeline with process facilities on the shore. During a landfall operation an offshore pipeline is pulled by means of a steel wire rope on the shore with a velocity of 7 cm/s. During this process the steel wire rope interacts with the soil located on the seabed and on the shore. Allseas Engineering BV has a long experience on landfall operations and it was occasionally noticed that the steel wire ropes were buried beneath sand dunes which resulted from sedimentation and wave actions. In these instances excessive pulling forces were required to mobilise the steel wire ropes.

A prototype experimental setup was developed for simulating the pulling process in medium scale. Physical modelling involved the pulling of a steel element through saturated sand with a relative density of 80%. The aim of this apparatus was to examine the shear failure mechanisms that develop in saturated sand while a steel pipe, with a significantly rough surface, is pulled through it. The main focus points of this study were the peak pulling force of the steel pipe and the change of pore pressures around the steel pipe's circumference during the pulling process. The latter two were examined with respect to six burial depths (0 - 0.31 m) and three pulling velocities (1, 4 and 7 cm/s).

It was observed that at every test a momentary decrease of pore pressures was taking place around the steel pipe during the pulling process. A peak was always recorded at the same time as the peak pulling force and this was attributed to the tendency of sand particles to dilate around the steel pipe. Undrained loading conditions were caused by the high pulling velocities and low permeability of the soil. Therefore, dilation was restrained by the pore water and consequently tensile pore pressures developed which increased the shear strength of the soil, momentarily.

Burying the steel pipe at different depths influenced, as it was expected, the peak pulling force due to the increase of the vertical effective stresses. In addition, the peak decrease of pore pressures was found to increase in magnitude while the burial depth ranged from 0 to 0.09 m and this was an unexpected event as the tendency of the soil to dilate was expected to be restrained. The magnitude of peak pore pressure decrease was also found to reduce at burial depths ranging from 0.09 m to 0.31 m due to the increase of vertical effective stresses that restrained the soil's tendency to dilation.

The effect of pulling velocity to the peak pulling force and the peak pore pressure reduction values was also examined. The latter were found to increase linearly with the increase of pulling velocity, at each burial depth that was tested. Also, the peak pulling forces were found to increase linearly while comparing tests at the same burial depth, conducted with different pulling velocities. In addition, the increase of pulling velocity caused a linear increase on the stiffness index of the test specimens.

The scientific significance of the results of the current study can assist to performing landfall operations in a more efficient way. It is recommended that during a landfall operation the initiation of the pulling of the steel wire rope should take place at the lowest possible rate. As a result, the maximum pulling force will be minimised and the pulling velocity can be increased gradually once the steel wire rope is mobilised. Moreover, the findings of this study can be useful for the (un-)installation of (offshore) piles, sheet pile walls, soil nails and dredging operations on saturated sands.

Acknowledgements

I would like to thank Dr. Ir. Dominique Ngan-Tillard for her continuous support throughout all the stages of this project. Her advice has been vital for progressing efficiently through all the steps of my thesis. In addition, her recommendations on the theoretical and experimental part of this study helped me produce a detailed connection between the theory and the experimental results. Also, her assistance on procedural matters was indispensable for completing this thesis.

Moreover, I feel thankful for the assistance of Dr. Amin Askarinejad on designing and organising my experimental apparatus. His immense knowledge of experimental soil mechanics inspired me to develop an extensive experimental programme and accurate experimental procedures. Also, his assistance on analysing the experimental results was vital for yielding accurate conclusions.

In addition, I am grateful for the assistance that I have received by Prof. Michael Hicks and Dr. Federico Pisanò on the theoretical part of this study and their sound recommendations regarding the soil mechanisms that developed in my experiments.

Furthermore, I would like to thank Kees van Beek (TU Delft) and Han de Visser (TU Delft) for their advice on designing the testing tank. In addition, Kees' unique skills were vital for embedding the pressure transducers in the steel pipe.

I would also like to acknowledge the permission given by the Geo-Engineering Section to conduct my experiments in their laboratory. Also, I would like to thank Arno Mulder (TU Delft) who was always enthusiastic and keen to help with any matter in the laboratory and assist with the transportation of my experimental apparatus.

Plenty of people from Allseas Engineering BV played a key role on the completion of this project. Firsly, I would like to thank my daily supervisor, Hester van der Waa, for her support throughout all the stages of this project. Secondly, I am grateful for the help I received by Adrian Singuran for designing and constructing the electronic apparatus. Lastly, I would like to thank Paul Meijer for his support on producing the drawings of the testing tank.

Finally, I would like to express my gratitude to my family and friends for their patience and unconditional support.

Alexandros Kyparissis

Contents

List of Figures

List of Tables

Nomenclature

Upper case latin symbols

A_{n}	[m^2]	Area of steel element interacting with the soil
C_{c}	[-]	Coefficient of curvature
C_{u}	[-]	Coefficient of uniformity
D	[m]	Diameter of steel element
D_{10}	[m]	Maximum diameter of the smallest 10% of the soil sample
D_{30}	[m]	Maximum diameter of the smallest 30% of the soil sample
D_{50}	[m]	Maximum diameter of the smallest 50% of the soil sample
D_{60}	[m]	Maximum diameter of the smallest 60% of the soil sample
E	[Pa]	Young's Modulus
E_{ref}	[Pa]	Reference Young's modulus
F_{c}	[N]	Rope curvature force component
F_{w}	[N]	Rope self-weight force component
F_{Δ}	[N]	Burial depth force component
F_{Ψ}	[N]	Interface dilation force component
G	[Pa]	Shear modulus
G_{s}	[-]	Specific gravity
I_{D}	[-]	Relative density
K_0	[-]	Earth pressure at rest
P_{mat}	[-]	Percentage of the sliding surface that runs over the steel element
P_{sand}	[-]	Percentage of the sliding surface that runs through sand
R_{a}	[m]	Average roughness
R_{n}	[-]	Normalised roughness
T_{f}	[N]	Final calculated peak pulling force
T_{max}	[N]	Maximum calculated pulling force

Lower case latin symbols

d	[m]	Burial depth
e	[-]	Void ratio
$e_{\max}$	[-]	Maximum void ratio
$e_{\min}$	[-]	Minimum void ratio
i	[°]	Inclination of indentations on rough steel surfaces
$k_{\max}$	[m/s]	Maximum soil permeability
$k_{\min}$	[m/s]	Minimum soil permeability
l_e	[m]	Effective length of steel element
m	[-]	Power in stress-dependent stiffness relation
p'_{ref}	[Pa]	Reference pressure
$q'_{\max}$	[Pa]	Dilation modulus
r_0	[m]	Radius of steel element
t	[m]	Shear zone thickness
u_1	[Pa]	Hydrostatic pore pressures
u_2	[Pa]	Pore pressures during shearing
u_c	[m]	Critical shear displacement
v_{pull}	[m/s]	Pulling velocity

Upper case Greek symbols

Δt	[m]	Chang of shear zone thickness
Δu	[Pa]	Change of pore pressures
$-\Delta u_{\max}$	[Pa]	Maximum decrease of pore pressures

Lower case Greek symbols

γ'	[N/m^3]	Effective unit weight
$\delta_{p,l}$	[°]	Peak interface friction angle at low normal stresses
$\delta_{p,h}$	[°]	Peak interface friction angle at high normal stresses
$\delta_{r,l}$	[°]	Residual interface friction angle at low normal stresses
$\delta_{r,h}$	[°]	Residual interface friction angle at high normal stresses
δ_s	[°]	Micro-facets and soil interface friction angle
θ	[°]	Angle with respect to the horizontal axis
μ	[-]	Friction coefficient
ν	[-]	Poisson's ratio
ξ	[-]	Interface dilation angle
ρ_{max}	[kg/m^3]	Maximum soil density
ρ_{min}	[kg/m^3]	Minimum soil density
σ'_3	[Pa]	Horizontal effective stress
$\sigma_{N,bottom}$	[Pa]	Effective stress acting on the bottom semicircle
$\sigma_{N,top}$	[Pa]	Effective stress acting on the top semicircle
σ'_v	[Pa]	Vertical effective stress
$\sigma'_{v,pwp}$	[Pa]	Effective stress induced by pore pressure reduction
$\phi_{p,l}$	[°]	Peak angle of internal friction at low normal stresses
$\phi_{p,h}$	[°]	Peak angle of internal friction at high normal stresses
$\phi_{r,l}$	[°]	Residual angle of internal friction at low normal stresses
$\phi_{r,h}$	[°]	Residual angle of internal friction at high normal stresses
ψ	[°]	Dilation angle

Abbreviations

ALO	Steel plate blasted with aluminium oxide
DAS	Data acquisition system
DS	Direct shear
F1	First foundation layer
F2	Second foundation layer
GND	Steel plate ground with grinding wheel
IWRC	Independent wire rope core
MGS	Steel plate with medium sand particles glued on its surface
PPT	Pore pressure transducers
PVC	Polyvinyl chloride
S0	Soil layer located at the heigh of the steel pipe
S1	First soil layer on top of the steel pipe
S2	Second soil layer on top of the steel pipe
S3	Third soil layer on top of the steel pipe
SFS	Steel plate with fine sand particles glued on its surface
VLB	Steel plate with coarse sand particles glued on its surface

Chapter 1

Introduction

During landfall operations a steel wire rope (SWR) is used to pull an offshore pipeline on the shore. During these operations the SWR interacts with the soil found on the seabed and in some cases this resulted in excessive pulling forces and deformations on the SWR. The geotechnical issues met at landfall operations analysed in this study are introduced in this chapter. Information regarding the causes of the problem is provided and a research approach is proposed. Finally, the document's layout is described.

1.1 Background information

1.1.1 Landfall operations

The construction of offshore pipelines involves multiple challenging stages and one of these is met when a pipeline has to be connected with the facilities onshore. Pipe-lay vessels that are used at large water depths cannot reach near the shore due to depth restrictions. The operation of these vessels involves the welding and construction of the final components of the pipeline. The final part of the pipeline is then pulled onshore using SWRs and thereafter is connected to other industrial equipment. This pulling process is widely known in the offshore industry as "landfall operation" and it is illustrated in Figure 1.1.

Figure 1.1: Landfall operation through a mechanically retained trench, July 2010, Germany (Nord Stream AG)

Landfall operations involve multiple phases for their completion. As illustrated in Figure 1.2, when the offshore pipeline reaches near the shore a SWR is attached to it. The path that is followed by the SWR and the pipeline firstly involves the seabed. In some cases the SWR and pipeline are pulled inside a micro-tunnel (Figure 1.2) or, in other cases, through a trench that is dredged and retained open mechanically (Figure 1.1).

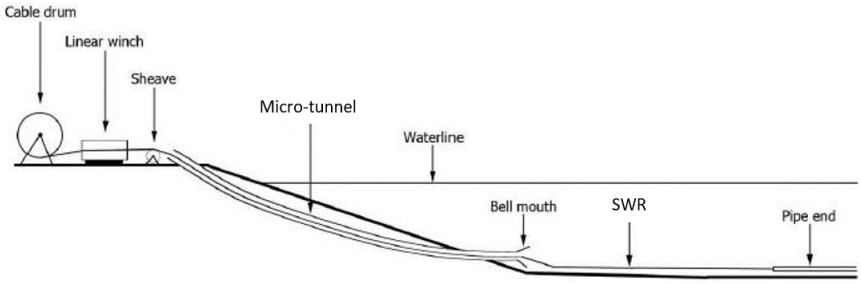

Figure 1.2: Landfall operation through a micro-tunnel [4]

The pulling setup that is used at landfall operations includes initially a sheave that assists with the normalisation of the SWR inclination. Once the pulling line is situated horizontally, it is then pulled by a linear winch, which ensures a stable and fully controlled pulling process. Finally, the SWR is collected on a storage winch. When the pipeline has reached on the shore it is welded, bolted and connected to the awaiting facilities onshore.

Finally, in other occasions a pipeline can be constructed in parts onshore and then pulled into the sea by the pipe-lay vessel through trenches or conduits. This process has some aspects in common with the process described above. The content of this study concentrates solely on instances that a pipeline is pulled on the shore through a mechanically retained trench.

1.1.2 Previous experience

Allseas is a world-wide leader in offshore pipeline installation and subsea construction. Multiple pipe-laying projects have been conducted in the past with great success. However, issues have aroused with landfall operations during two projects, where unexpected excessive pulling forces were observed. Firstly, at the development of Shell Corrib project which is located at North-West Ireland and secondly at the development of Noble Tamar field, located in Israel. Consequently, these issues have caused project delays and therefore Allseas aims for improving the prediction of the required pulling forces needed for conducting efficient landfall operations. The improvement of the forces' prediction is aimed to be achieved by understanding the causes of the excessive pulling forces.

1.1.3 Steel wire ropes

In general, SWRs that are used at landfall operations consist of an independent wire rope core (IWRC) and multiple strand cables that surround it, forming a helical shape. The core and strand cable also consist of smaller steel wires that are bound together, also forming a helical layout as depicted in Figure1.3.

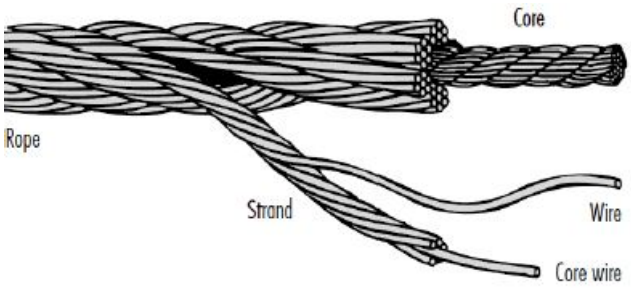

Figure 1.3: Internal structure of SWRs, illustrating the core, strands and wires [4]

The direction at which the strand wires are laid with respect to the core can differ

resulting into different "types of lay". The most common type of lay found in the industry is when the strand wires develop the helical shape in the opposite direction to the direction at which the strands have been laid, as illustrated in Figure 1.3. This type of lay is known as "ordinary lay" and the strand wires are in general aligned with the lay of the SWR. Another type of lay, known as "Lang's lay", consists of both the strands and strand wires being laid in the same direction. In the case of Lang's lay, the strand wires are set to a 45° angle with respect to the laying line of the SWR. In some instances the strands are wound around the core to the right and in other instances to the left, resulting in "Right-Hand Lay" and "Left-Hand Lay", respectively.

The SWRs used by Allseas at landfall operations usually consist of 6 or 8 strands with an ordinary lay and an independent core wire. The usual diameter used in landfall operation most of times ranges roughly between 60 mm and 80 mm. The steel wire ropes used at the Shell Corrib and Noble Tamar projects are illustrated in Figure 1.4. The technical specifications can be found in Table 1.1.

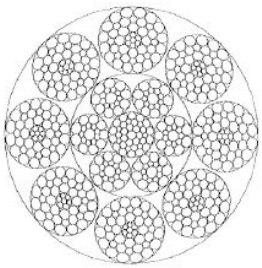

(a) Shell Corrib project

(b) Noble Tamar project

Figure 1.4: Internal structure of SWRs used in previous projects [4]

Table 1.1: Technical specifications of SWRs used in Shell Corrib and Noble Tamar

	Projects	
Specifications	**Shell Corrib**	**Noble Tamar**
Diameter [mm]	83	77
Strands	8 outer strands 47 wires each	6 outer strands 36 wires each
Lay type	Right-hand ordinary lay	Right-hand ordinary lay
IWRC - strands	8 strands 19 wires per strand	6 strands 7 wires per strand
IWRC - core	36 wires	7 wires
Minimum Breaking Load [ton]	550	486
Tensile strength [MPa]	1960	1960

Finally, it has to be noted that when SWRs are subjected to tension they tend to rotate due to their helical structure. The tensile load is therefore transformed to torsional and as a result the strands are separated and untwisted.

1.2 Problem definition

The problem of excessive pulling forces can be divided into more subcategories as illustrated in Figure 1.5. Based on conclusions drawn by [14] and [4], it is expected that

the excessive pulling forces can be attributed to both the behaviour of soil and the SWR during pulling.

Based on the behaviour of the SWRs, there are two mechanisms that develop during the pulling process and therefore contribute to the excessive pulling forces. The first mechanism involves the transformation of the tensile load to torsional which, as explained earlier, causes the untwisting of the SWR's strands and the rotation of the system. The deformations that the SWR undergoes result in local increases of its nominal diameter and therefore the increase of the system's pulling force. The second mechanism is developed due to the resistance that is caused on the sand-steel interface while the SWR is rotated. The screwing effect could cause hockling, bird-caging and occasionally breakage of the IWRC.

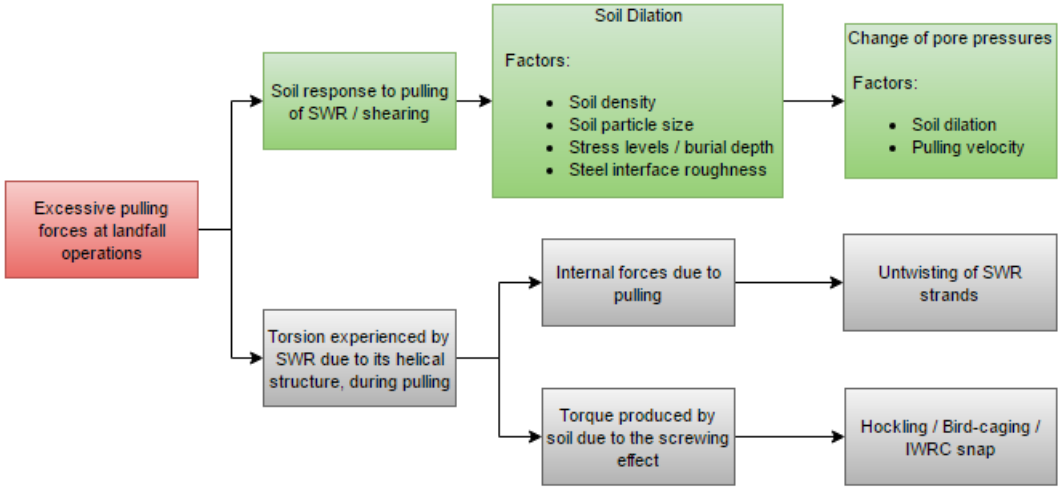

Figure 1.5: Excessive pulling forces, problem break-down

The tendency of the soil to dilate located around the SWR could be another reason that high pulling forces are required during the pulling operation. The pulling process is expected to take place in undrained loading conditions due to the high pulling velocity and low soil permeability.

As it is shown in Figure 1.6a, dense soils tend to dilate when subjected to shear loads and become loose. In case a shear strain is applied rapidly (i.e. 7 cm/s) then the dilation is suppressed due to the pore water being incompressible, as it is shown in Figure 1.6b. The latter effect is also reinforced in case the soil's permeability is relatively low. The soil grains tend to dilate, however the pore water does not allow any volume changes to take place. As a consequence, tensile stresses develop in the pore water and therefore the vertical effective stresses and the shear strength of the soil are increased.

The above-mentioned failure mechanism is also expected to take place around the external surface of a SWR's. At the projects where excessive pulling forces were observed during the landfall operations (Shell Corrib and Noble Tamar) the dominant soil conditions constituted of fine dense sand deposits.

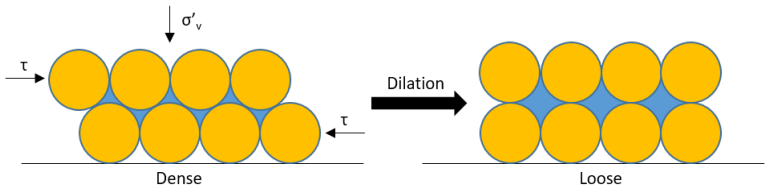

(a) Drained conditions

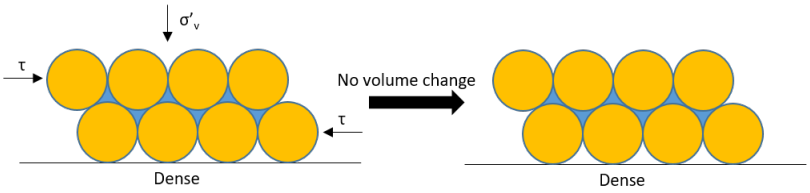

(b) Undrained conditions

Figure 1.6: Response of a dense saturated soil to shear load

1.3 Research questions

The influence of the soil response on the pulling forces was decided to be examined purely with experimental methods. An prototype experimental setup can produce data suitable for examining the soil mechanisms on sand-steel interface during undrained loading. Therefore, the main research question of the current study is:

- *What are the soil phenomena that develop during the pulling of the SWR and how do they affect the resulting pulling forces?*

The main research question will be answered using three sub-questions that assist to breaking down the problem in separate focus points.

- *What **test setup** can simulate the problem so that influencing parameters can be varied and their effects can be measured?*
- *Does the **sand's tendency to dilate** have an impact on the pulling forces and what soil parameters influence its magnitude?*
- *Do **pore pressures** on the sand-steel interface decrease during the pulling operation and, if yes, what soil parameters influence their magnitude?*

1.4 Thesis layout

Chapter 2 describes the theoretical background of this study. References are made to the behaviour of sand during shearing and attention is paid on the undrained shearing of the soil and decrease of pore pressures. Chapter 3 is constituted by the theoretical background of several analytical models that were found in literature and are used for calculating the forces required for mobilising a steel medium which is embedded in soil. In addition, an analytical analysis is conducted with these models and the models' performance is analysed. Chapter 4 includes details of the experiments conducted for this study. Information such as the test setup, techniques and programme is provided. The experimental results

are presented and analysed in Chapter 5 and correlations between the test variables and recorded results are discussed. Finally, Chapter 6 includes the conclusions drawn during this study and various recommendations are made for further research.

1.5 Problem aspects omitted in this study

The focus point of the current thesis is the analysis of the soil failure mechanisms that take place in dense and fine sands during rapid shearing. In the case of landfall operations SWRs are pulled through the soil and also get deformed. However, these deformation mechanisms and their effect to the pulling resistance are not taken into consideration as the steel element used in the current study was a steel pipe. Possible scenarios of the sand-SWR interaction are referred to in Chapter 6.

Chapter 2

Literature review

Granular soils' response to shearing is dominated by their relative density. Loose soils tend to contract and dense soils tend to dilate. As discussed in Chapter 1, problems were encountered in two past projects when the SWRs interacted with dense sands and therefore sand dilation is examined further. This chapter investigates the response of sand to shear loading. In other terms, the factors affecting the tendency of sand to dilate are analysed and connections are made to pore pressure changes.

2.1 The response of sand to shear loading

The tendency of sand to dilate can cause a significant increase of the resulting pulling forces of the SWRs. Radial stresses on the external surface of SWRs increase due to the fact that soil particles intrerlock with the steel interface. The phenomenon of dilation is influenced by multiple factors that are described in this section and specifically in Section 2.2. Information has been extracted by [17] and [18] and this provided a basis on which attention must be paid for the understanding of the mechanisms that develop during the landfall operations.

The parameter that expresses the soil's tendency to dilate, the dilation angle, decreases as the confining pressures inside a soil deposit increase. In addition, it has to be noted that in case the confining pressures are extremely high, the soil particles are crushed and shear strains take place within the shear. Hence, a dense sample is expected to densify even further or maintain its initial volume instead of dilate in case the confining stress levels are extremely high.

[17] suggested that a steel medium embedded in the soil can be treated as being significantly more rigid than a soil. This medium has a specific roughness which contributes to the total shear resistance of the interface. An observation to the total interface shear resistance can be made by examining the interface at a microscopic level. It could be said that, due to the steel elements' roughness, there are some protruding micro-facets with an inclination of "i" as illustrated in Figure 2.1. This inclination adds up to the micro-facets surface and soil interface friction angle (δ_s) and the final interface friction (ϕ_n) angle is formed. The latter is an equivalent of the peak interface friction angle, "δ_p" that is used later in the current study and their correlation is described in Equation 2.1. [18] stated that sliding on the inclined teeth causes work to be done against the applied vertical load, thereby making the shear resistance on the sand-steel interface greater than it would be on just from sliding friction on smoother surfaces.

$$\delta_p = \phi_n = \delta_s + i \tag{2.1}$$

However, this also implies that in case the steel medium is extremely rough then the shear band will be relocated away from the sand-steel interface and consequently the shear

Figure 2.1: Surface roughness of a steel medium [17]

resistance will be equal to the shear strength of the soil. [17] noted that the shear resistance of a sand-steel interface is dependent on the soil particles' interlocking which has to be overcome. The interlocking effects therefore are constituted by two components:

1. The shear resistance between the soil particles. For interlocking, the residual frictional resistance (ϕ_r) better represents the resistance that develops for small shear displacements, in comparison to the peak shear resistance (ϕ_p).

2. The dilation of the soil which is represented by the dilation angle (ψ). Work is produced while the soil particles tend to roll on top of each other.

2.2 Factors affecting the shear strength and dilation of a sand-steel interface

[18] conducted an extensive research on sand-steel interface peak strength, varying multiple parameters such as the steel surface roughness, particle size and density of the sand as well as the stress level at which the shear box tests were conducted. The effects of these parameters are further discussed in the following subsections.

The classic direct shear (DS) box test was modified by replacing its bottom part by various steel plates (all with different roughness), as illustrated in Figure 2.2.

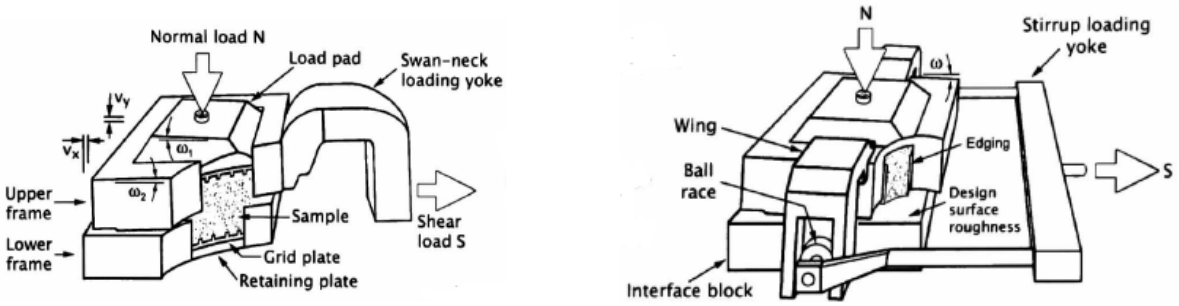

(a) Standard shear box apparatus

(b) Modified shear box apparatus

Figure 2.2: Direct shear box apparatus modifications by [18]

The weight of the upper frame and the soil situated in it were added to the normal stresses applied during the DS tests, in order to achieve more accurate results. The following parameters were defined for measuring the interface shear resistance:

- Peak interface friction angle, δ_p: corresponding to the peak friction angle of a soil as in regular DS tests, ϕ_p.

- Peak interface dilation angle, ξ_p: corresponding to the soil dilation angle of a soil as in regular DS tests, ψ_p.

2.2.1 Steel interface roughness

Figure 2.3 illustrates the layout of different sand particle sizes on surfaces with different roughness. It can be seen that the fine particles have significantly more interlocking effects than the coarse sand particles, which results in a larger interface friction.

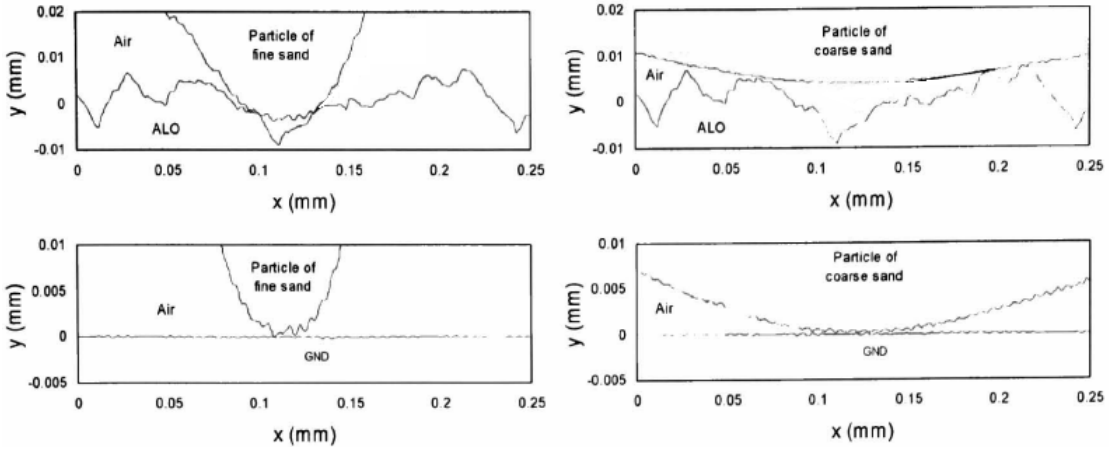

Figure 2.3: Fine sand (left) and coarse sand (right) particles, on rough (upper) and smooth (lower) surfaces [18]

Normalisation of surface roughness was introduced (relative roughness) and used for making clear that generally a fine sand can mobilise higher shear resistance than a coarse sand on a surface with the same roughness. This parameter is expressed in Equation 2.2 and it is constituted by the ratio of average surface roughness, R_{a}, over the average particle size, D_{50}.

$$R_{\mathrm{n}} = \frac{R_{\mathrm{a}}}{D_{50}} \tag{2.2}$$

2.2.2 Soil Particle size

Figure 2.4 illustrates the effect of relative roughness on the interface friction and dilation angles for sands with different particle sizes. This allows for a clearer view of the results for low (relative) roughness surfaces.

A linear increase is noticed in δ_{p} with increasing roughness. The intermediate roughness zones show approximately the same behaviour for coarse medium and fine sands when plotted with the normalised roughness parameter. After a normalised roughness of 0.02 a plateau is noticed at approximately 42° for the fine sand and 48° for the medium and coarse sands.

The dilation effect shows a similar behaviour in Figure 2.4b as it can initially be observed that no dilation occurred at surfaces with low relative roughness (< 0.003) for all sands. Moreover, the dilation of fine, medium and coarse sands is shown to be equal and increases linearly until a relative roughness of approximately 0.02 is reached. At relative roughness values greater than 0.02, it is observed that the coarser the material is the larger the dilation becomes. As reported by [18], at extremely high roughness levels the dilation reaches stages where the $\xi_{\mathrm{p}} = \psi_{\mathrm{p}}$. Based on the conclusions by [18] the latter occurs when the relative roughness values are equal or greater than 0.08.

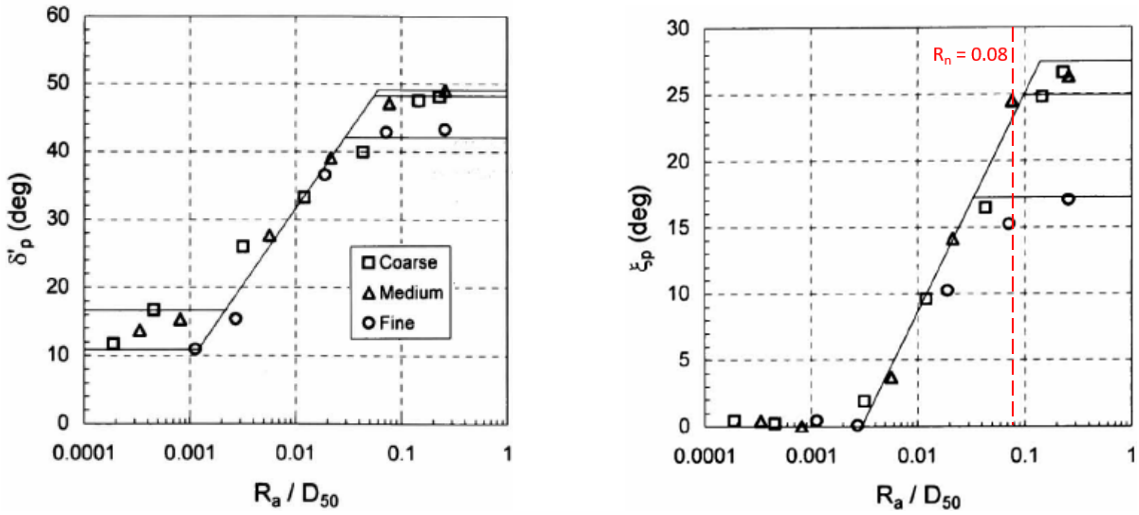

(a) Interface shear resistance

(b) Interface dilation

Figure 2.4: Effect of particle size on interface friction and dilation angles relative to normalised roughness, at a normal stress level of 25 kPa [18]

2.2.3 Soil relative density

The results of interface friction and dilation angles with respect to the average roughness for a sand at different relative density levels, are presented in Figure 2.5. It has to be noted that the legend of this figure indicate a decreasing roughness value from "Shear" to "GND". Details regarding the fabrication of the steel plates used during the modified DS tests are provided in Table A.1.

The first observation that can be made is that the higher the relative density is, the higher the interface friction and dilation angles that are obtained. However, it has to be noted that this is true only for the current case where a normal stress of 25 kPa was induced. This normal stress was chosen by [18] on purpose in order to allow for the maximum dilation effect to take place. For each of the relative densities there is a linear increase of δ_p and ξ_p with an increase in surface roughness. When the lines in Figures 2.5a and 2.5b reach a plateau then δ_p and ξ_p correspond to ϕ_p and ψ_p, respectively.

Figures 2.5c and 2.5d also illustrate that the change in δ_p and ξ_p is analogous to the relative density for surfaces with different roughness. An linear increase of δ_p and ξ_p is noted as the relative density is increased, for all surfaces tested. Additionally, it should be noted that the smoother a surface is, the lower the values that correspond to the interface shear resistance and dilation. No dilation occurs at very smooth steel surfaces (GND). In general, [18] noted that friction and dilation at the interface zone for intermediately rough surfaces is proportional to the relative density.

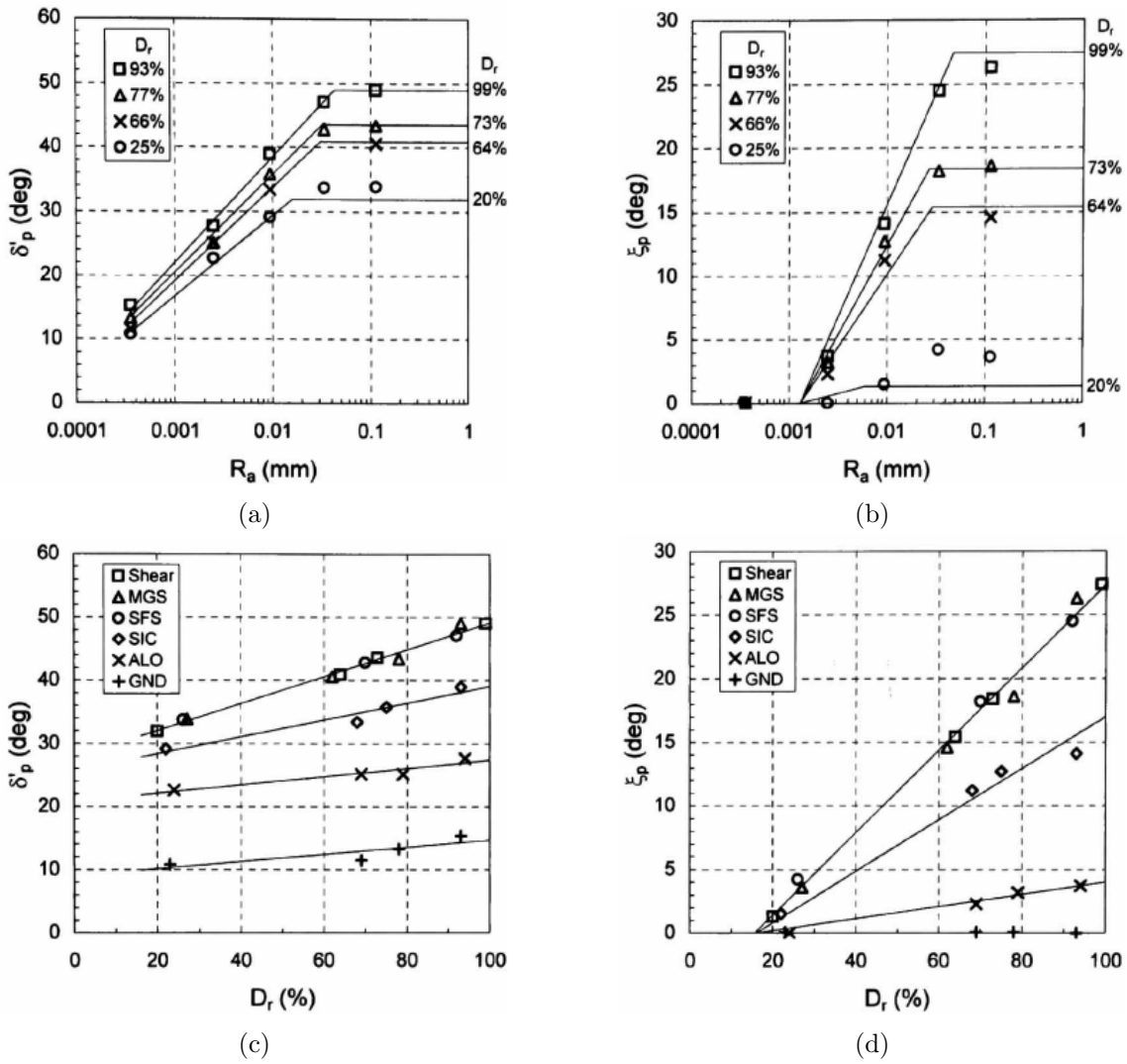

Figure 2.5: Effect of average roughness ((a) and (b)) and relative density ((c) and (d)) to the shear resistance and dilation angles, at a normal stress level of 25 kPa [18]

2.2.4 Stress levels

Based on the results of the experiments conducted with dense coarse sand, illustrated in Figure 2.6, it can be observed that both δ_p and ξ_p decrease with the increase of normal stresses except when the surface is smooth. [18] have attributed the latter response to the fact the soil particles are restricted from rolling on top of each other at higher stresses and therefore are dragged. As a result, dilation is restrained in high stress conditions.

The results of interface shear resistance tests for multiple steel surfaces that were conducted by [18] have indicated that there is a linear relationship between the angles of interface friction and dilation. This relationship is described by Equation 2.3 and it correlates the two angles with an error band of $\pm 3°$. The results can be divided in the "dilatant" and "non-dilatant" based on the interface response to shearing. [18] concluded that the dilation potential can be described as follows (also see Figure A.1):

1. At smooth surfaces the soil particles slide on the steel surface, hence dilation does not occur.

2. At intermediate and rough surfaces the soil particles roll on top of each other and this movement results in dilation.

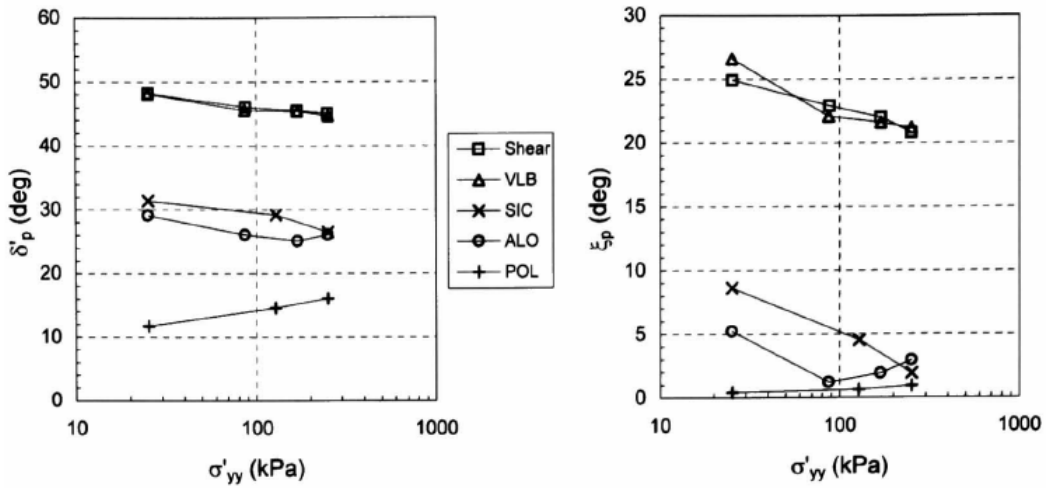

Figure 2.6: Effect of normal effective stress on interface friction *(left)* and dilation *(right)* angles for dense coarse sand [18]

$$\delta_{\mathrm{p}} = 25^{\circ} + \xi_{\mathrm{p}} \tag{2.3}$$

2.3 Reduction of pore pressures

Based on the experience of Allseas, excessive pulling forces are suspected to be generated due to the drop of pore pressures around on the sand-steel interface while the SWR is pulled. The development of excess pore pressures can be attributed to the tendency of the soil to dilate during undrained shearing. This section is dedicated to the research of this phenomenon with relevant findings from the literature that could justify the excessive pulling forces.

2.3.1 Triaxial tests

[20] showed via triaxial tests that "cavitation can occur spontaneously in a saturated sand during undrained loading." [20] conducted 3 undrained triaxial tests with medium-grained dense sand at a relative density of 86%. At each test the samples were loaded with different initial back pressures of 150, 350 and 550 kPa and corresponding cell pressures of 200, 400 and 600 kPa. As a result, the same net confining stress of 50 kPa was initially applied to all samples.

The volumetric strains of the samples were measured by recording the volume of water entering or exiting the triaxial cell. This method was initially tested with a drained sample and it was compared to the change of water volume entering or exiting the sample. The comparison of these two methods showed a good agreement.

It was stated that a dense sand tends to dilate when it is sheared and negative water pressures develop in its pores. In instances where drainage is fully controlled, such as in undrained triaxial tests, cavitation can take place. This decrease of pore pressures increases the shear strength of saturated sand as it increases the vertical effective stresses. Hence, the lower the pore water pressure drops, the higher the strength that is expected to be gained by the sand. This is because in undrained conditions stresses are induced on the water, in addition to the soil skeleton.

In addition, drainage was allowed once cavitation took place. Consequently, volumetric changes took place as the sand samples experienced dilation. As a result, this additional strength was lost when the water was drained. This phenomenon is also expected to be

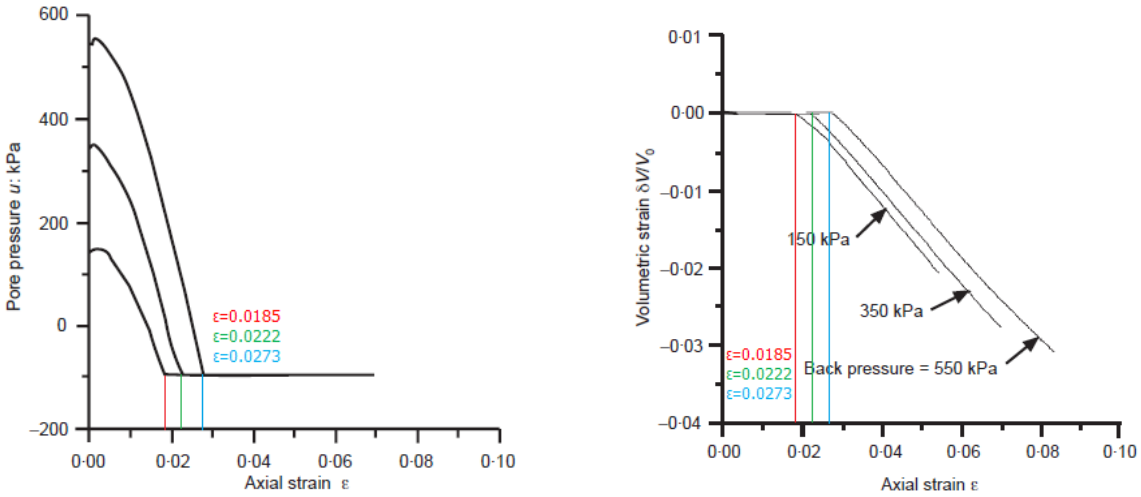

(a) Development of pore pressures

(b) Development of volumetric strains

Figure 2.7: Pore pressures and volumetric strains with respect to axial strains [20]

governed by the soil's permeability. Moreover, [16] stated that cavitation seems to be restrained, even by dense sands, when the effective stresses are at high levels and this was attributed to the fact that dilation cannot occur either.

Based on the results obtained by [20] the following comments can be made:

- The pore pressure level at each test starts from the induced back-pressure and it decreases to a point where cavitation occurs, at specific axial strains for each test. This decrease is due to tensile stresses experienced by the pore water during shearing. (Figure 2.7a)

- All three samples had approximately the same pore pressure reduction rate which was constant up to the point when cavitation occurred. This was attributed to the same dilation potential for all three samples as they were all assembled with the same relative density. After that point, only axial strains took place at the same, negative, pore pressure level for all 3 samples. (Figure 2.7a)

- No volumetric strains were observed before cavitation occurred as expected in undrained shearing of a saturated soil. Once cavitation was observed (at different axial strains for each sample as mentioned above) a decrease of volumetric strains (increase of sample volume) is observed with approximately the same rate for every sample and it was attributed to dilation. (Figure 2.7b)

In addition, two more detailed comments can be made on Figure A.2.

- The cavitation is also visible through the effective stress paths where a change of inclination is observed and tends to equalise with the stress path expected for drained loading condition. (Figure A.2b)

- Post-cavitation, part of the strains were recovered, however plastic deformations were also induced. During this unloading stage the pore water pressure remained constant at negative levels. (Figure A.2c)

2.3.2 Soil nail pull-out tests

The bond resistance of drilled and grouted nails was tested extensively by [21]. Physical modelling took place at large scale and soil nails were installed and pulled out from a medium plasticity clay. The soil mismatch with the geological conditions of the current thesis does not allow for developing trustworthy relations. However, it is believed that several outcomes from these experiments can provide a sound theoretical background of the mechanisms that develop on the grout-soil interface when the soil nail is mobilised.

One of the aims of these tests was to obtain the influence of altering the in-situ stresses in the soil to the pull-out capacity of the soil nails. The soil nails were pulled-out with different rates as the influence of the pulling rate to the pulling forces was another focus point. As it was reported by [21], controlling the pulling rate was initially extremely challenging. Figure 2.8 depicts an example of unexpected fluctuations that took place during a test. From the latter incident it was shown that sudden increases of shear stresses on the soils nail's external surface took place and were fully attributed to sudden unplanned increases of the pulling rate.

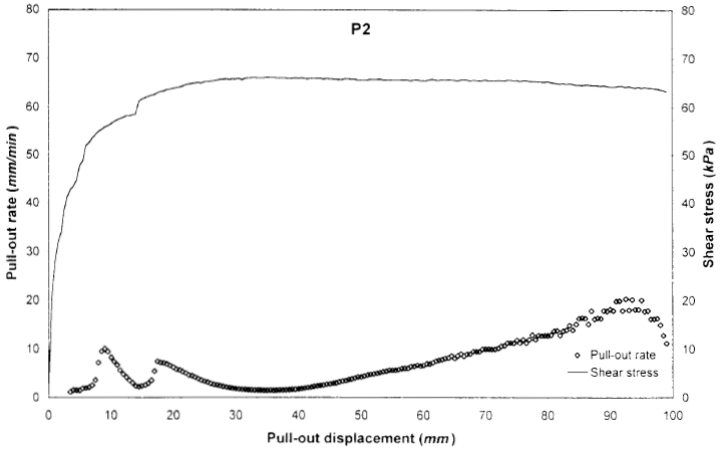

Figure 2.8: Pull-out of a soil nail with unplanned fluctuations of the pulling rate (source: [21])

In addition, an immediate decrease of the axial force at the nail head and consequently to the shear stress was noted at a different test. This is depicted in Figure 2.9 and [21] stated that this sudden decrease was "certainly due to a sudden drop in pulling rate" as the rate recording indicated a drop at the corresponding time. This behaviour was unexpected and therefore it was referred to as a focus point for further investigation.

[21] conducted only one experiment for which a constant load was applied on the specimen. The focus point of this test was to measure the changes of pore pressures on the grout-soil interface. This was achieved by installing a pore pressure transducer on the grout-soil interface and the results that were obtained are depicted in Figure 2.10.

It can be seen in Figure 2.10b that once the initial load was applied, suction (plotted as positive) was recorded and slowly dissipated as the pulling rate remained low. In addition, at a time of 15 hours two fluctuations of the pulling rate caused corresponding fluctuations of suction on the grout-soil interface. In addition, a small fluctuation on the load was noted, however the reason of this incident occurring was noted as unclear by [21].

The influence of pulling rate to the pulling capacity of the soil nails was also commented by [21] and special attention was paid to the mechanisms that take place during the pulling process. It was stated that the tests were conducted in partially undrained conditions and it was explained that dilation takes place as plastic strains accumulate around the grout-soil interface. As a result, dilation causes a reduction in the pore pressures. In addition, it

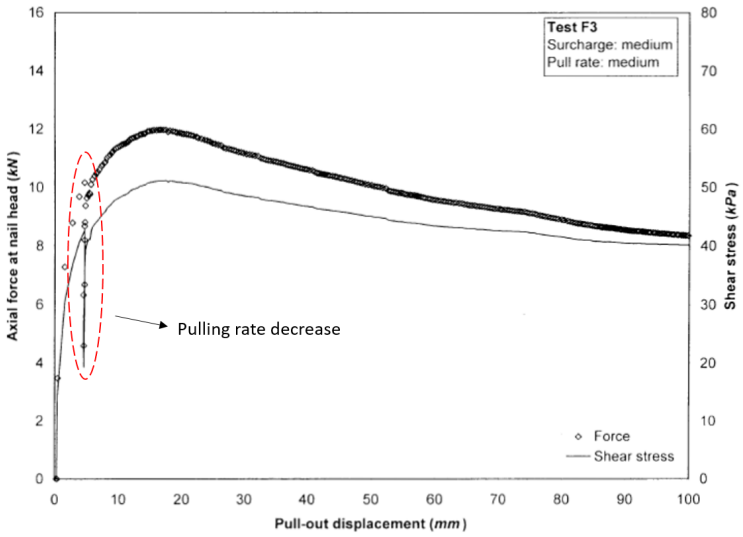

Figure 2.9: Pull-out of a soil nail with a unplanned decrease of pulling rate [21]

was mentioned that dilation causes a permanent increase of radial stresses on the soil nail, whereas the suction effect is only temporary and dissipates with a rate which a function of the soil's permeability.

However, it can be observed that in most cases the pulling rate was maintained at values greater than 1 mm/min, even at the force-controlled experiment. Therefore, it can be said that the loading conditions were undrained and as a consequence dilation was restrained. The decrease of pore pressures noted prior to the peak pulling can be attributed to the tensile stresses developed in the pore water due to the soil's tendency to dilate.

In addition, the following remarks were made based on all the experimental results. These support the relation of the decrease of pore pressures with the increase of the pull-out forces and it could be said that they could generally apply for any soil interface at which there is susceptibility for dilation.

1. For a given in-situ stress the soil nail resistance recorded towards the end of the test was similar, regardless the pulling rate
2. High initial values of soil nail resistance were measured at the highest pulling rates
3. Similarities were noted between the shear stress curves recorded during the medium and slow pull-out rate, in terms of shape

Finally, numerical analyses that were conducted by [21] with an in-house software at the University of Oxford indicated that "cavitation might occur during very fast pull-out testing."

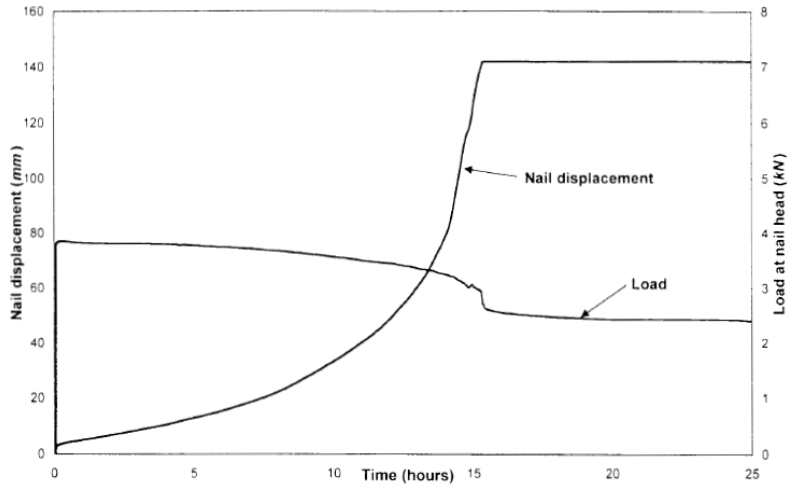

(a) Displacement - time - axial load curves

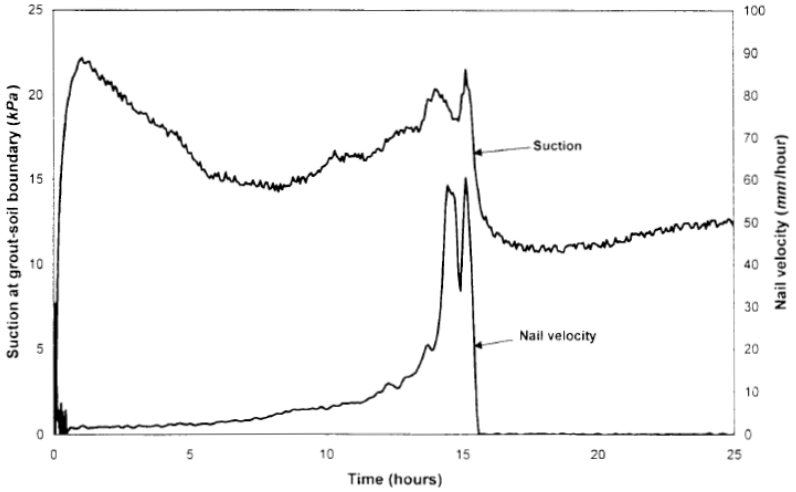

(b) Interface suction - time - pulling rate curves

Figure 2.10: Pore pressures and volumetric strains with respect to axial strains [21]

2.4 Expectations at landfall operations

Finally, an effort is made to estimate the situation expected during the conduction of landfall operations and the application of a pulling force on a SWR.

During a landfall operation the SWR is pulled through the seabed or the trench that has been constructed for the pipeline. During the installation of the SWR, the pulling process and the time in-between, sand settlement or natural backfill of the trench occurs and the SWR is therefore considered to be embedded in the sub-sea soil. Taking into account a high pulling rate (i.e. 7 cm/s) and the geological conditions, then the pulling process is considered to take place in (partially) undrained conditions. Consequently, it could be said that the pulling velocity plays a vital role to the force required to mobilise the SWR. This is because the pulling velocity is considered an equivalent of the rate at which shear loading takes place on the sand-steel interface.

Based on the information that was gathered through literature and the above-mentioned assumptions it is expected that the soil surrounding the SWR will tend to dilate during pulling. The magnitude of dilation depends on the roughness of the SWR, particle size and the stress levels. In case shearing takes place, a decrease of pore pressures is expected to occur, especially in sands of low permeability and the magnitude of pore pressure re-

duction is expected to be proportional to the pulling velocity. Another factor which is expected to affect the magnitude of pore pressure decrease is the sand's dilation potential. Hence, it can be stated that it is expected that the higher the pulling velocity, the greater the soil resistance is to be generated. The fact that the embedment depth of the SWR is relatively small translates to low confining stresses that favour the reduction of pore pressures.

Another effect that is expected to contribute to the excessive pulling forces is the concept of "loosening front" which was observed by [28] during his extensive experimental programme. This is illustrated in Figure 2.11 and only applies to SWRs. As it was stated by [28] when the rope is free to rotate at both ends, then during remobilisation it opens and hence it increases in length. Therefore, a small length increase occurs during the application of the pulling force, which then dissipates as the rope moves. The entire rope closes and hence rotates according to the direction of lay. During this process a high torsional resistance is exerted by the soil on the SWR. In the case when the rope is fixed from rotation on both ends, negative torque is generated. This dissipates slowly once the mobilisation of the SWR occurs and torque is observed to dissipate too.

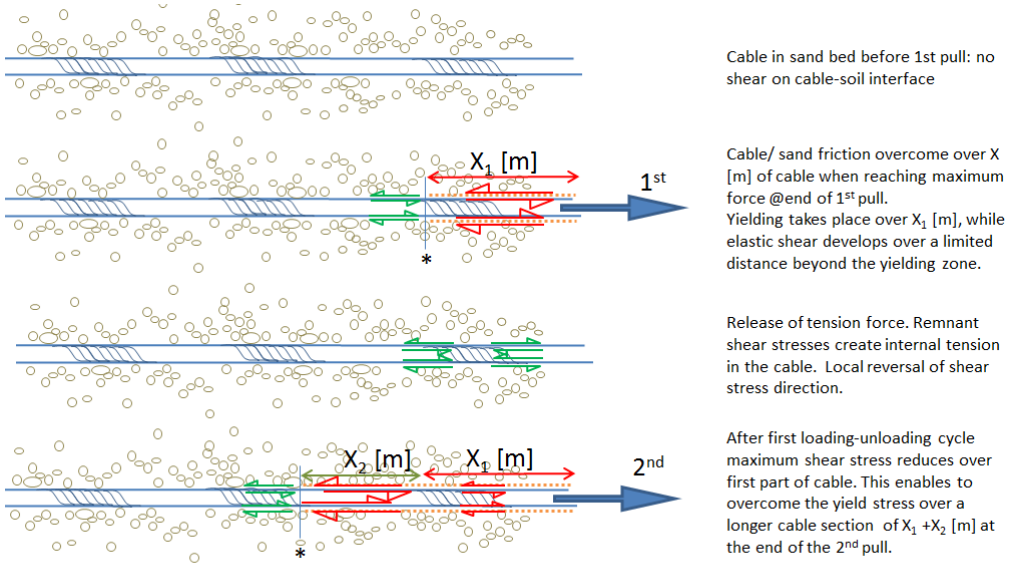

Figure 2.11: The loosening front effect [28]

2.5 Summary

Based on the literature research that was conducted it can be concluded that there is a theoretical relation between the tendency of granular soils to dilate and the decrease of pore pressures. Loading needs to take place in undrained conditions so that pore pressure reduction occurs at the sand-steel interface. The latter effect is expected to be proportional to the dilation (potential) of sand which was found to be analogous to factors such as the soil particle size, relative density, confining stress levels and interface roughness.

When shearing takes place in a granular soil then dilation is expected to take place. In the current case dilation is expected to be restrained due to the fact that shearing takes place rapidly in a saturated soil. Dilation is expected to be restrained by the incompressibility nature of pore water. In other terms, the volumetric changes are not expected to occur due to the tensile stresses that develop within the pore water. This effect is also

expected to be reinforced in a fine soil as water movement is further restrained. Consequently, the pulling velocity and soil permeability are considered to play a vital role to the magnitude of pore pressure decrease during this process. Finally, it is important to note that dilation is expected to take place eventually after the soil has exhibited its maximum shear strength and its critical state is reached.

Chapter 3

Analytical models

Three different analytical models were found in literature that may be suitable to predict the pulling forces required during pulling operations with SWRs through sand. These models differ significantly with respect to their complexity, approach, variables, accuracy and field of application. However, the common aspect between all these models is that all of them are developed for predicting the forces required to pull steel elements through sandy deposits.

The situation for which the pulling forces are estimated with these models is illustrated in Figure 3.1. A steel element (rod or SWR) is embedded in a sand deposit which is submerged in the water in order to simulate the seabed. The steel element is to be subjected to tensile loading which also is the principal parameter under examination.

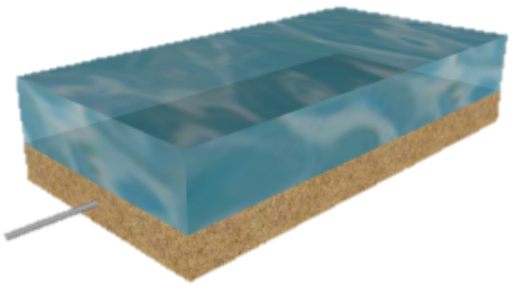

Figure 3.1: Buried steel element in saturated sand (schematic)

The three analytical models are described in this section. Detailed description and derivations of the models' formulae can be found in Appendix B. The parameters and processes that are considered by each model are discussed and comparisons between the models are made.

3.1 Klooster et al. (2015)

This model was developed for predicting the pulling forces of steel elements through a soil medium and it is based on the assumption that the pulling resistance is produced solely by shear forces. Hence, the components contributing to the resulting pulling force are as follows.

- Horizontal and vertical soil stresses
- Self-weight of steel element
- Steel element-soil interface friction

The change of soil stresses around the steel element's perimeter is taken into account in high detail as it is depicted in Figure 3.2. The mathematical expression that describes the pulling resistance of a steel element with a circular cross-section is given in Equation 3.1. As it can be observed, the more values of θ used during the analysis, the more accurate the model's result will be.

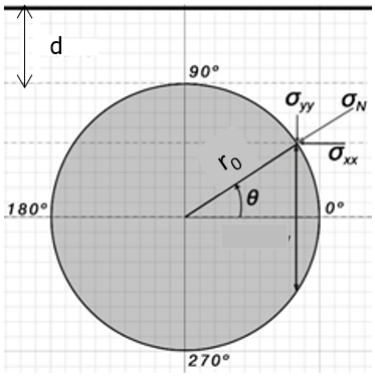

Figure 3.2: Soil stresses acting on a buried steel element [14]

$$T_{\max} = 2\mu \int_0^{90} \sigma_{\mathrm{N,top}}(\theta)\; r_0\; l_{\mathrm{e}}\; d\theta + 2\mu \int_{270}^{360} \sigma_{\mathrm{N,bottom}}(\theta)\; r_0\; l_{\mathrm{e}}\; d\theta \tag{3.1}$$

Where:

d = Burial depth [m]	σ_{xx} = Horizontal component of σ_{N} [Pa]
r_0 = Radius of steel element [m]	σ_{yy} = Vertical component of σ_N [Pa]
$\mu = \tan\delta_{\mathrm{p}}$ = friction coefficient [-]	l_{e} = Effective length of steel element [m]
σ_{N} = Effective stress normal to the steel element's surface [Pa]	θ = Angle to horizontal axis [°]

3.2 Luo et al. (2000)

A model to predict the pull-out capacity of soil nails installed in cohesion-less soils was developed by [17]. Even though this model was developed for this particular application, the authors have stated that it could also be used for "any longitudinal strip reinforcement in dilative soils". As a result, this model could, theoretically, be used for predicting the pulling forces of SWRs during landfall operations, in drained loading conditions.

This model is based on the fact that the soil exerts overburden pressure on the steel medium. In addition, the dilation of the shear band around the steel elements' surface is considered. The dilation of soil causes radial stresses to increase and consequently the pull-out resistance of the steel medium is increased. In other terms, it can be understood that when dilation occurs the effective stresses on the steel element's surface are increased. The resulting pulling force ($T_{\max}$) of the steel element is a function of it surface area, A_{n}, the maximum effective stress on the steel element, $q'_{\max}$, and the angle of internal friction of the soil. $q'_{\max}$ not only involves the soil stresses as a function of depth, but as a function of dilation too, as it is further explained in Appendix B.2. The function that describes the maximum pulling forces is given in Equation 3.2.

$$T_{\max} = A_{\mathrm{n}}\; q'_{\max}\; \tan\phi_{\mathrm{p}} \tag{3.2}$$

3.3 Luger (2014)

This model was developed by Deltares on request by Allseas within an investigation that was completed in 2014 regarding the prediction of the pulling forces during landfall operations. The model was based on the experience that was gained by Allseas at Noble Tamar and Shell Corib projects. In addition, professional experience by the scientists of Deltares highly contributed to the development of this model. As a result, the model focuses on the drained behaviour of the soil and on the response and layout of the SWR during the pulling procedure.

As it is described in Equation 3.3 the maximum force for mobilising a SWR or, in general, a steel element which is embedded in a soil is a function of the steel element's self weight (F_{w}), burial depth (F_{Δ}), sand-steel interface dilation (F_{Ψ}), steel element's curvature (F_{c}) and effective length (l_{e}).

$$T_{\max} = (F_{\mathrm{w}} + F_{\Delta} + F_{\Psi} + F_{\mathrm{c}})\, l_{\mathrm{e}} \tag{3.3}$$

[19] identified several phenomena that are expected to occur during the pulling of SWRs at landfall operations which could result into excessive forces. However, these were not quantified nor added to the current analytical model. These aspects include the following.

- Rope surface anisotropy effect: Resistance of torsion developed by the soil acts on the SWR during pulling which is then expected to increase the pulling forces.
- Additional resistance due to rope anomalies: Kinking and bird-caging (see Figure B.2) can occur due to torque. In these instances the SWR deforms and its cross sectional area increases locally, where deformation takes place. Consequently, the bigger the cross sectional area becomes, the higher the required tensile forces that are required to mobilise the SWR.

3.4 Validation of the models

The performance of the theoretical models was investigated by comparing the predictions of the three models with the results of small scale experiments. [14] conducted small scale experiments that involved the pulling of a steel rod and a SWR with nominal diameters of 6 mm. The testing programme included a variation of the burial depth ($0 - 15$ cm) while the pulling velocity was kept constant at 2 cm/s. The input used for these simulations can be found in the following sections. Conclusions were therefore derived regarding the applicability of the three analytical models described above and their accuracy on predicting the pulling forces.

3.4.1 Input

Shear modulus

The models by Luo et al. (2000) and Luger (2014) include the effect of the shear modulus of the soil as a basic parameter that influences the total resistance. [19] proposed that the shear modulus changes with the effective stress levels, hence with the different burial depths. A method of calculating the shear modulus at different burial depths was suggested and can be obtained with Equations 3.4, 3.5 and 3.6. Figure 3.3 illustrates the development of shear modulus at different depths, obtained with the suggested method.

The value of Young's modulus of the sand used in the experiments is approximately 20 MPa, as it was mentioned by [14]. Assuming that the material that was used is

homogeneous and isotropic, a value of 0.3 for the Poisson's ratio, (ν). Based on Hooke's law, Equation 3.4 can be used for determining the shear modulus:

$$G = \frac{E}{2(1+\nu)} \tag{3.4}$$

If it is assumed that the Hardening-Soil (HS) model rule can be applied – as suggested by [19] – then Young's modulus can be calculated as follows:

$$E = E_{\text{ref}} \left(\frac{\sigma'_3}{p_{\text{ref}}} \right)^m \tag{3.5}$$

With:

$$\sigma'_3 = d\,\gamma'\,K_0 \tag{3.6}$$

Where:

E = Young's modulus [Pa]
σ'_3 = Minor principal stress [Pa]
d = Burial depth [m]
K_0 = Earth pressure at rest [-]
m = Power in stress-dependent stiffness relation = 0.5 (for sands) [-]
E_{ref} = Reference Young's modulus [Pa]
p_{ref} = Reference pressure = 100 [kPa]
γ' = Effective unit weight of the soil [kN/m^3]
G = Shear modulus [Pa]

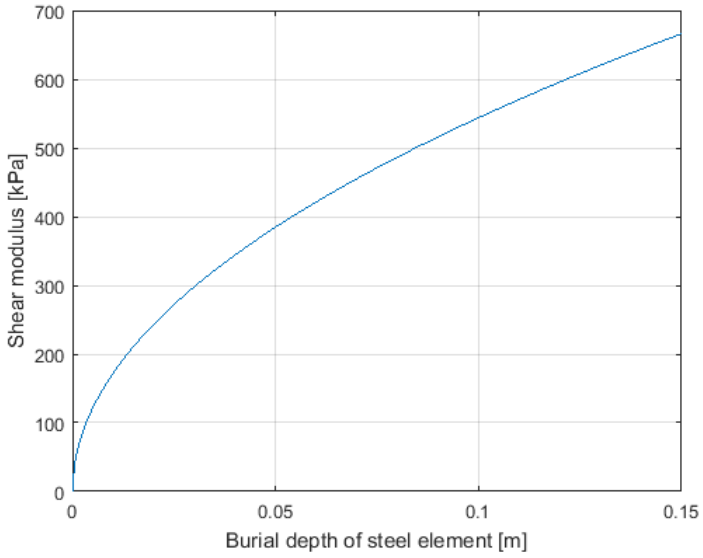

Figure 3.3: Change of shear modulus with respect to burial depth

Interface friction characteristics

An effort to differentiate between the rod and the cable tests was made and it was based on the input data that was used by [14] at their analyses. When the friction coefficient ($\mu = \tan\delta_{\text{p}}$) was calculated for the rod tests a value of 22° was used for the interface friction angle, indicating that there was a steel-sand interface at the shearing zone. However, when simulating the cable tests $\mu = \tan\phi_{\text{p}}$ was used, indicating that a soil-soil interface occurs at the shearing zone. The latter was attributed to the fact that sand particles stick between the SWR strands due to the high roughness of its external surface.

A similar approach was followed when using Luger's (2014) model. However, this model allows for quantifying the contribution of the sand and the steel element to the interface shearing resistance with the so-called terms P_{sand} and P_{mat}, respectively. Values of $P_{\text{sand}} = 0$ and $P_{\text{mat}} = 1$ were used for simulating the rod tests and vice versa for simulating the cable tests.

[19] has also suggested that the shear zone thickness (t) should be approximately 5 times the average grain size of the soil, so in this occasion a value of 500 μm was chosen to be used as $D_{50} = 103$ μm. The change of thickness of the shear zone (Δt) is proposed to occur at a shear strain of the order of 2.5%, hence resulting at a value of $\Delta t = 0.025 \times 500$ μm $= 0.0125$ mm.

The same principle was followed when using the model by Luo et al. (2000) producing two sets of results, one for each steel element (rod and cable) that was used in the experiments. In addition, this model also takes into account the critical shear displacement (u_{c}) of the steel element which translates to the shear displacement which corresponds to shear failure. Values of 0.5 mm and 1 mm were used for steel elements with low (rod) and high (SWR) roughness values, respectively. It has to be noted that [17] have not made any recommendations regarding the exact value for different steel surface roughness, however a value of $u_{\text{c}} = 1$ mm was proposed to be used at one of their applications. The input introduced above can be found in Table 3.1.

Table 3.1: Values used as input for predicting the experimental results by [14]

	Klooster et al. (2015)		**Luo et al. (2000)**		**Luger (2014)**	
Parameter	Rod	Cable	Rod	Cable	Rod	Cable
ϕ_{p} [°]	42	42	22	42	42	42
δ_{p} [°]	22	22	-	-	22	22
u_{c} [mm]	-	-	0.5	1	-	-
P_{sand} [-]	-	-	-	-	0	1
P_{mat} [-]	-	-	-	-	1	0
t [mm]	-	-	-	-	0.500	0.500
Δt [mm]	-	-	-	-	0.0125	0.0125

3.4.2 Results

The results produced with the above-mentioned input are presented in Figure 3.4 and Figure 3.5 for the rod and the SWR, respectively. The experimental results indicated a linear increase of pulling force of the rod with respect to the burial depth. The pulling force required to mobilise the SWR increased exponentially with the increase of burial and higher magnitudes with respect to the rod results were noted.

Rod

The pulling forces of the rod tests seem to be estimated poorly by the models of Klooster et al. (2015) and Luger (2014). Both models show the development of the pulling force having very similar trend. However, the model by Luger (2014) indicated double magnitude of pulling forces initially. An intersection of the two lines occurred at a burial depth of approximately 0.13 m. The latter was followed by an indication of higher pulling forces by Klooster's et al. (2015) model.

The model by Luo et al. (2000) followed a totally different trend with respect to the trend of the experimental results. It could be said that this trend is mainly dependent on the development of the shear modulus with respect to the burial depth. Initially,

the pulling forces are overestimated (almost 5 times larger), but the difference from the experimental results decreased up to a point when an burial depth of approximately 0.13 m was reached where the two sets of data seem to come into an intersection. At burial depths larger than 0.13 m the pulling forces are underestimated by the model.

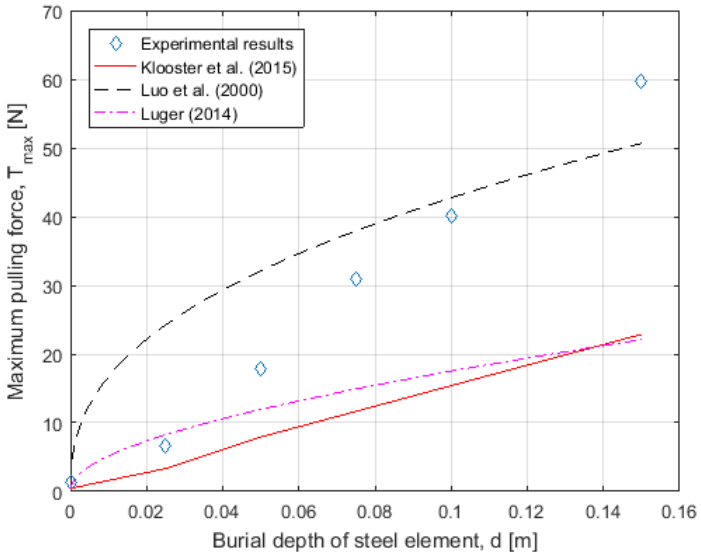

Figure 3.4: Prediction of pulling forces for rod, $D = 6$ mm

SWR

The experimental results of the SWR, depicted in Figure 3.5. From this figure it can be observed that Luger's (2014) model produced higher forces in comparison to the model by Klooster et al. (2015), initially. However, the difference of the forces produced by the two models decreased as the burial depth increased. Up to an burial depth of 0.025 m a good agreement is observed between the predictions of the two models and the experimental results, however beyond this point the difference increases as the experimental results show a steeper exponential increase in pulling force.

Similar to the prediction of the steel rod pulling forces, the model by Luo et al. (2000) model showed a totally different trend of the SWR pulling forces with respect to the burial depth compared to the experimental results, as illustrated in Figure 3.5. Similar to the rod, it can be understood that the trend of the this model is controlled by the development of the shear modulus. The magnitude of this prediction seemed to be influenced by the value of u_c too. The difference of the predicted pulling force magnitude for a rod and a cable with this model, as shown in Figure 3.4 and Figure 3.5, is attributed to the two different u_c and μ values.

3.4.3 Discussion

The deviation of analytical results from the experimental can be attributed to multiple aspects that are not included in the models or to the fact that there is room for improvement on the input parameters and assumptions taken into account.

Regarding the model by Klooster et al. (2015), it was shown that its predictions deviate from the experimental results for both the cases of the rod and the SWR. It was proposed by the authors that negative pore pressures are suspected to develop during pulling, which might explain the underestimation of the pulling force. The development

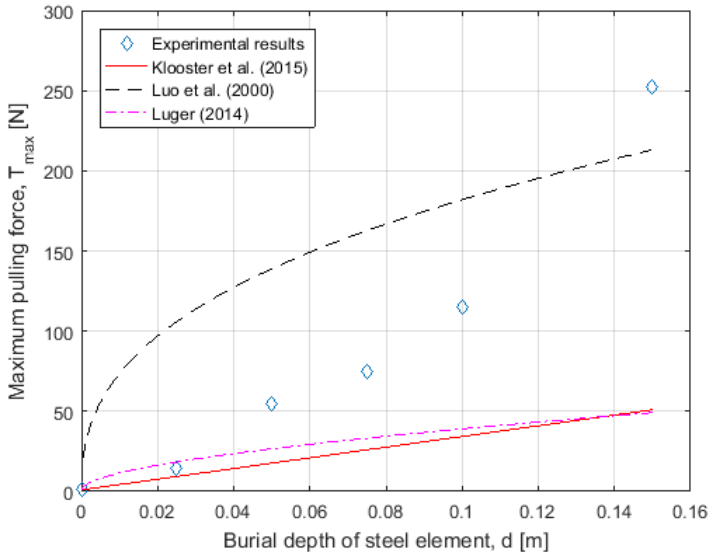

Figure 3.5: Prediction of pulling forces for SWR, $D = 6$ mm

of negative pore pressures, or at least the reduction of pore pressures, was described in Chapter 2 and it was attributed to the soil's tendency to dilate.

Therefore, soil parameters and load conditions such as pore pressure reduction, dilation potential, pulling velocity and soil permeability are directly connected to the magnitude of the pulling force. As a result, they should be taken into account by an analytical model in case a more accurate prediction of pulling forces is to be achieved.

Furthermore, as mentioned previously, the shear modulus of the soil significantly influences the magnitude and trend of the predicted pulling forces obtained with the models of Luger (2014) and Luo et al. (2000). Most significantly, for the latter it can be easily observed that the developed trend has a similar shape as the development of shear modulus in Figure 3.3. The method that was proposed by [19] for quantifying the shear modulus at different burial depths could be invalid for this application. Possibly, a different soil behaviour model different than the HS model better matches the application discussed in this thesis. A more detailed explanation is provided in Appendix B.4.2. Also, the critical shear displacement proved to be a dominant parameter for the model by Luo et al. (2000), however due to lack of information regarding this value, it cannot be altered accurately.

3.5 Summary

As it was mentioned in Chapter 1 the loading conditions at a landfall operation are expected to be undrained due to the high pulling velocity used as common practice. In contrast, the three analytical models account for drained conditions and therefore for volume changes on the shear band around the steel element. As a result, it is concluded that the models' formulation is not completely correct with respect to the soil mechanics that develop during the pulling of the steel element. However, it was decided to conduct more analyses and check their performance with respect to the current study.

The three analytical models have various similarities in terms of formulation, such as the overburden pressures acting on the steel element and the sand-steel interface behaviour. However, key differences can be observed regarding the processes and parameters that are considered in Tables 3.2 and 3.3.

It can generally be concluded that model by Klooster et al. (2015) is the most simplistic in comparison to the rest. The models by Luo et al. (2000) and Luger (2014) have

numerous aspects in common, with the latter being be considered as the most detailed model. This is because it takes into account more parameters than the rest. On the other hand, Luger's (2014) model takes into account more processes and this makes it equally complex with the latter. An extensive comparative study with the use of all the models was conducted to examine their applicability to the pulling operation and performance.

Table 3.2: Summary of processes included in the analytical models

Process	**Klooster et al. (2015)**	**Luo et al. (2000)**	**Luger (2014)**
Quantification of material contribution to resistance	-	-	✓
Increase of radial stresses due to dilation	-	✓	-
Increase of soil's frictional strength due to dilation	-	✓	✓
SWR curvature effect	-	-	✓

Table 3.3: Summary of parameters included in the analytical models

Parameter	**Klooster et al. (2015)**	**Luo et al. (2000)**	**Luger (2014)**
Relative density	-	✓	-
Burial depth	✓	✓	✓
Poisson's ratio	-	✓	-
Angle of internal friction	✓	✓	✓
Interface friction angle	✓	✓	✓
Shear modulus	-	✓	✓

The predicted pulling forces for the SWRs did not show an agreement with neither the trend nor the magnitude of the forces recorded at the experiments. The analytical models by Klooster et al. (2015) and Luger (2014) showed significantly lower pulling forces. The model by Luo et al. (2000) predicted pulling forces with higher magnitude in comparison to the prediction of the two other models. In addition, all models showed a different trend than the trend observed in the the experimental results. As a result, it was proposed that improvements can be made regarding the input that these models take into account.

It was shown that the parameters that dominate the magnitude of the final pulling force and the trend that is developed with respect to the burial depth of the steel medium, involve the shear modulus of the soil, the critical shear displacement and the contribution of the steel/soil to the interface shear strength. Additionally, none of the analytical models take into account the effects of pore pressure reduction due to dilation potential of a soil. This could be one improvement to be made, aiming for a more accurate prediction of the pulling forces required for mobilising the steel element.

Chapter 4

Physical modelling - apparatus materials and methods

This chapter summarises information relevant to the selection of the materials and apparatus used for the current study. The testing box is described and details regarding its structure are given. Moreover, the soil used in the experiments is characterised and its shear strength is determined. Finally, a description of the methods used for preparing the physical models and the testing programme are provided. Further information regarding the physical modelling can be found in Appendix C.

4.1 Apparatus

4.1.1 Testing box

Physical modelling took place at medium scale and involved the pulling of a steel pipe through wet sand which was deposited in the testing box depicted in Figure 4.1. The size of this tank is 2.50 × 0.43 × 0.40 m^3 (L × B × H) and it was constructed with S355 steel and acrylic walls on its longitudinal sides.

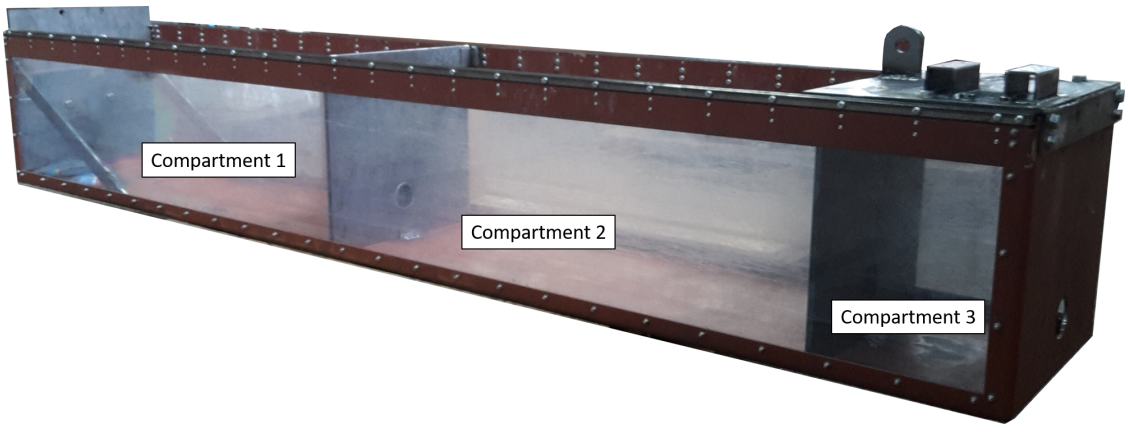

Figure 4.1: Testing box layout

The internal part of the box was separated in three compartments with the addition of 2 separating plates. This allowed for creating a more confined environment where the soil and the steel pipe could be placed. As a result, the length of the steel pipe that was interacting with the soil was constant and equal to 1 m. The pulling of the pipe was achieved with an electric motor which was fixed on a baseplate and was installed on the top of the small compartment. A braided Dyneema® rope was attached on the end of

the pipe and was guided through two pulleys. This rope type was chosen as it is highly undeformable and exhibits strains of approximately 3% at maximum loading conditions [24] as well as it is torque-free when subjected under tension. In this way measurement errors due to deformations of the pulling apparatus were minimised.

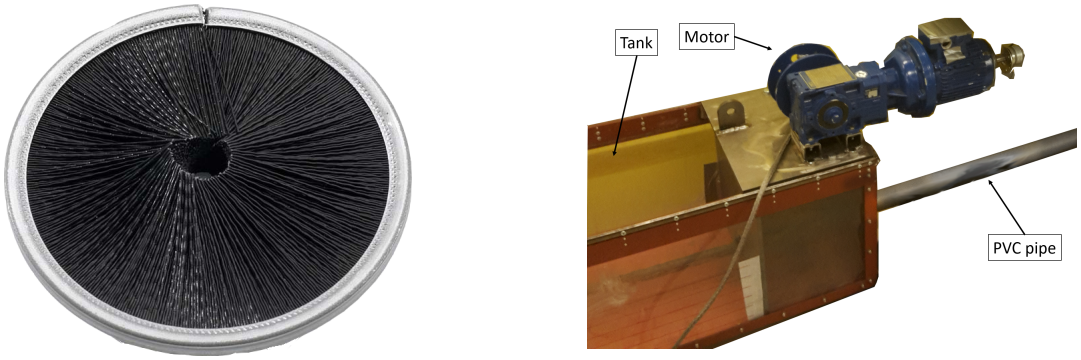

(a) Disk brush seal

(b) PVC (extension) pipe

Figure 4.2: Steel pipe support features on testing tank

Figure 4.2a illustrated the disk brush seals which were placed on the circular openings of the separating plates. These components allowed for the minimisation of sand transfer to the adjacent compartments during the pulling process. In addition, a free water flow between the box's compartments was achieved and the disks' synthetic fibres assisted to maintain low friction with the steel pipe.

Finally, as it is shown in Figure 4.2b, a PVC pipe was attached to the box's right hand side which allowed for a space extension where the steel pipe could be hosted, without extending the whole tank. The steel pipe was laying into the PVC pipe during the construction of the two sand foundation layers (F1 and F2). The steel pipe was placed carefully into the medium compartment when the latter two were completed and the placement of the remaining soil layers was continued. A portion of the steel pipe (>0.50 m) was also hosted by the PVC extension while it was positioned in the medium compartment, before the initiation of each experiment.

4.1.2 Steel pipe and installation of pressure transducers

A steel pipe with a length of 2 meters was used for the current experimental study. Medium scale conditions were achieved with a nominal diameter of $D = 30$ mm, considering the fact that SWRs with nominal diameters of 60-80 mm are used by Allseas at landfall operations. The external surface of the pipe was blasted with aluminium silicate blast cleaning grit, provided by [12], and an average roughness of $R_a = 11$ μm was achieved. The latter was applied for achieving a rough steel interface that would mobilise the full shear strength of the soil surrounding the pipe, simulating the rough external surface of a SWR.

Modifications took place on the steel pipe for hosting 6 pore pressure transducers (PPT) for which further information is provided in Section 4.1.4. These PPTs were used for measuring the changes of pore pressures on the sand-steel interface while the steel pipe was pulled through the sand deposit. A top-side-side pattern was followed when installing the PPTs which allowed for recording any possible pressure differences around the pipe's circumference.

Mounting the PPTs on the pipe required a process described in Figure 4.3 and the installation method was inspired by [22]. Initially, the pipe was cut and separated in sections (1), (2) and (3) with the corresponding lengths depicted in Figure 4.3a. This was done for achieving a convenient installation procedure for the PPTs. The PPTs were

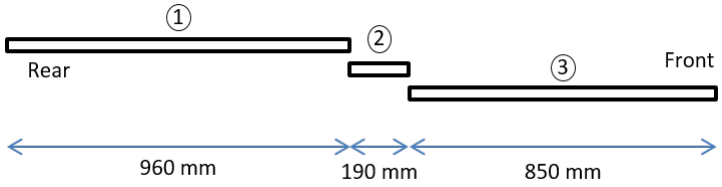

(a) Section cuts

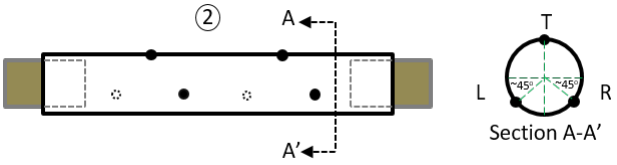

(b) Installation of top (T), left (L) and right (R) PPTs and overlapping connection pipes

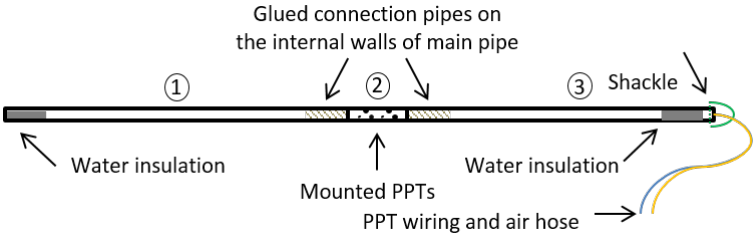

(c) Finishes

Figure 4.3: Internal structure of steel pipe

attached in section (2) on holes drilled with the pattern depicted in Figure 4.3b. These holes allowed for the direct contact of the PPTs with the water on the sand-steel interface. Two connection pipes with length of 60 mm each were also glued and pinned on the internal walls of the main pipe. These were used as overlapping components for connecting all the sections together and achieving a strong bond.

As it is shown in Figure 4.3c, insulation material was placed on each of the pipe's ends for providing a dry environment for the correct function of the PPTs, allowing the PPTs' wiring and an air hose to exit from the front end of the pipe. Finally, two holes were drilled on the front end of the pipe and allowed for the installation of a shackle which was used for attaching the pulling rope.

4.1.3 Electric motor and pulling line

An electric winch, commercially available by EMCÉ WINCHES®, was used as the pulling equipment for the experiments of the current study. The motor is depicted in Figure 4.4 and it was installed on the testing box as it was described in Section 4.1.1. The pulling capacity of the motor was tested prior to deciding on its use and it was found that a maximum pulling force of approximately 3 kN could be produced. In addition, the pulling velocity could be varied from 0 to 15.8 cm/s, which oversubscribed the prototype pulling velocity of 7 cm/s.

As it is indicated in Figure 4.5a, the pulling rope attached on the motor was connected on a straight line to the load cell with the use of a shackle. Another rope was attached on the opposite side of the load cell which was guided through the pulleys to the steel pipe.

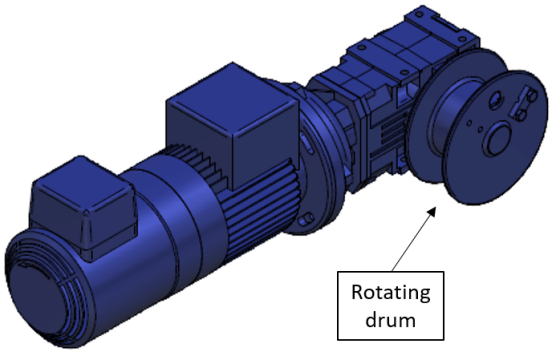

Figure 4.4: Schematic drawing of electric motor (source: EMCÉ Winches®)

Additionally, a steel eye (see Figure C.9) was welded on the winch plate in order to allow the creation of a pulling loop which is indicated in Figure 4.5b. This was created in case the motor was incapable of producing enough pulling force to mobilise the steel element. This design was inspired by the principle of "mechanical advantage", commonly used in pulley systems. This loop could be established by doubling the length of the pulling rope which was to be guided through a snatch block.

As a result, the pulling force, experienced at the position of the snatch block, could be doubled while the pulling velocity was reduced to half of the spooling velocity. The snatch block could be attached on the load cell with the use of a shackle. On the other end of the load cell the pulling line continues in the same way as it was indicated for the previous layout. Finally, it has to be noted that the position of the load cell was ideal in case the alternative pulling line was to be used. Also, it allowed for a displacement of more than 1 m which was approximately the displacement required to occur so that the PPTs could travel within the second compartment of the testing tank.

4.1.4 Electronic system

An Allseas in-house electronic system was used for the needs of the current thesis. This system is schematically depicted in Figure 4.6 and is constituted of the following two components, based on the function requirements of the experimental set-up:

1. Data acquisition from the connected sensors
2. Motor speed control

A description of the sensors used for these experiments follows below. In addition, the functions of the Data Acquisition System (DAS) as well as of the Motor Control System (MCS) are provided.

Sensors

As it was indicated in section 4.1.2, 6 differential PPTs were installed on the pipe on a top-side-side fashion. Initially, the intention was to install the PPTs on a top-side-bottom pattern, however this was not successful due to space restrictions within the pipe. All PPTs had the same dimensions as indicated in Figure 4.7 and were separated in two groups with respect to their sensitivity. Two different sensitivities were used for the PPTs as the expected change of pore pressures could not be predicted accurately.

As a result, the PPT groups had the capability of measuring pressure ranges of ±3.45 kPa and ±103.42 kPa. Every PPT was installed with the same manner in the pipe with one port facing the hollow section of the steel pipe and the other port facing the

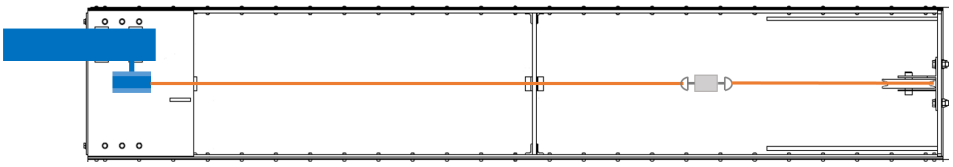

(a) Direct

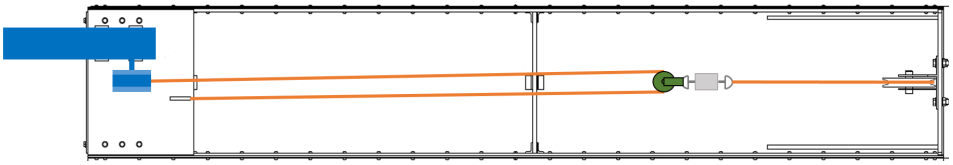

(b) With mechanical advantage

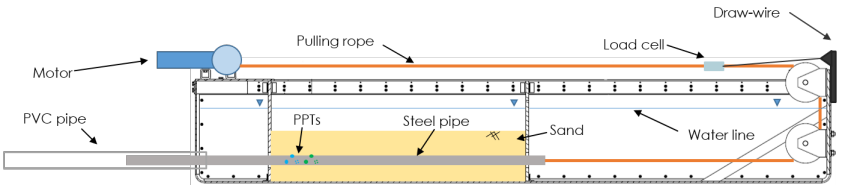

(c) Cross section of pulling line

Figure 4.5: Possible pulling lines with the current experimental set-up (top view)

sand-steel interface. A fine steel wire mesh was placed on the outer end to avoid the PPTs' port blockage by sand particles. Finally, the air in the outer port of the PPTs was replaced by silicon oil, providing accurate measurements pore pressure changes. Technical specifications of the pressure sensors are provided in Appendix C.3.

A two-way load cell by VPG Transducers®, with a maximum capacity of ±500 kg, was used for measuring the tension force required for mobilising the buried steel pipe. Finally, a draw-wire was used for measuring the displacement of the pipe during the tests.

Data acquisition system

The basic function of the DAS was to log all the signals produced by the test sensors (i.e. load cell, draw-wire and PPTs) and also to display the recordings on a computer's screen providing a live view of the pulling force, displacement and pressure changes on the sand-steel interface. As it is indicated in Figure 4.6, the logging took place by connecting the sensors with electric wires to wireless transmitters (nodes).

Two transmitters were used in total for hosting all the sensors and data was transferred wirelessly to a receiver node which was connected to the computer. In addition, the transmitters also functioned as electricity sources for the all sensors except for the draw-wire, which required an external power supply.

The majority of tests were conducted with a sampling rate of 4 Hz (0.5-4 readings/cm), however several experiments took place with a rate of 64 Hz (9-64 readings/cm) for increasing the recordings' accuracy. The sampling was always accompanied by an automatic logging of time.

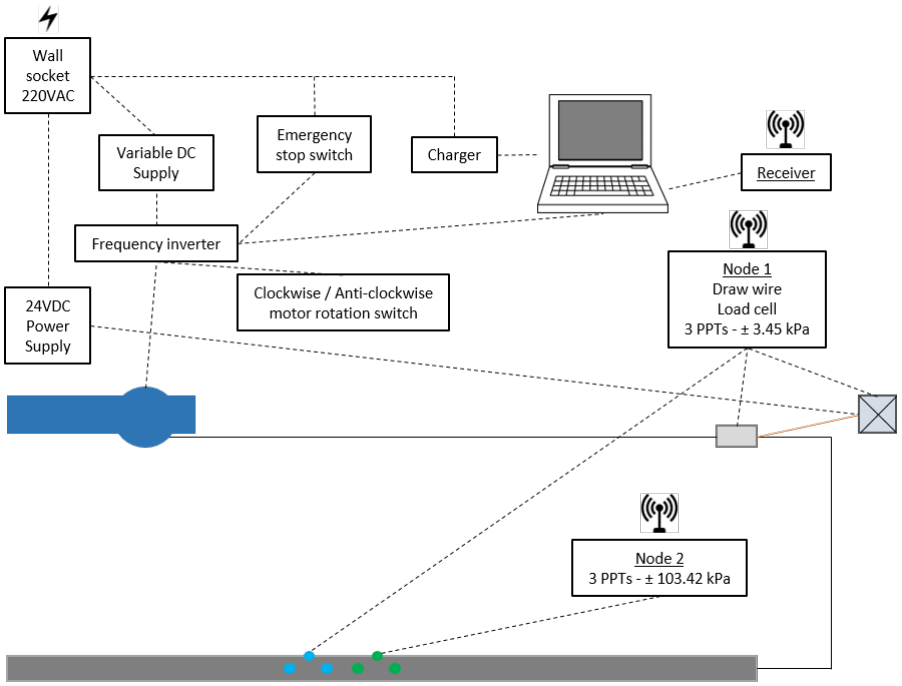

Figure 4.6: Simplified interpretation of electronic system (dashed lines indicate electrical wiring)

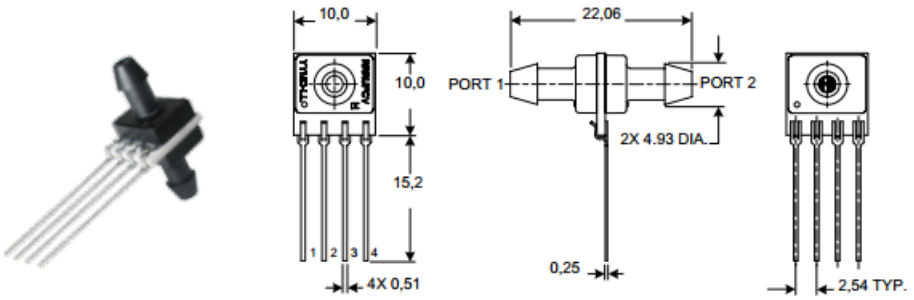

Figure 4.7: Differential pore pressure transducer - dimensions in mm (source: Honeywell®)

Motor control system

Ensuring the correct and safe use of the motor required the design of a control system. The main function of the MCS was to provide constant pulling velocities during the pulling procedure. Pulling velocities of 1, 4 and 7 cm/s were required to be achieved and to remain constant regardless the resistance experienced by the steel element which was pulled through the sand mass. The latter was achieved by fine-tuning a variable power supply, which altered the frequency of the converter connected to the motor. Two additional switches were added to the system that could be used for changing the motor's rotational direction and for stopping the motor in cases of emergency (i.e. short circuits and unexpected motor response), respectively.

4.2 Sand properties

The soil that was used for the current study was a natural, uniform, fine, silica sand. Characterisation tests were conducted and involved the determination of particle size distribution, density and shear strength by DS (small box apparatus). The results obtained by the soil characterisation tests can be found in Table 4.1.

4.2.1 Particle size distribution

Sieving took place following the guidelines defined by [7]. Sieve sizes of 600, 425, 300, 210, 150 and 63 μm were assembled and installed on a vibrating table as shown in Figure C.14. A total mass of 300 g of oven dried sand was used for the test and it was agitated for 30 minutes. The particle size distribution curve obtained from the test is depicted in Figure 4.8 below. Based on the results derived from this test and the guidelines of the Unified Soil Classification System [29] the soil was classified as "Poorly graded sand (SP)". It also has to be noted that fine material (particle diameter < 63 μm) was found to be less than 1%.

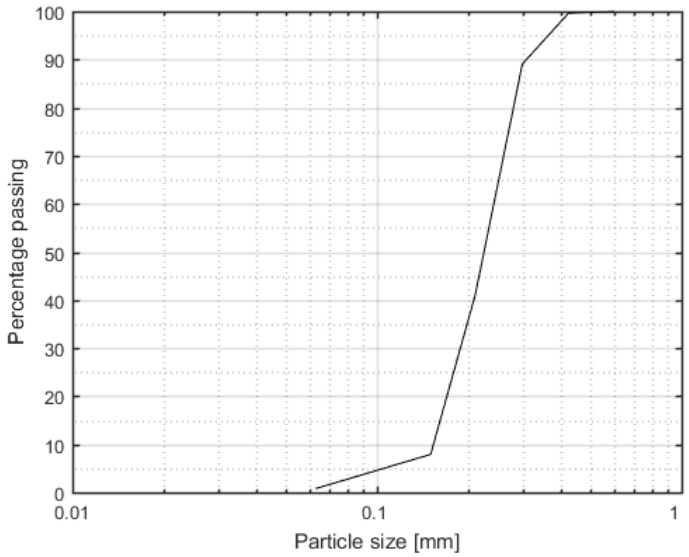

Figure 4.8: Particle size distribution curve

4.2.2 Density

The maximum and minimum density tests were conducted based on the guidelines provided by [2] and the apparatus used for this test is depicted in Figure C.15. Each test was repeated three times in order to improve the results' accuracy and it was found that the maximum and minimum void ratios are equal to 0.90 and 0.62 respectively. The also corresponded to maximum and minimum relative densities of 1635.7 kg/m^3 and 1379.3 kg/m^3.

4.2.3 Shear strength determined by direct shear (small box apparatus)

DS box tests were conducted with the use of a box with dimensions of $60 \times 60 \times 40$ mm^3 and with respect to the guidelines provided by [8]. A relative density of 80% was used for all the tests as this is the level of compaction that was planned to be used for the experiments of the current study. The method of achieving the correct relative density is further described in Appendix C.4.3.

The specimens were tested at 6 different normal stresses that can be categorised to low ($1.45 - 8.25$ kPa) and high ($74 - 194$ kPa) with regards to their magnitude. The group of low normal stresses was included in the testing programme as it is a representative stress level range of the situation expected during the experiments, however it was impossible to achieve normal stresses lower than 1.45 kPa. The high normal stresses were included as common practice values for DS box testing.

A strain rate of 1 mm/min was used initially and the tests took place in both dry and wet conditions. The wet tests were conducted on the group of high normal stresses only. This was because [11] suggested that the shear strength of sands, derived by DS box testing, should be the same for both dry and wet conditions due to the high permeability of sands which induces drained loading conditions. However, an intriguing observation that was made during testing was that the peak shear strength of the sand seemed to be lower in wet conditions. As this contradiction between the theory and practice was noted, the dry and saturated tests were repeated with a strain rate of 0.5 mm/min.

The results of dry and wet tests came into an agreement, as it is shown in Figure 4.10 once the strain rate was reduced. These differences obtained initially were attributed to the development of excess pore pressures during shearing. The latter was also an indication that the tests were not fully drained due to the low permeability of the soil. Therefore, it can be said that the sand used for the current study is susceptible to preventing drainage during shear loading in case this is not applied slow enough.

Interface tests were also conducted with the use of a steel plate which was blasted with aluminium silicate blast cleaning grit, in the same manner as it was done for the steel pipe. The surface roughness of the plate was measured with the means of a profilometer and an average roughness value of $R_a = 11$ μm (or 4.8% of D_{50}) was obtained. These measurements are available in Appendix C.4.3. The final results of the DS box tests are depicted in Figures 4.9, 4.10 and 4.11.

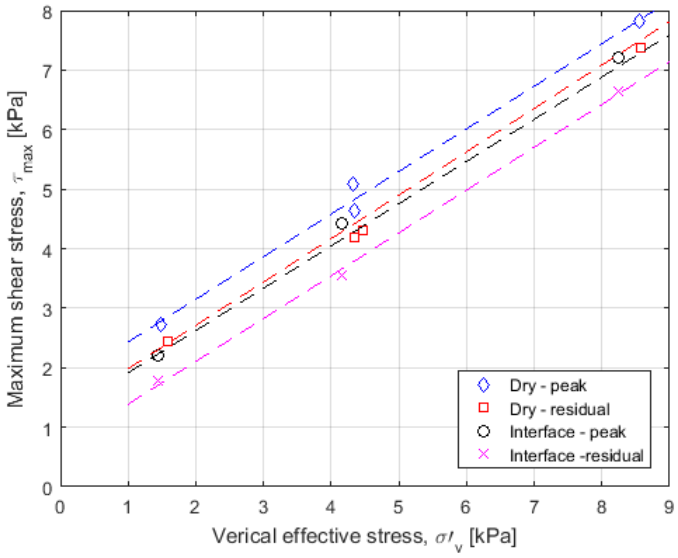

Figure 4.9: Peak and residual shear strength of dense uniform fine sand - dry and interface tests (low vertical effective stresses)

It can be seen that a higher friction angle was exhibited by the soil during the tests with the low stresses by comparing Figures 4.9 and 4.10. The latter also indicates the curvilinearity of the Mohr-Coulomb failure surface. The results of the dry and interface tests indicated a (peak and residual) friction angle of 35°. The results from the tests conducted at higher normal stresses showed that the peak and residual friction angle of the soil (in both dry and saturated conditions) was 34° and 28.5°, respectively. The results of the interface tests indicated that the steel surface was rough enough to mobilise the full shear strength of the soil as the same friction angle was obtained at both occasions.

Finally, the dilation of the sand was also examined and as it can be observed from Figure 4.11 the dilation angles (ψ and ξ) are found to decrease dramatically from 18° to approximately 11.3° as the normal stress increases from 1.45 kPa to 8.25 kPa. The latter

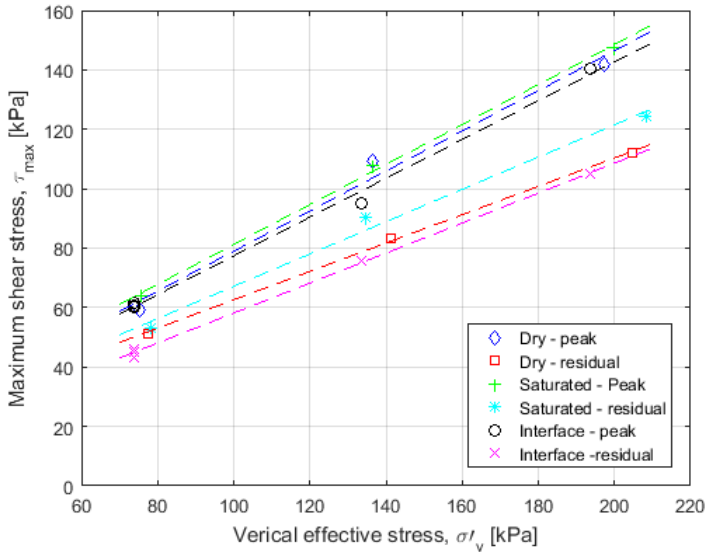

Figure 4.10: Peak and residual shear strength of dense uniform fine sand - dry, wet and interface tests (high vertical effective stresses)

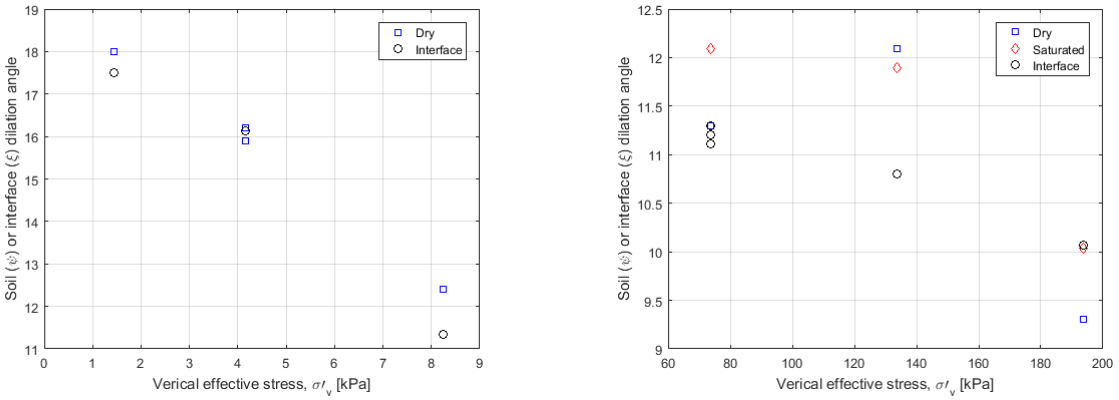

(a) Low stresses

(b) High stresses

Figure 4.11: Dilation of DS box samples at different vertical effective stresses

trend is then followed by slight decrease of dilation from 12.1° to 9.3° as the normal stress ranges from 74 to 194 kPa. It can be said that dilation of a granular soil is decreased as the in-situ stresses are increased, as it was also suggested by [16]. This effect was more visible at stress variations at the low levels as it was also notes by [18]. The above-mentioned results were also compared to Equation 4.1 provided by [6] and a good agreement was achieved using the peak, residual and dilation angles obtained from the tests conducted at high normal stresses. Additional details regarding the results of the DS box tests can be found in Appendix C.4.3.

$$\phi_p = \phi_r + 0.8\,\psi \tag{4.1}$$

Table 4.1: Soil parameters derived through sieving, density and DS box tests

Parameter	Meaning	Value
D_{10} [mm]	Maximum diameter of the smallest 10% of the sample	0.16
D_{30} [mm]	Maximum diameter of the smallest 30% of the sample	0.19
D_{50} [mm]	Average particle size	0.23
D_{60} [mm]	Maximum diameter of the smallest 60% of the sample	0.25
C_{u} [-]	Coefficient of uniformity	1.563
C_{c} [-]	Coefficient of curvature	0.903
$\rho_{\max}$ [kg/m^3]	Maximum density	1635.7
$\rho_{\min}$ [kg/m^3]	Minimum density	1379.3
$e_{\min}$ [-]	Minimum void ratio	0.620
$e_{\max}$ [-]	Maximum void ratio	0.900
G_{s} [-][1]	Specific gravity	2.65
$k_{\min}$ [cm/s][2]	Minimum permeability	0.096
$k_{\max}$ [cm/s][2]	Maximum permeability	0.250
$\phi_{\mathrm{p,l}}$ [°]	Peak friction angle at low normal stresses	35
$\phi_{\mathrm{r,l}}$ [°]	Residual friction angle at low normal stresses	35
$\phi_{\mathrm{p,h}}$ [°]	Peak friction angle at high normal stresses	34
$\phi_{\mathrm{r,h}}$ [°]	Residual friction angle at high normal stresses	28.5
ψ [°]	Dilation angle	$9.3 - 18$
$\delta_{\mathrm{p,l}}$ [°]	Sand-steel interface peak friction angle at low normal stresses	35
$\delta_{\mathrm{r,h}}$ [°]	Sand-steel interface residual friction angle at low normal stresses	35
$\delta_{\mathrm{p,h}}$ [°]	Sand-steel interface peak friction angle at high normal stresses	34
$\delta_{\mathrm{r,h}}$ [°]	Sand-steel interface residual friction angle at high normal stresses	28.5
ξ [°]	Sand-steel interface dilation angle	$9.3 - 18$

[1] Assumed after [27]

[2] Calculated empirically with Equation C.1

4.3 Sample preparation

Multiple techniques were considered initially for constructing specimens suitable for the current study. The test specimens were required to be good representatives of real life situations. As it was mentioned in Chapter 2, excessive pulling forces were observed at instances where the sand was at dense state. Consequently, the test specimens were aimed to be constructed at a relative density of 80% and their full saturation was essential. [15] has provided an overview of different sand deposition techniques for experimental purposes which are based on past experimental procedures. The following methods were considered for the current study and their suitability was assessed.

1. Air pluviation: Raining of the sand (in dry condition) in the testing tank from a specific height with a specific rate of deposition. The dropping height and rate of deposition are considered the two main factors that affect the final relative density of the sand sample. This technique is capable of simulating the natural deposition of aeolian deposits and a fair degree of uniformity can be achieved. The saturation of the specimens takes place once the sand mass is placed in the testing tank. As a consequence, uncertainties are caused regarding the degree of saturation especially for fine grained sands.

2. Water pluviation: Similarly to the Air pluviation technique, the sand is rained in the testing tank which already contains water. Therefore, full saturation of the sand

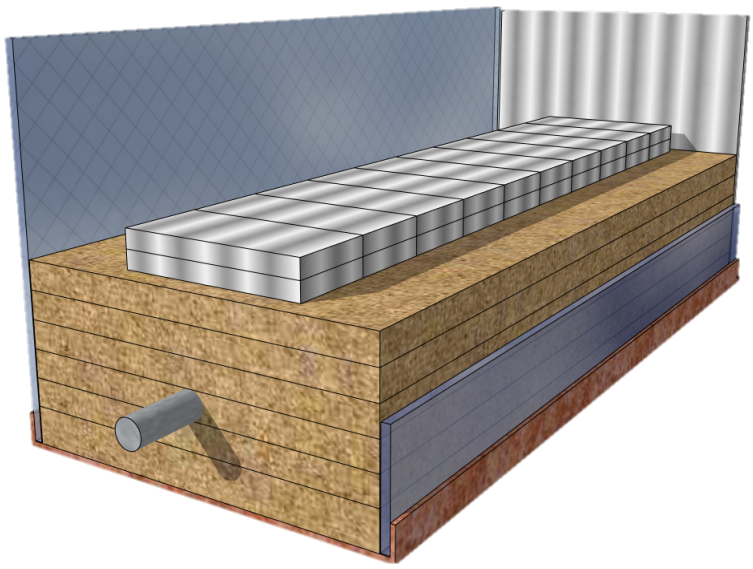

Figure 4.12: Layered construction of test specimens indicating two foundation layers, four soil layers, steel pipe and surcharge plates

mass can be achieved. The relative density that can be achieved is generally considered lower than the one that is achieved in air pluviated samples as the terminal velocity of sand particles in water is significantly lower than in air. In other terms, the deposition energy of the sand particles is lower. In addition, a good degree of uniformity can be achieved especially when poorly graded sand is used for the experiments. This technique is also good for simulating the natural deposition of sands in water.

3. Moist tamping: The placing of sand mass is done in a layered fashion. Layers of specific height, and therefore of specific volume and mass, are placed in the testing tank. Each layer is levelled and tamped for achieving the correct height and therefore the desired relative density. This technique is capable of producing very loose to dense samples, however their uniformity is under question as conflicting conclusions have been mentioned by [15].

It was observed that with any of the above-mentioned techniques there could have benefits and drawbacks regarding the structure and fabric of the sand samples. It was therefore decided that the most suitable technique for constructing the sand specimens for the current study would be moist tamping and a step-wise procedure is further described in Appendix C.5.

A correct relative density could be achieved in the same way as it was accomplished with the DS box tests and the layered construction of the specimens. In addition, full saturation of the samples could be achieved as the known soil mass would be submerged in water. Trapped air bubbles between the soil's grain can be compressed and therefore be led to the surface. The homogeneity of the samples was controlled by carefully tamping the newly deposited area and ensuring the correct levelling of each layer with the use of a sand scraper.

It was also found through literature that relative densities in the order of 80% - 100% can be achieved with this method. [25] stated that the heterogeneity of the samples might be higher in comparison to models prepared with other techniques (e.g. vibrational compaction). However, it was also mentioned that the homogeneity of these models is satisfactory for modelling Civil Engineering problems and validating numerical analyses.

The variables of the current study were the burial depth of the pipe (d) and pulling velocity (v_{pull}). The normalised burial depth over the pipe's diameter (d/D) was varied from 0 to 10.4. For the latter it has to be noted that after a depth of $3D$ (measured from the top of the pipe) steel plates were used on top of the soil as additional surcharge, as it is depicted in Figure 4.12. As a result, the placement of additional sand was avoided and the construction time was decreased.

The steel plates had dimensions of $200 \times 95 \times 20$ mm^3, weighed 3 kg each and one layer included 10 of them which were placed along the sand sample. As a result, a surcharge of 1.1 kPa was exerted at the depth of the steel pipe (accounting for the development of pressure bulbs) with the installation of each layer of steel plates. More details regarding the steps of preparing the test specimens can be found in Appendix C.5.

4.4 Testing programme

The d/D ratio was limited to 10.4 as, based on the experience by Allseas, the SWRs' embedment depths do not exceed 0.50 m. Considering the fact that the maximum diameter of SWRs used at landfall operations by Allseas is 0.08 m, it can be concluded that $d/D =$ 10.4 covered the needs of the current study. Burial depths of $6.7D$ and $10.4D$ were used for examining whether dilation takes place while the in-situ stresses increase further. Additionally, considering the fact that the pulling velocity of SWRs at landfall operations is 7 cm/s, it was decided to test the influence of this variable by conducting series of tests with 1, 4 and 7 cm/s. The testing programme of the current study can be found in Table 4.2.

Table 4.2: Experimental programme

Test Name	**Pulling velocity, v_{pull} [cm/s]**	**Normalised burial depth, d/D [-]**	**(Simulated)[2] burial depth, d [m]**	**Vertical effective stress, σ'_{v} [kPa][3]**	**Number of steel plate layers**
1_0	1	0	0	0	-
1_1		1	0.03	0.30	-
1_2		2	0.06	0.60	-
1_3		3	0.09	0.90	-
1_6.7 [1]		6.7	(0.20)	2.00	1
1_10.4		10.4	(0.31)	3.10	2
4_0	4	0	0	0	-
4_1		1	0.03	0.30	-
4_2		2	0.06	0.60	-
4_3		3	0.09	0.90	-
4_6.7		6.7	(0.20)	2.00	1
4_10.4		10.4	(0.31)	3.10	2
7_0	7	0	0	0	-
7_1		1	0.03	0.30	-
7_2		2	0.06	0.60	-
7_3		3	0.09	0.90	-
7_6.7		6.7	(0.20)	2.00	1
7_10.4 [1]		10.4	(0.31)	3.10	2

[1] Tested twice

[2] Burial depths in brackets were achieved with steel plates

[3] At the start of tests

4.5 Summary

The testing box along with the steel pipe including the pressure transducers are considered a suitable and innovative approach on determining the change of pore pressures on the sand-steel interface. The variation of pulling velocity on every experiment could be achieved with the selected motor and electronic system. Therefore, its influence to the change of pore pressures and maximum pulling force can be examined and one of the research sub-questions is answered.

Soil index testing showed that the sand used in the experiment is uniform,fine grained and susceptible to preventing drainage during shear loading at high rates. Assembling test specimens with a relative density of 80% and ensuring their homogeneity and full saturation was a significant part of the current study. The "moist tamping" technique was chosen as the most suitable sample preparation technique for achieving the above-mentioned specimen characteristics. Finally, the experimental testing programme included the variation of the steel pipe's burial depth and pulling velocity, which allowed for checking their effects on the pulling force and change of pore pressures on the sand-steel interface.

Chapter 5

Physical modelling - results

This chapter is dedicated to the examination of the results obtained during the experiments. Raw and processed results can also be found in Appendix D. Firstly, general observations are described providing information regarding the performance of the experimental setup and basic behaviours of the physical models. Secondly, the recorded results are examined and emphasis is given to the effects of the burial depth and the pulling velocity to the peak pulling force, change of pore pressures, residual pulling force and stiffness exhibited by the samples. Finally, the results are discussed and conclusions are drawn.

5.1 General observations

Trial tests were conducted prior to the initiation of the experimental programme. The aim of these tests was to determine the friction produced by the contact of the steel pipe with the testing tank as well as the contact of the pulling rope with the pulleys. It was shown that a force of approximately 25 N was produced and therefore this was subtracted from the measured force.

Also, it was observed that the PPTs located on the top side of the pipe did not produce any signals while the pipe was submerged or pulled. In order to neglect the possibility of attributing this fault to the pipe's positioning, another test was also conducted with the pipe rotated 180° which also gave the same indication. As a consequence, testing was continued with the use of 4 side sensors.

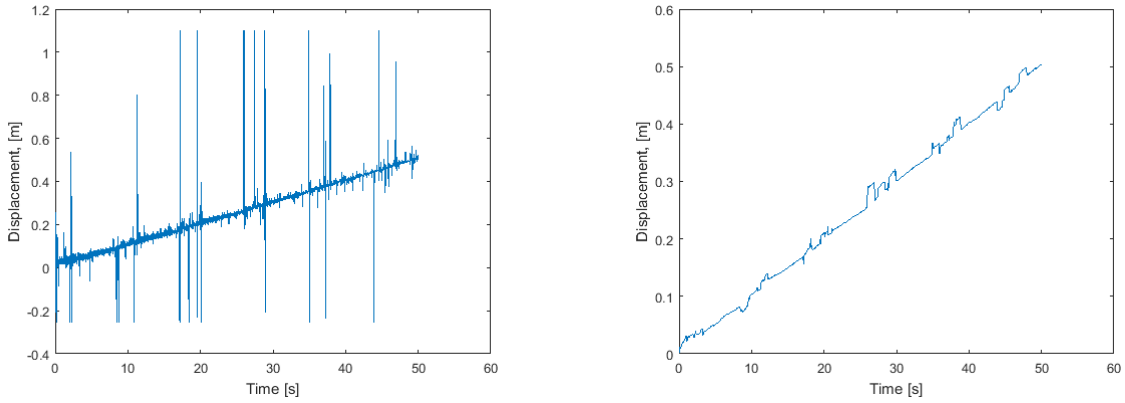

(a) Unprocessed signal

(b) Filtered signal

Figure 5.1: Recording of displacement, $d/D = 6.7$, $v_{\text{pull}} = 1$ cm/s

Additionally, it was observed that the draw-wire's signal was producing a high magnitude of noise as it is also shown in Figure 5.1a. This noise was attributed to the interference

of the high frequency signals produced by the load cell and the motor. Also, an effort to filter the signal produced by the draw-wire was made with the moving average technique. It was assumed that the pulling velocity was always constant and no acceleration took place during the pulling process as the variations in displacement data were attributed to noise. In addition, it can be observed that the signal produced extreme spikes periodically (approximately every 7 seconds) and this was due to the rotating gears and drum of the electric motor.

Consequently, the displacement data were disregarded and the pulling force was examined with respect to time as it is shown in Appendix D.1. The shape of these graphs was noted to always consist of a sharp peak which was followed by an instant decrease to the residual force at all pulling velocities, which came into an agreement with the statements of [21].

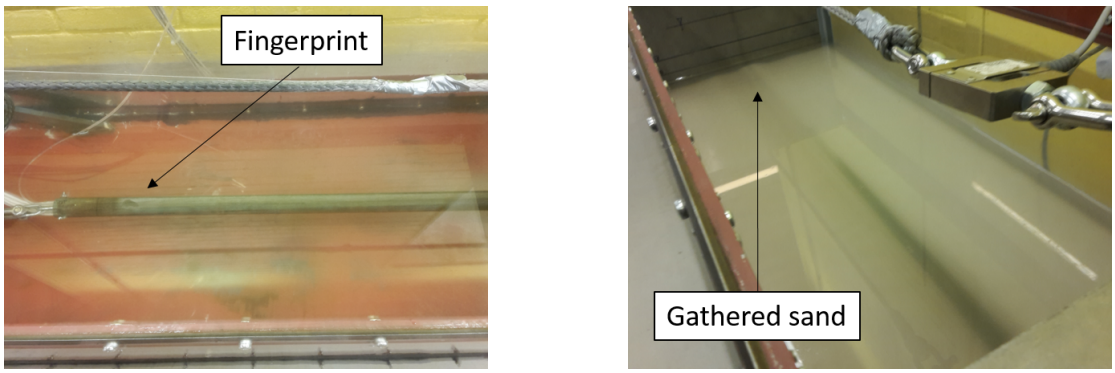

(a) Sand particles trapped on pipe (b) Dragging of sand

Figure 5.2: Shear failure and sand particle interlocking

Furthermore, shear failure always occurred between the sand particles and not on the sand-steel interface. This was attributed to the fact that the steel pipe had a rough surface capable of causing particle interlocking and therefore inducing soil shear failure. As it is observed in Figure 5.2a, sand particles were always found to be trapped on the steel pipe's indentations at the end of every experiment. The latter is also proven by an observation that was made at the experiments conducted at a normalised depth of $0D$. As it is depicted in Figure 5.2b, once the steel pipe was mobilised and particle interlocking took place on the rough indentations on the steel pipe's surface. As a result, part of the sand surrounding the steel pipe was dragged towards the end of the confined space following the direction of pulling.

In addition, the relative density of two samples was checked by installing a cylindrical container at a depth equal to that of the steel pipe. These two samples were prepared using the technique described in Appendix C.5 . The containers were extracted carefully after the end of the two tests, the excessive sand was scraped from the top of the containers and they were put in an oven (100 °C) overnight. The dry sand mass was measured the next day and relative densities of 79% and 82%, were calculated. Therefore, it can be said that this sample preparation technique performed well in producing samples with the desired relative density.

As it is illustrated in Figure 5.3, a decrease of pore pressures was noted at all the experiments and therefore all values $(-\Delta u)$ were plotted as positive. The peak pulling force was observed to occur at the same time as the peak of pore pressure reduction took place. This was a first indication that the reduction of pore pressures around the pipe influenced the force required to mobilise the steel pipe.

Finally, cavitation never took place, in contrast to what has been referred to by [20]. However, it was observed that the peak pore decrease was always followed by an instant

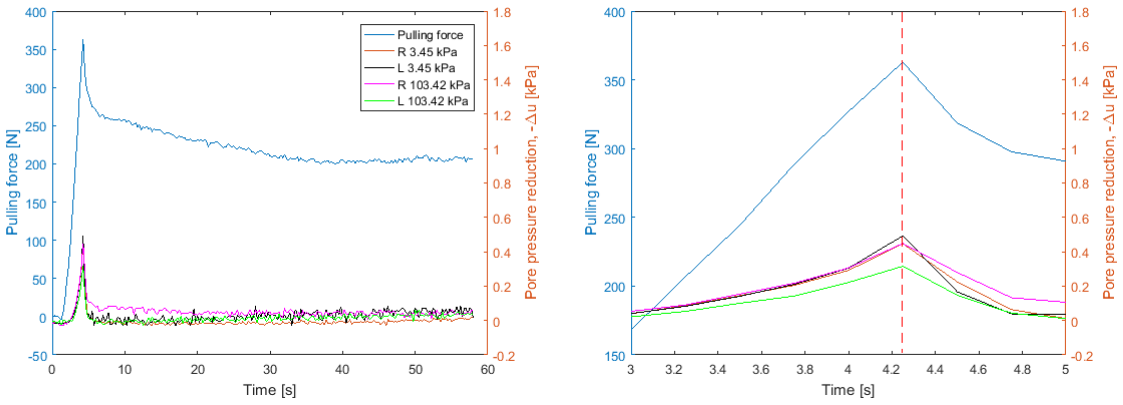

(a) Complete test recording

(b) Zoomed-in on the peak values

Figure 5.3: Peak force and peak pore pressure reduction occurring at the same time, $d/D = 6.7$, $v_{\text{pull}} = 1$ cm/s

decrease of the excess pore pressures and this indicated a transition from undrained to (partially) drained loading conditions.

5.2 Burial depth effect

Initially, it has to be noted that that the average values of the recordings were plotted in instances where two tests were conducted (i.e. 1_6.7 and 7_10.4). These values are always denoted in the following figures with the use of arrows, along with the actual recordings.

5.2.1 Peak pulling force

Figure 5.4 depicts the development of peak pulling forces versus the burial depth of the steel pipe, measuring from its top side. As it can be observed, the peak pulling force increased with the burial depth and this was due to the increase of the vertical effective stresses. It can also be said that the magnitude of the peak pulling force is higher while the pulling velocity is increased. In more detail, an average increase of 41.5% and 74.3% was noted for the tests conducted with 4 and 7 cm/s, in comparison to those conducted with 1 cm/s.

5.2.2 Peak pore pressure decrease

The pore pressure changes were measured by four sensors simultaneously while the pulling process took place. At all tests it was observed that the readings of all PPTs differed and this was attributed to the varying sensitivity of each of the sensors and possible soil inhomogeneity. These differences are depicted in Figures D.24-D.27. The maximum pore pressure reduction of all four PPTs, was selected and is presented in Figure 5.7. This was due to the assumption that this reduction was present around the circumference and along the effective length of the steel pipe.

Most of maximum pore pressure reduction values were recorded by L 3.45 kPa sensor which was a sensible outcome considering the fact that it was one of the two most sensitive pressure sensors. In contrast, R 3.45 kPa recorded only 2 maximum values (at tests 4_1 and 7_2), but always with a small deviation from the L 3.45 kPa sensor. In 4 tests (1_10.4, 4_6.7, 7_0 and 7_1) it was observed that the R 103.42 kPa sensor recorded the maximum values and this was attributed to possible inhomogeneity of the sand sample around the

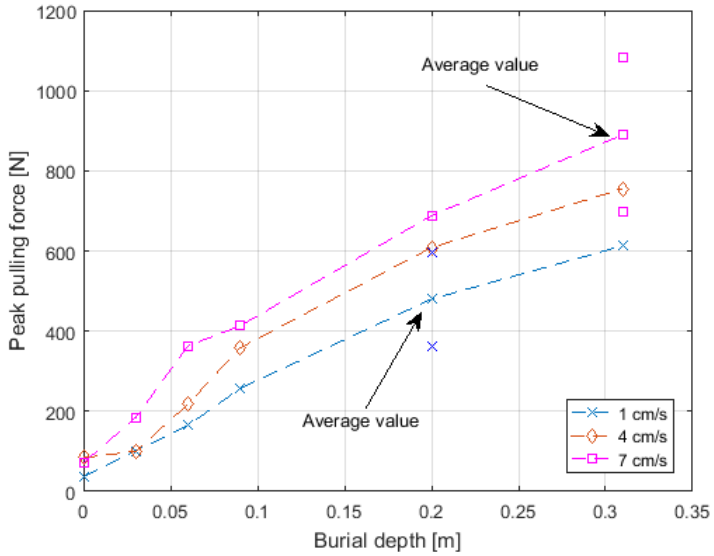

Figure 5.4: Peak pulling force with respect to burial depth, at different pulling velocities (dashed lines are linear interpolations)

area where the L 3.45 kPa and R 3.45 kPa were located. Lastly, the L 103.42 kPa sensor never recorded a maximum value.

Information regarding the change of pore pressures with respect to time can be found in Appendix D.2. The peak changes of pore pressures ($-\Delta u_{\max}$) on the sand-steel interface are presented in Figure 5.5. It can be observed that all the $-\Delta u_{\max}$ values recorded at the tests conducted with 1 cm/s vary along the 0.5 kPa line while a slight increase is noted at burial depths of 0.20 m.

In addition, it can be observed that the tests conducted with 4 cm/s yielded more significant decreases of pore pressures. An increase in the magnitude was noted as the burial depth varied from 0 to 0.09 m and a peak was reached at 1.56 kPa. This behaviour was unexpected as the tendency of soil to dilate is expected to be higher at smaller burial depths. However, it was impossible to conduct DS box tests with vertical effective stresses lower than 1.45 kPa and therefore this behaviour is considered unclear. Furthermore, a slight decrease was noted at approximately 1.1 kPa, as the burial depth increased from 0.09 m to 0.31 m.

A similar trend was also followed by the results obtained by the tests conducted with 7 cm/s. A peak of 2.6 kPa was noted at a burial depth of 0.09 m and moreover a gentle decrease was noted as the burial depth was increased to 0.20 m and 0.31 m. This behaviour was attributed to the decreasing fashion of the sand's dilation potential which is induced by the increase of vertical effective stresses, as it was also illustrated in Figures 2.6 and 4.11a.

An average increase of 86.0% and 270.6% in the magnitude of $-\Delta u_{\max}$ values was observed for tests conducted with 4 cm/s and 7 cm/s, in comparison to those conducted with 1 cm/s. As a result, it can be said that the pulling velocity always influences the peak pulling force, regardless the burial depth.

An increase of $T_{\max}$ was also observed by [21] when the pulling rate was increased. In addition, [13] also stated that the an increase of the shear strain results in a direct increase of a sand's dilation (potential), which can consequently induce higher tensile stresses in the pore water in case shearing takes place in undrained conditions.

Finally, it was also seen that when the pulling of the steel pipe was accomplished relatively slowly (i.e. 1 cm/s) then the decrease of pore pressures did not fluctuate signif-

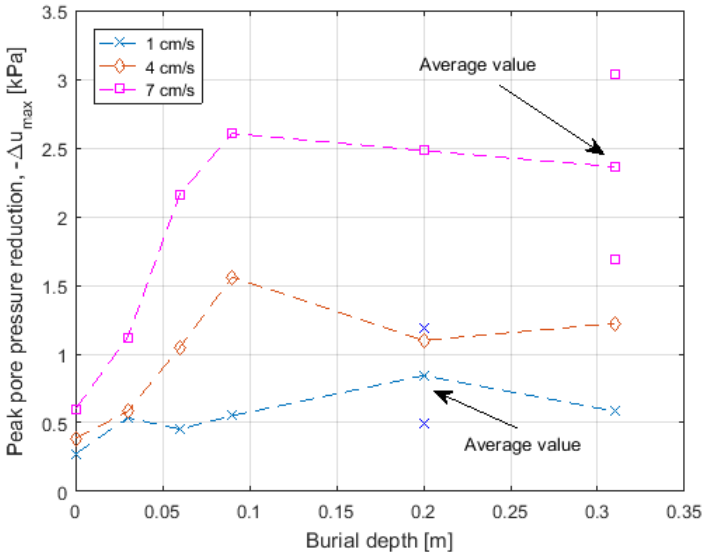

Figure 5.5: Peak pore pressure decrease, plotted as positive, with respect to burial depth, at different pulling velocities (dashed lines are linear interpolations)

icantly. This behaviour was due to the slower application of strains, in comparison to the tests conducted with 4 cm/s and 7 cm/s, which allowed for a smoother transition from undrained to (partially) drained loading conditions.

5.3 Pulling velocity effect

The pulling velocities used during the experiments varied from 1 cm/s to 7 cm/s. Consequently, the loading conditions encountered during the experiments were considered undrained as shearing took place at 1200-8400 times the drained shearing rate.

Drainage restrictions were noted during the DS tests in Section 4.2.3. It was shown that the differences between the results of dry and saturated specimens were due to the development of excess pore pressures at a shearing rate of 1 mm/min. This effect was diminished when the DS tests were repeated with a shearing rate of 0.5 mm/min, which was therefore condidered to induce drained loading conditions.

5.3.1 Peak pulling force

The effect of the pulling velocity to the peak pulling force is illustrated in Figure 5.6. As it can be observed from the trendlines, the pulling force increased linearly with the pulling velocity, for all burial depths. This was attributed solely to the fact that the peak values of pore pressure reduction increased linearly with the pulling velocity too, as it is shown in Section 5.3.2. In other terms, the increased magnitude of $-\Delta u$ caused an in increase of effective stresses around the steel pipe's perimeter and therefore increased the maximum pulling resistance, momentarily. In addition, the difference in peak forces' magnitude between all the burial depths was attributed to the naturally increasing in-situ soil stress which resulted to a higher shear resistance.

5.3.2 Peak pore pressure decrease

The change of peak pore pressure reduction with respect to the pulling velocity is depicted in Figure 5.7. Based on the trendlines, it can be said that the peak $-\Delta u_{\max}$ values

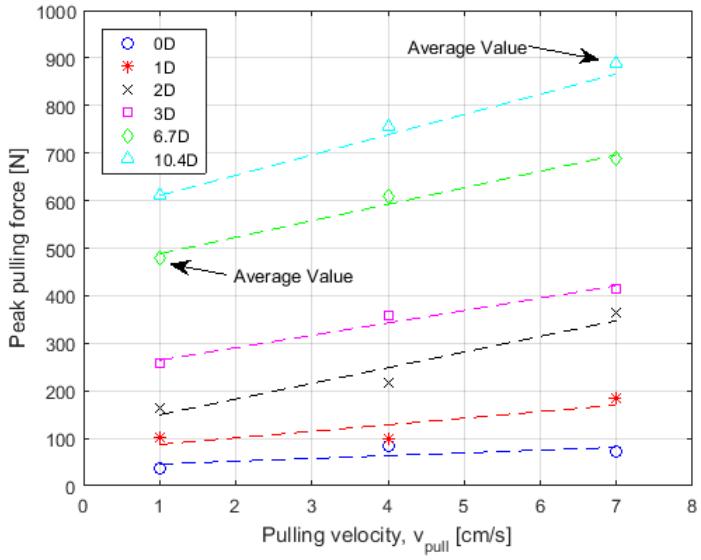

Figure 5.6: Peak pulling force with respect to pulling velocity, at different burial depths (dashed lines are linear trendlines)

increased linearly with the increase of the pulling velocity for each burial depth. This was attributed to the fact the shear load was applied more rapidly as the pulling velocity was increased and therefore higher tensile stresses developed.

An additional observation that can be made is that the rate at which the peak $-\Delta u_{\max}$ values increase becomes higher as the burial depth increases, up to a value of 0.09 m. Once the burial depth was increased from 0.09 m to 0.31 m ($3D - 10.4D$), a decrease of the trendlines' inclination was observed. This was attributed to the fact that the soil's dilation potential was restricted proportionally to the increase of the burial depth (i.e. vertical effective stresses).

Finally, the formulation of these trends could lead to the empirical quantification of the peak pore pressure reduction with respect to the pulling velocity, for each of the burial depths. The mathematical equations along with the corresponding correlation factors (R^2), describing the development of the trendlines presented in Figure 5.7, are provided in the following equations. The peak pore pressure decrease at intermediate depths of the ones tested can be obtained by averaging the slope gradient values and constant terms of two limiting equations. However, it has to be noted that this cannot be confirmed as an accurate approach due to limited number of experimental results obtained in this study.

$$-\Delta u_{\max,0D} = 0.0545\ v_{\text{pull}} + 0.2015,\ R^2 = 0.9708 \tag{5.1}$$

$$-\Delta u_{\max,1D} = 0.0973\ v_{\text{pull}} + 0.3569,\ R^2 = 0.8078 \tag{5.2}$$

$$-\Delta u_{\max,2D} = 0.2850\ v_{\text{pull}} + 0.0817,\ R^2 = 0.9703 \tag{5.3}$$

$$-\Delta u_{\max,3D} = 0.3423\ v_{\text{pull}} + 0.2029,\ R^2 = 0.9999 \tag{5.4}$$

$$-\Delta u_{\max,6.7D} = 0.2727\ v_{\text{pull}} + 0.3833,\ R^2 = 0.8641 \tag{5.5}$$

$$-\Delta u_{\max,10.4D} = 0.2964\ v_{\text{pull}} + 0.2044,\ R^2 = 0.9744 \tag{5.6}$$

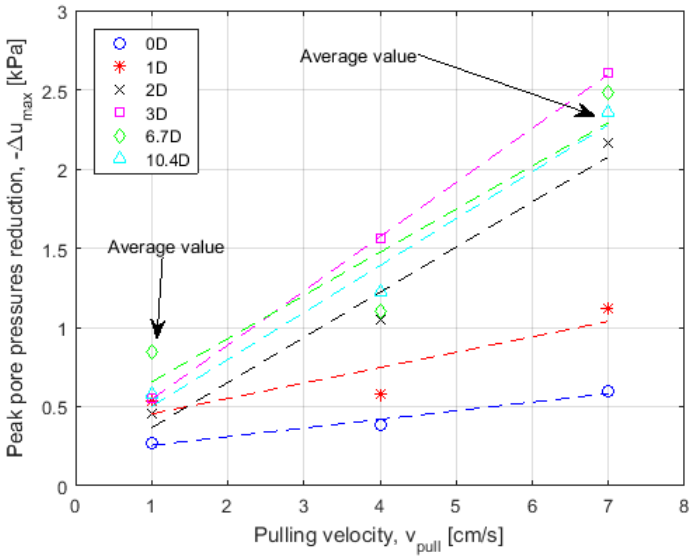

Figure 5.7: Peak pore pressure decrease, plotted as positive, with respect to pulling velocity, at different burial depths (dashed lines are linear trendlines)

5.3.3 Residual pulling forces

Figure 5.8 depicts the effect of the pulling velocity to the residual pulling forces obtained at each experiment. It was observed that at each pulling velocity the magnitude of residual forces was approximately the same and small deviations can only be attributed to the soil's inhomogeneity. This observation also came into a good agreement with the statement made by [21], in Section 2.3.2. This was an expected behaviour as the shear strength of the soil was expected to be the same while extreme deformations had taken place and the excess pore pressures had dissipated. Finally, as the burial depth increased the magnitude of residual pulling forces increased too due to the increase of the in-situ soil stresses.

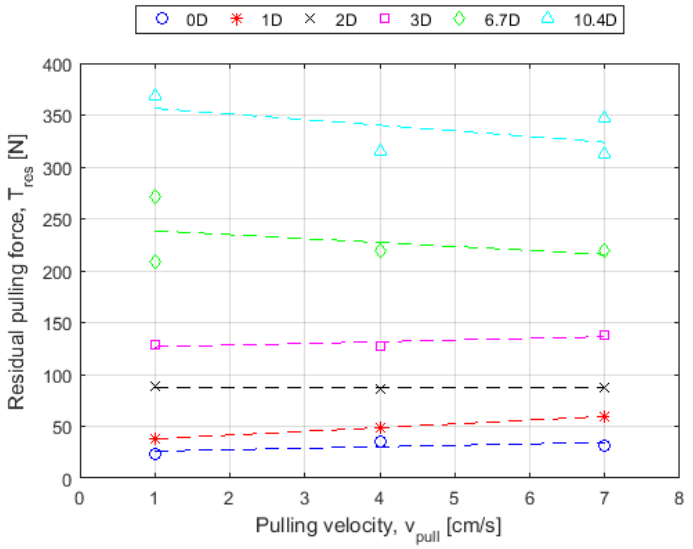

Figure 5.8: Residual pulling forces with respect to pulling velocity, at different burial depths (dashed lines are linear trendlines)

5.3.4 Soil stiffness index

An effort was also made to examine the elastic response of all the test specimens. As it was mentioned previously, the displacement data were disregarded due to the high noise levels produced by the draw-wire and therefore the actual exhibited stiffness could not be quantified. Figure 2.1 depicts the inclination of a tangent line to the 50% of the peak value obtained by the Force-Time curves(Figures D.1, D.2 and D.3).

By examining the development of the samples' stiffness index it could be said that at each burial depth a linear increase was noticed as the pulling velocity varied from 1 cm/s to 7 cm/s. Consequently, it can be said that an increase of the soil stiffness is expected to be noted in case pulling takes place with a larger velocity. This was attributed solely to the effects of pore pressure decrease, which took place at the same time as the pulling force. Finally, the increased stiffness at higher burial depths was due to the increase of the vertical effective stresses.

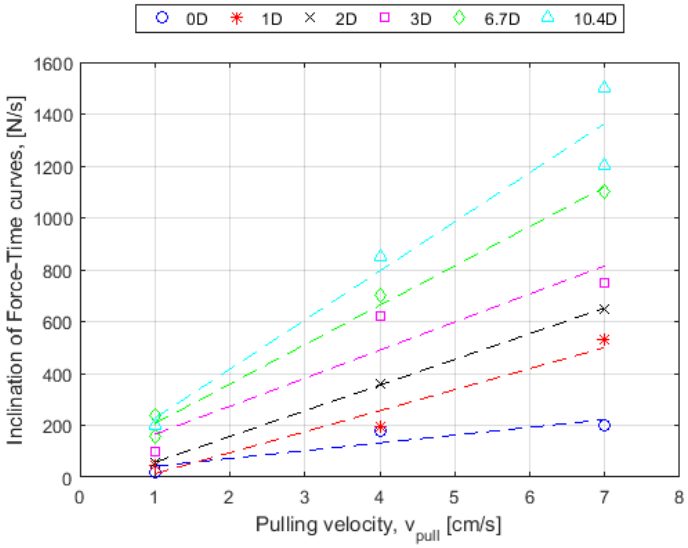

Figure 5.9: Inclination of Force-Time curves, calculated at 50% of peak pulling force, at different burial depths (dashed lines are linear trendlines)

5.4 Discussion

5.4.1 Methods of testing

Initially, it has to be mentioned that most experiments were not repeated due to time restrictions. The majority of tests exhibited satisfying results, at least in a qualitative manner, and two repetitions only took place because the initial results were considered unexpected. However, the repetition of all the tests is highly recommended for establishing more accurate interpretations of the trends of pulling forces and pore pressure changes. As it was also mentioned previously, the homogeneity of the samples was not perfectly controlled and therefore the repetition of the experiments could result to defining an error margin and average values of peak pulling forces and excess pore pressures.

The dimensions of the testing tank allowed for the construction of sand samples that were big enough that boundary effects can be neglected (e.g. restrictions of the shear band around the steel pipe, pressure bulbs developed by the steel surcharge plates in contact with the tank's walls). At tests conducted at a burial depth of 0 m, a small mass of sand was observed to be dragged towards the vertical separating plate. However, this could not

be quantified and therefore it was not involved in the determination of the pulling force. It was also observed that this sand mass was not present at the initial stages of the pulling process and therefore its effect on the peak pulling force can be neglected.

The relative roughness of the steel element, with respect to the grain size of the sand, was of high importance to the peak mobilisation force of the steel element. Based on the current case, sand grains were interlocked with the indentations of the rough steel surface which resulted on a sand-sand failure mechanism. This shear band which was located further from the sand-steel interface, was highly compacted and tended to dilate which resulted to the momentary decrease of pore pressures. However, the changes of pore pressures were measured from the steel pipe's surface and therefore it is possible that the true pore pressure reduction was not measured due to the distance from the shear band.

5.4.2 Elaboration on the results

Force-Time diagrams indicated that the pulling force and pore pressures increased as the pulling process was initiated and a peak was reached simultaneously by both. This behaviour was the first indication that the peak pulling force was directly influenced by the peak pore pressure decrease. These peaks were then followed by a dramatic decrease of magnitudes for both the pulling force and pore pressure readings, indicating a transition from undrained to (partially) drained conditions.

An expected observation that was made was that the maximum pulling force of the steel element was directly proportional to the burial depth. However, it was also noted that the pulling velocity played an important role to the maximum pulling force too. More specifically, it was observed that an increase in the pulling velocity resulted to a higher peak pulling force while the steel pipe was buried at the same depth. This was attributed to a larger decrease of pore pressures that took place during the pulling process which resulted in a momentary increase of the vertical effective stresses.

The decrease of pore pressures was noted to have a higher magnitude at depths ranging from 0 to 0.09 m, in comparison to depths ranging from 0.09 m to 0.31 m. This was an unexpected observation as the soil's tendency to dilate was expected to decrease with the increase of vertical effective stresses. At higher burial depths, increased soil stresses restricted soil's tendency to dilate and therefore the magnitude of pore pressure decrease was observed to decay. However, it was observed that the peak pore pressure decrease recorded at tests conducted with 1 cm/s was almost equal at all burial depths and this was attributed to the fact that shear strain rate was slow enough to allow for a smooth transition from undrained to (partially) drained loading conditions.

Moreover, the residual pulling forces were found to remain constant as the pulling velocity varied from 1 cm/s to 7 cm/s, for each of the tested burial depths. This came into an agreement with literature and it was attributed to the fact that the behaviour of a highly deformed soil is unaffected by the strain rate once it has reached a constant volume condition.

Last but not least, the pulling velocity was found to influence the shear stiffness index of the sand specimens. This was attributed solely to the decrease of pore pressures and an indication was given that the soil's elastic response is expected to be stiffer in cases when high pulling velocities are used.

5.5 Summary

To sum up, various aspects regarding the behaviour of the sand-steel interface were captured during this experimental study. During undrained loading, dilation of the shear band was restrained by tensile pressures that developed in the pore water. A transition

from undrained to (partially) drained loading conditions was always found to occur once the excess pore pressures reached a peak value. However, cavitation never took place, in contrast to literature findings.

It was natural to note the increase of resistance with the increase of the steel element's burial depth. However, the recording and examination of the change of pore pressures on the shear band that forms around the steel element was a unique and unconventional approach to the mechanisms that develop during the shearing of sand. Finally, it was intriguing to see that the maximum decrease of pore pressures was increased in magnitude up to a depth of 0.09 m as this was unexpected. At burial depths ranging from 0.09 m to 0.31 m the magnitude of excess pore pressures decreased due to the restriction of dilation.

Additionally, It was observed that the pulling velocity played an important role to the magnitude of the final pulling force that was required for the mobilisation of the steel element. Both the maximum pulling force and the peak decrease of pore pressures were found to increase linearly with the increase of pulling velocity at each burial depth. Finally, the decrease of pore pressures was also found to influence the exhibited soil stiffness of each of the tested specimens.

Chapter 6

Conclusions and recommendations

6.1 Conclusions

6.1.1 Experimental apparatus and instrumentation

One of the research aims of the current study was to develop a prototype experimental setup capable of simulating the pulling of a steel pipe through saturated sand. This was achieved with the testing tank presented in Chapter 4.

The separation of its internal part into three compartments allowed for the construction of confined sand specimens and extravagance of material was avoided. In addition, the relatively large dimensions resulted in the omission of boundary effects that could affect the experimental results. Openings on the separating plates, mounted with disk brush seals, allowed for the guidance of the steel pipe along the testing tank. This adjustment produced low friction forces and minimised the transfer of transfer from the middle compartment to the ones adjacent to it.

An additional requirement for this experimental setup was to record the changes of pore pressures around the steel pipe's perimeter while it was pulled through sand. The installation of PPTs on the steel pipe was an innovative and unique way of achieving this aim and therefore valuable information could be gathered regarding the shear failure mechanism around the steel pipe. Also, the steel pipe was blasted with silicon grit and an increased surface roughness was achieved. This resulted on an approximation of the rough surface of a SWR, capable of mobilising the full shear strength of the soil when the steel pipe was pulled.

The pulling of the steel pipe took place with an electric motor capable of producing a much higher pulling force than the maximum recorded force and therefore an accurate strain control was achieved. The pulling velocity was varied and controlled by fine tuning the MCS and the signals produced by the force and pressure transducers were recorded by the DAS.

Finally, the fine uniform sand used in this study was selected in accordance to the geological conditions met at the Noble Tamar and Shell Corrib projects, as provided by Allseas. Soil characterisation tests indicated that this fine sand could achieve relatively low values of permeability at high relative densities. In addition, it was indicated by the saturated DS tests that this sand had the tendency to restrict the drainage at a shearing rate of 1 mm/min. Interface DS box tests conducted with a steel plate blasted with silicon grate (i.e. same as with the steel pipe) indicated the full shear strength mobilisation of the soil.

6.1.2 Experimental results - pulling tests

The results yielded from the experimental study gave an insight regarding the behaviour of a fine sand at rapid shear loading (i.e. 1, 4, 7 cm/s) and the change of pore pressures around the steel pipe's circumference. Similar results were not found in literature and therefore it can be said that the dilation potential of sand and a consequent decrease of pore pressures in the shear band play an important role on the maximum mobilisation force of the steel element. Consequently, two more research questions were answered and the magnitude of the peak pulling force of a steel element is expected to be influenced by the following factors:

- Burial depth of the steel element (soil stresses)
- Soil relative density
- Tendency of soil to dilate
- Soil particle size (permeability)
- Pulling velocity

Due to the unfortunate event of high noise levels produced by the draw-wire only Force-Time diagrams allowed for analysing the experimental results. In addition, Pore pressure-Time diagrams indicated that there was a transition from undrained to (partially) drained loading conditions, once the peak pore pressure reduction was taking place. Also, it was observed that the peak pulling forces were found to take place at exactly the same time as the peak pore pressure reduction.

The surface of the steel pipe was always covered with sand particles at the end of every experiment. This indicated that during the pulling process the particles were interlocked with the rough indentations of the steel pipe's surface and therefore shear failure was taking place within the sand particles and not on the sand-steel interface. This also came into an agreement with the results obtained by the regular and modified DS tests and with the conclusions derived by [18].

Furthermore, the influence of burial depth and pulling velocity on the maximum pulling force were examined. It was natural and expected to observe an increase of peak pulling force while the burial depth was increased due to the increase of the vertical effective stresses. More importantly, it was interesting to see that the increase of pulling velocity caused an average increase of peak pulling forces in the order of magnitude of 41.5% and 74.3% at the tests conducted with 4 cm/s and 7 cm/s, in comparison to the tests conducted with 1 cm/s. It was observed that the peak pulling force, for each burial depth, was increased in a linear fashion with respect to the increase of pulling velocity. This behaviour was fully attributed to the corresponding peak pore pressure decrease.

It was also observed that the magnitude of peak pore pressures decrease, recorded at tests conducted with $v_{\text{pull}} = 4$ cm/s and 7 cm/s, increased while the burial depth increased from 0 m to 0.09 m. This was an unexpected behaviour as the potential of soil dilation was expected to be higher at lower vertical effective stresses. Moreover, a slight decline on the magnitude of peak pore pressure decrease was observed at burial depths ranging from 0.09 m to 0.31 m. This was attributed to the increase of vertical effective stresses and therefore to the decrease of the soil's tendency to dilate.

In contrast, the peak pore pressure reduction noted at tests conducted with $v_{\text{pull}} = 1$ cm/s seemed to be unaffected by the burial depth. In this case the strain rate allowed for a smoother transition from undrained to (partially) drained loading conditions and therefore lower pore pressure reductions took place.

In general, an average increase of peak pore pressure reduction in the order of magnitude of 86.0% and 270.6% was noted at tests conducted with $v_{pull} = 4$ cm/s and 7 cm/s, in comparison to the tests conducted with $v_{\text{pull}} = 1$ cm/s. Also, it was interesting to see that the peak pore pressure reduction values were increased linearly as the pulling velocity varied from 1 cm/s to 7 cm/s. The rate of increase was noted to rise for burial depths ranging from 0 m to 0.09 m and to decay at burial depths of 0.20 m and 0.31 m. The linear relationship between the peak pore pressure reduction and pulling velocity was expressed mathematically, aiming to an empirical quantification of this unprecedented effect.

Finally, it was observed that the residual pulling forces remained approximately constant at each burial depth, regardless the pulling velocity. This came in to a good agreement with the statements made by [21]. Also, it was indicated by the results that an increase of the pulling velocity can cause a stiffer response by the soil during the pulling process.

6.2 Recommendations

6.2.1 Physical modelling - Apparatus and analysis

The experimental results of the current study yielded important outcomes regarding the behaviour of sand during rapid shearing. Unprecedented results were obtained regarding the decrease of pore pressures on the shear band during the pulling process. Their effect to the maximum force required to mobilise a steel element buried in saturated sand was examined. However, the experimental variables were limited to the burial depth and the pulling velocity of the steel pipe. Therefore, the variation of the following parameters provide further research material.

- Particle size: Coarse sand tends to dilate more in comparison to fine sand and consequently higher tensile stresses are expected to develop in the pore water in case undrained loading can be achieved. However, the permeability of the soil will be bigger in comparison to fine sand and therefore drained loading conditions are more likely to take place within the tested pulling velocity spectrum.

- Relative density: Highly compacted sand results in a higher unit weight in comparison to a looser sand and as a consequence to a higher shear strength. In addition, highly compacted sand tends to dilate more than loose sand and this will have a direct consequence to the decrease of pore pressures during shearing.

- Pulling velocity: An effort to examine the pulling velocities that were omitted in the current research (i.e. 2, 3 and 6 cm/s) will provide better outcomes on how the peak pulling force is influenced by this variable. In addition, experiments with pulling velocities smaller than 1 cm/s can yield a critical pulling velocity which allows for the mobilisation of the steel element without causing significant pore pressure decrease.

- Burial depth: The examination of burial depths ranging from 0.09m to 0.20 m will yield information regarding the transition point where the peak pore pressure decreases ceases to increase in magnitude. Additionally, it would be interesting to determine the behaviour of pore pressure decrease at larger burial depths, where the dilation potential is expected to be reduced significantly.

- Roughness of steel element: The dilation potential of sand is proportional to the roughness of the steel element which interacts with it. In the current case, the steel pipe's outer surface was rough enough to mobilise the full shear strength of the

soil and therefore a rougher surface is not expected to yield higher pulling forces or lower pore pressures. However, a steel element with a smoother outer surface is expected to cause a smaller reduction of pore pressure. Also, the shear strength of the sand-steel interface is expected to be decreased as the soil particles will slide on the smooth surface and interlocking will be less acute.

- Diameter and type of steel element: A larger nominal diameter of the steel element is expected to yield higher pulling forces due to the increase of the contact area with the soil. In addition, the pore pressure reduction effect will also act on a larger surface, in comparison to smaller steel elements.

- Type of steel element: The use of a SWR can yield more information regarding the shear strength of the sand-steel interface and can therefore be compared with experimental results obtained with a steel pipe of the same size. However, a method of installing the PPTs on the SWR will be required.

A clearer picture on the decrease of pore pressures could be yielded by the installation of more PPTs in the steel element at more strategic locations on the steel pipe's circumference (i.e. top, side and bottom). The pore pressure reduction effect can be further examined with recordings at different positions around the steel element's perimeter. Also, absolute or gage sensors could be considered instead of differential and a sampling rate of 60-100 Hz is advised to be used. The latter can result in a more detailed examination of the pulling force development with respect to the pore pressure change.

The DS tests at low vertical effective stresses is recommended with the use of a more sensitive load cell. This can result in a more accurate analysis of the stress-strain results and therefore to a better derivation of the soil's behaviour at stress levels equivalent to the ones found in practice. Also, more detailed information regarding the dilative response of sand can be derived by extensive DS testing at low effective stresses.

The repetition of each experiment can provide a more accurate result and narrow down the effects of possible experimental errors. The most significant error that can source from an experimental study of this scale is the soil inhomogeneity and can lead to large deviations of the results.

Finally, pulling tests are recommended to be conducted at which the pulling process is to be initiated at the slowest possible rate, followed by a gradual increase in the pulling velocity once the pulling force is observed. The pore pressure reduction effect is expected to be minimised while following the above-mentioned testing method.

6.2.2 Expected behaviour of a steel wire rope

A SWR is expected to mobilise the full shear strength of the soil and this is due to its extremely rough and complex external surface. In general, higher pulling forces are expected to be obtained while using a SWR due to the deformation mechanisms that can develop while it is subjected in tensile loading. These deformations can result to local increases of the SWR's nominal diameter and therefore the area at which there is interaction with the soil. Consequently, the magnitude of pore pressure decrease is expected to be higher.

In addition, the screwing effect takes place at excessive tensile loading due to the spiral structure of SWRs. This effect is expected to result in an additional force component as torsional failure will also be required to occur prior to the mobilisation of the SWR. Also, the slender structure of a SWR can result on a curved placement within the soil specimen and therefore to a higher contact area with the soil.

Finally, the "loosening front" effect is expected to take place in case the SWR is buried in large depths or if it is pulled with a high pulling velocity. This can result to multiple

trials of pulling and releasing of the SWR before its whole length is mobilised. In addition, in this case it is more probable that excessive deformations will take place.

6.2.3 Analytical calculations

The development of an analytical model which accounts for undrained loading conditions is recommended to be developed for predicting the force required to mobilise a steel element which is buried in saturated sand. Based on the findings of this study, the following parameters should be considered while developing an this model.

- Burial depth
- Pulling velocity
- Steel element size (diameter/length)
- Pore pressure reduction effect
- Soil shear modulus
- Soil permeability/particle size
- Relative density
- Angle of internal friction
- Interface friction angle
- Dilation angle

6.2.4 Landfall operations practice

Prior to the initiation of a landfall operation project an extensive site investigation is recommended to take place along the project field. In this way engineering parameters of the soil can be derived and soil sampling can take place. Furthermore, simple laboratory tests (e.g. sieving, density, hydraulic conductivity and DS tests) can result to a more accurate characterisation of the soil which is expected to interact with the SWR. Therefore, enough data will become available for predicting the required pulling forces via analytical models.

The development of an experimental setup that will allow for prototype scale testing would be the ideal approach of predicting the magnitude of pulling force and pore pressure decrease around the SWR. Therefore, experimental studies could be conducted and the obtained results can be compared to data collected from landfall projects.

Finally, the most important recommendation is to initiate the pulling process with the lowest possible pulling velocity. As a result, the pulling force required to mobilise the SWR along with the pipeline will not be affected by the reduction of pore pressures. Once the whole system is mobilised then the pulling velocity can be gradually increased as shear failure will have taken place in the soil that interacts with the SWR. Therefore, the residual shear strength of the soil will be the dominant resistance component. Achieving the above-mentioned procedure it is required that the pulling velocity of the linear winch, located onshore, should be synchronised with the release velocity of the tensioners located on the pipe-laying vessel.

References

[1] Amer, A. & Awad, A. (1974). Permeability of cohesionless soils. Journal Of Geotechnical And Geoenvironmental Engineering, 100(GT12).

[2] Anaraki, K. (2008). Hypoplasticity Investigated: Parameter Determination and Numerical Simulation (M.Sc.). Technical University of Delft, Delft.

[3] Bardet, J. P. (1997). Experimental soil mechanics. Upper Saddle River, NJ: Prentice Hall.

[4] Bosch (Van den), M. (2013). Internship report - Steel wire rope-sand interaction. Delft: Allseas Engineering BV and University of Twente.

[5] Brinkgreve, R. B. J., Broere, W. (2006). Plaxis material models manual. Delft.

[6] Bolton, M. (1986). The strength and dilatancy of sands. Géotechnique, 36(1), 65-78.

[7] British Standards Institution (1996). BS 1377: Part 2: 1990 Methods of test for Soils for civil engineering purposes. Part 2. Classification tests. London: British Standards Institution.

[8] British Standards Institution (1996). BS 1377: Part 7: 1990 Methods of test for Soils for civil engineering purposes. Part 7. Shear strength tests (total stress). London: British Standards Institution.

[9] Castro, G. (1969). Liquefaction of sands (Ph.D.). Harvard University, Cambridge.

[10] Castro, G., Enos, J. L., France, J. W., & Poulos, S. J. (1982). Liquefaction induced by cyclic loading. NASA STI/Recon Technical Report N, 83.

[11] Das, B., (2015). Principles of foundation engineering. Cengage learning. Vancouver.

[12] Eurogrit.nl. (2016). Eurogrit aluminium silicate (coal slag grit) - Products - Sibelco Europe. Available at: `http://eurogrit.nl/uk_us/products/expendable_abrasives/eurogrit_aluminium_silicate_coal_slag_grit` [Accessed 25 May 2016].

[13] Healy, K. A. (1963). The dependence of dilation in sand on rate of shear strain (No. 13). Massachusetts institute of technology, Cambridge.

[14] Klooster, S. J. B. v. t., Prieelle, F. V. E. d., Riet, M. A. J. v. and Tsutsunava, N. (2015). Onderzoeksrapport Groep 120. Delft: TU Delft.

[15] Kuerbis, R. & Vaid, Y. (1988). Sand sample preparation - the slurry deposition method. Soils and foundations, 28(4), 107-118.

[16] Lee, K. (1965). Triaxial compressive strength of saturated sand under seismic loading conditions (Ph.D). University of California, Berkeley.

[17] Luo, S., Tan, S., & Yong, K. (2000). Pull-out Resistance Mechanism of a Soil Nail Reinforcement in Dilative Soils. Soils and foundations, 40(1), 47-56.

[18] Lings, M. & Dietz, M. (2005). The peak strength of sand-steel interfaces and the role of dilation. Soils and foundations, 45(6), 1-14.

[19] Luger, D. (2014). Pull-in wire ropes research. Rope-soil interaction model. Deflt: Deltares.

[20] McManus, K. and Davis, R. (1997) 'Dilation-induced pore fluid cavitation in sands', Géotechnique, 47(1).

[21] Morris, J. D. (1999). Physical and numerical modelling of grouted nails in clay (Ph.D). University of Oxford.

[22] Ottolini, M., Dijkstra, J., van Tol, F. (2014). Immediate and long-term installation effects adjacent to an open-ended pile in a layered clay. Canadian Geotechnical Journal, 52(7), 982-991.

[23] Panagoulias, S. (2015). Critical pressure during installation of suctions caissons in sand (M.Sc.). Technical University of Delft.

[24] Physical Properties. (2016). Marlowropes.com. Available at: `http://www.marlowropes.com/technical/physical-properties.html`. [Accessed 12 April 2016].

[25] Rietdijk, J., Schenkeveld, F. M., Schaminée, P. E. L., Bezuijen, A. (2010, June). The drizzle method for sand sample preparation. In Proceedings of the International Conference on Physical Modelling in Geotechnics 2010 (ICPMG 2010) (pp. 267-272).

[26] Schanz, T., Vermeer, P. A., Bonnier, P. G. (1999). The hardening soil model: formulation and verification. Beyond 2000 in computational geotechnics, 281-296.

[27] Smeets, C. (2013). Declarations of performance for aggregates for concrete and mortar (1st ed.). Dessel: SIBELCO Benelux. Available at: `http://www.sibelco.be/Web/Sibelcobe/Site.nsf/lwebkey/Sibelco_DoP_01_Kwartszand_Sort000000-S60/$File/DoP%20S60%20(EN-DE)%20v1.pdf?Openelement`. [Accessed 5 September 2016].

[28] Talmon, A. (2014). Pull-in wire ropes research. Factual report of pulling tests. Delft: Deltares.

[29] Wagner, A. (1957). The use of the unified soil classification system by the bureau of reclamation. In Fourth international conference on soil mechanics and foundation engineering. London. (Vol. 125).

Appendix A

Details from literature

A.1 Sand-steel interface strength and dilation

Table A.1: Legend explanation for Figure 2.5

Label	**Remark**	$R_{\max}$ [μ**m**]	$R_{\mathbf{a}}$ [μ**m**]
Shear	DS test with sand only	-	-
VLB	Pluviation of coarse sand on a uniform coating of Araldite smeared,across the steel surface	1320	180
MGS	Pluviation of medium sand on a uniform coating of Araldite smeared,across the steel surface	880	114
SFS	Pluviation of fine sand on a uniform coating of Araldite smeared,across the steel surface	202	33.7
SIC	Shot blasting with 16 grit silicon carbide (D_{50} = 1.8 mm)	67	9.4
ALO	Shot blasting with 120 grit aluminium oxide (D_{50} = 0.2 mm)	24.6	2.49
GND	Grinding wheel, with direction of striations perpendicular to,direction of shearing	3.85	0.356
POL	Abrasion of ground surface using abrasive paper	1.98	0.147

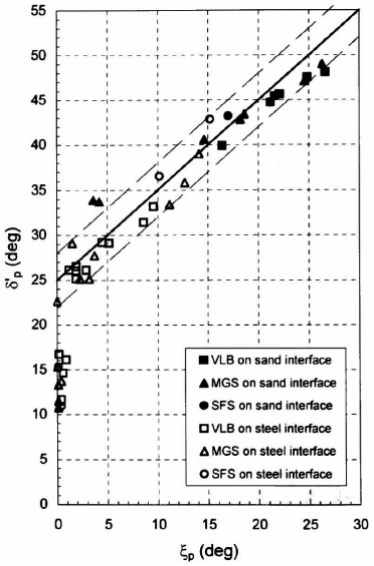

Figure A.1: Interface friction-dilation angles (VLB, MGS and SFS for coarse, medium and fine sands respectively) [18]

A.2 Decrease of pore pressures at shear bands

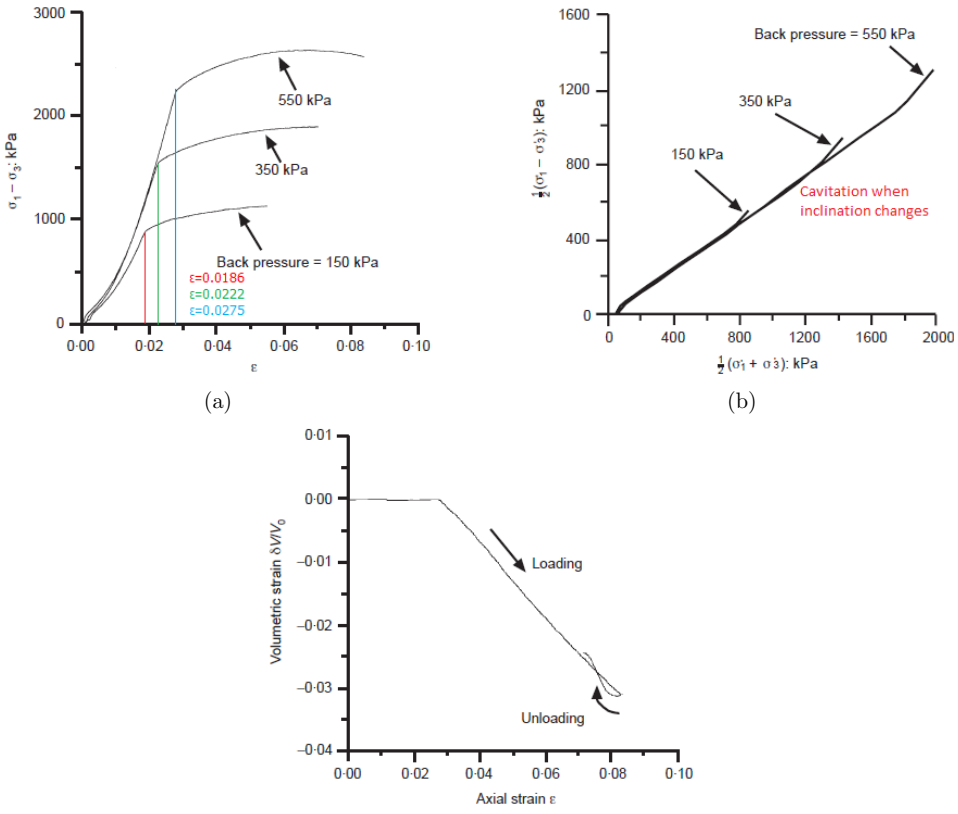

Figure A.2: (a) Undrained stress-strain response, (b) undrained pore pressure response, (c) Undrained volumetric strain response, (d) Undrained effective stress paths, (e) Undrained volumetric response during unloading for 550 kPa back pressure test.[20]

Appendix B

Analytical models

B.1 Klooster et al. (2015)

$$T_{\max} = \pi \; D \; l_{\mathrm{e}} \; \mu \; (\sigma_0 + \sigma_{\mathrm{B}} + \sigma_{\mathrm{L}} + \sigma_R) \tag{B.1}$$

With:

$$\sigma_{\mathrm{B}} = d \; (\gamma_{\mathrm{sand}} - \gamma_{\mathrm{water}}) \tag{B.2}$$

$$\sigma_0 = d \; (\gamma_{\mathrm{sand}} - \gamma_{\mathrm{water}}) + D \; (\gamma_{\mathrm{steel}} - \gamma_{\mathrm{water}}) \tag{B.3}$$

$$\sigma_{\mathrm{L}} = \sigma_{\mathrm{R}} = K_0 \; \sigma_{\mathrm{B}} \tag{B.4}$$

Where:

$T_{\max}$ = Pulling force [N]	l_{e} = Steel element length [m]
μ = Friction coefficient = $\tan \delta_{\mathrm{p}}$ [-]	σ_0 = Vertical effective stress (bottom) [Pa]
δ_{p} = Peak interface friction angle [°]	σ_{R} = Horizontal effective stress (right) [Pa]
D = Steel element diameter [m]	σ_{L} = Horizontal effective stress (left) [Pa]
d = Burial depth [m]	σ_{B} = Vertical effective stress (top) [Pa]
γ = Material unit weight [N/m^3]	K_{p} = Passive earth pressure [-]

B.2 Luo et al. (2000)

$$q'_{\max} = \lambda \tan \left\{ 3 \; I_{\mathrm{D}} \left[11.1 - \ln \left(\frac{1+\nu}{1-\nu} \sigma'_{\mathrm{v}} \right) \right] - 3 \right\} + \sigma'_{\mathrm{v}} \tag{B.5}$$

With:

$$\lambda = \frac{G u_{\mathrm{c}}}{r_0} \tag{B.6}$$

and

$$\frac{3(1-\nu)}{1+\nu} \; exp \left(10 - \frac{5}{I_{\mathrm{D}}} \right) \; < \; \sigma'_{\mathrm{v}} \; < \; \frac{3(1-\nu)}{1+\nu} \; exp \left(10 - \frac{1}{I_{\mathrm{D}}} \right) \tag{B.7}$$

Where:

λ = Dilation modulus [Pa]
I_{D} = Relative density [-]
ν = Poisson's ratio [-]
σ'_{v} = Vertical effective stress [Pa]
G = Soil shear modulus [Pa]
u_{c} = Critical shear displacement [m]
r_0 = Steel element radius [m]

B.3 Luger (2014)

The components that constitute the Deltares model are analysed in this section and information is provided regarding the background philosophy and derivation.

Equivalent surface friction factor, $\mu^\star$ [-]: It quantifies the effect that the soil and/or the steel element have at the total pulling resistance. As SWRs have rough surfaces and are constituted of thin strands, it was observed that sand particles were trapped between the SWR's strands, as it is schematically illustrated in Figure B.1. Hence, shear failure at the contact area can occur when sand particles slide on other sand particles or when the actual rope slides on sand particles. These effects are taken into account by quantifying the contribution of the soil (P_{sand}) and the steel element (P_{mat}) to the total shear resistance of the interface.

$$\mu^\star = P_{\mathrm{mat}} \ \tan\delta_{\mathrm{p}} + P_{\mathrm{sand}} \ \tan\phi_{\mathrm{p}} \tag{B.8}$$

Where:

P_{mat} = % of the sliding surface that runs over the steel element
δ_{p} = Peak interface friction angle [°]
P_{sand} = % of the sliding surface that runs through sand
ϕ_{p} = Peak soil friction angle [°]

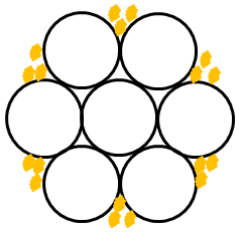

Figure B.1: Sand particles trapped between the strands of a SWR (schematic)

Rope self-weight effect, F_{w} [N/m]: The effective weight of the rope generates additional friction that needs to be taken into account.

$$F_{\mathrm{w}} = \mu^\star \ W \tag{B.9}$$

Where:

W = Effective weight of the of SWR per unit length [N/m]

SWR burial effect, F_Δ [N/m]: Additional friction is generated in case the rope is fully buried into the seabed because its whole perimeter is in contact with the soil. An overburden pressure is present because of the soil's effective weight.

$$F_\Delta = \pi \ D \ \mu^\star \ \sigma'_{\mathrm{n}\Delta} \tag{B.10}$$

With:

$$\sigma'_{\mathrm{n}\Delta} = (0.5 + 0.5\ K_0)\ d\ \gamma' \tag{B.11}$$

Where:

D = SWR diameter [m]
d = Embedment depth of steel element [m]
K_0 = 1 - $\sin\phi_\mathrm{p}$ = Earth pressure at rest [-]
$\sigma'_{\mathrm{n}\Delta}$ = Additional interface stress [Pa]
γ' = effective unit weight of soil [N/m^3]

Interface dilation effect, F_Ψ [N/m]: In case the soil around the wire rope is densely packed, it will dilate under shear loading, exerting additional stresses perpendicular to the SWR's perimeter.

$$F_\Psi = \pi\ D\ \mu^\star\ \sigma'_{\mathrm{n}\Psi} \tag{B.12}$$

With:

$$\sigma'_{\mathrm{n}\Psi} = \frac{G\ (R_\mathrm{g}^2 - R_0^2)}{R_\mathrm{g}^2} \tag{B.13}$$

$$R_0 = 0.5\ D + t \tag{B.14}$$

$$R_\mathrm{g} = R_0 + \Delta t \tag{B.15}$$

Where:

$\sigma'_{\mathrm{n}\Psi}$ = Additional stress due to dilation [Pa]
G = Shear modulus of soil [Pa]
R_g = Radius of cavity which contains the rope plus the dilated shear layer [m]
R_0 = Radius of cavity which contains the rope plus the shear layer [m]
t = Shear zone thickness [m]
Δt = Increase of shear zone thickness due to dilation [m]

Rope curvature effect, $F_\mathbf{c}$ [N/m]: Additional resistance is also expected in case the steel element is not installed in a levelled layout longitudinally.

$$F_\mathrm{c} = \frac{S\ \mu^\star}{R_\mathrm{c}} \tag{B.16}$$

Where:

S = Tensile force on SWR [N]
R_c = Radius of curvature [m]

(a) Hockling

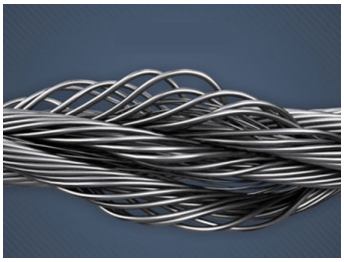

(b) Bird - caging

Figure B.2: Deformation mechanisms of SWRs resulting by extreme tension

B.4 Validation of the analytical models

B.4.1 Results obtained by Klooster et al. (2015)

Table B.1: Experimental rresults obtained by [14] with D = 6 mm steel elements

	$T_{\max}$ [N]	
Burial depth [m]	**Rod**	**SWR**
0.000	1.242	1.309
0.025	6.640	14.837
0.050	17.861	54.385
0.075	30.829	74.919
0.100	40.141	115.250
0.150	59.751	252.507

B.4.2 Notes on the Hardening Soil model

Information regarding the advantages and disadvantages was extracted from [5] and [26]. It was observed that the HS model was not the most suitable choice as it lacks several key characteristics that apply for the situation of the pulling process.

The HS model is commonly used in engineering practice and it simulates the critical state of soils with the use of the angle of internal friction (ϕ_{p}), cohesion (c) and angle of dilation (ψ). One of its greatest advantages is that the soil's stiffness is characterised by the triaxial loading stiffness (E_{50}), triaxial unloading stiffness (E_{ur}) and oedometer loading stiffness (E_{oed}). It does not account for large stiffness at small strains and reduced stiffness at higher strains. As it was shown through literature the mobilisation of the steel elements is considered to occur at small strains and after that stage softening is noted which is then followed by the residual shear strength of the soil.

As a result, the "Hardening Soil model with small-strain stiffness" (HSsmall) seems to be more suitable for this application as it accounts for the increased stiffness of soils at small strains. Its basic principle is that at small strains a higher stiffness is exhibited

Table B.2: Analytical results obtained by [14] with D = 6 mm steel elements

	$T_{\max}$ [N]	
Burial depth [m]	**Rod**	**SWR**
0.000	0.448	1.000
0.025	3.329	9.329
0.050	7.923	17.658
0.075	11.661	25.987
0.100	15.398	34.316
0.150	22.873	50.975

in comparison to engineering strain levels and the transition between the two stages is non-linear. It is also suggested that the shear modulus of a soil decreases by 30% when the transition from the small strains to the larger strains occurs.

Appendix C

Physical modelling - apparatus materials and methods

C.1 Testing box

The layout and dimensions (in mm) of the testing box are shown in the figures below. As it can be observed, the steel frame constitutes the load bearing part of the structure and has dimensions of $2.50 \times 0.43 \times 0.40$ m^3. The side walls are made of acrylic sheets that are bolted on the steel frame.

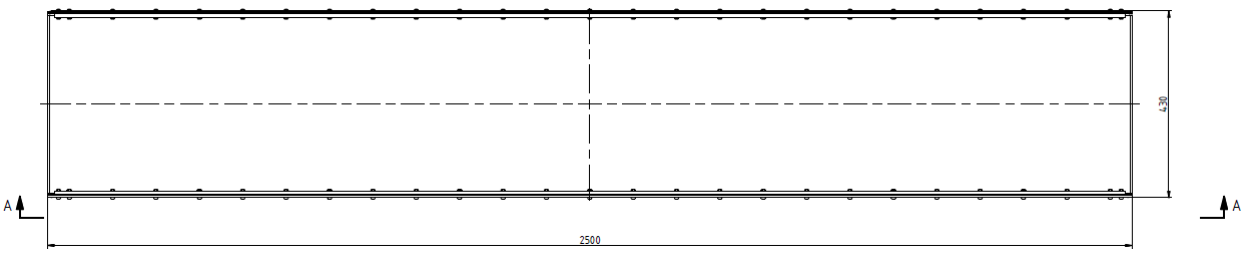

Figure C.1: Testing box prior to modifications - top view

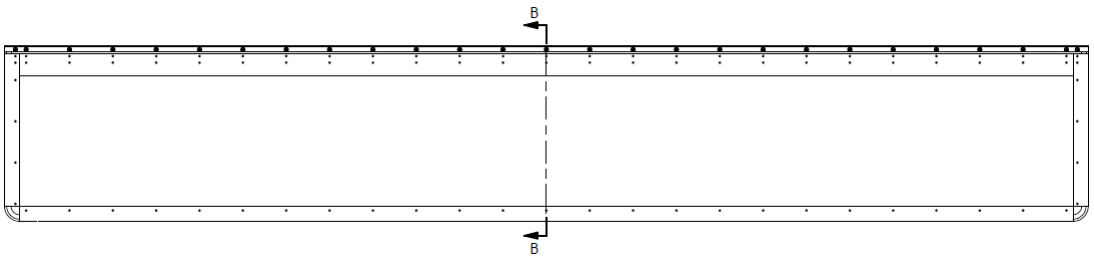

Figure C.2: Testing box prior to modifications - elevation AA

The modifications and additions that took place for the needs of the current study are depicted below in Figures C.4, C.5 and C.6. It can be seen that two separating plates (Item 9) were added in the box and therefore three compartments were created. In addition, a reinforcement plate (Item 11) was attached on the box's wall and it allowed for the installation of two pulleys (Item 15). A steel plate was also introduced for supporting the electric motor (Item 10). The winch plate was constituted of a steel plate with two hollow steel beams that allowed the motor be on an elevated position and an eye which assisted on the creation of a pulling loop. Two steel beams (Item 17) were used for supporting the winch plate.

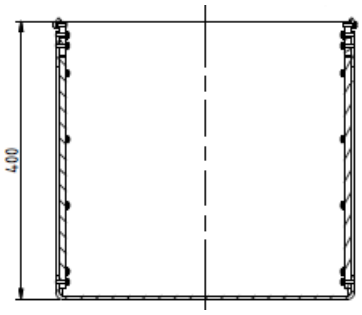

Figure C.3: Testing box prior to modifications - cross section BB

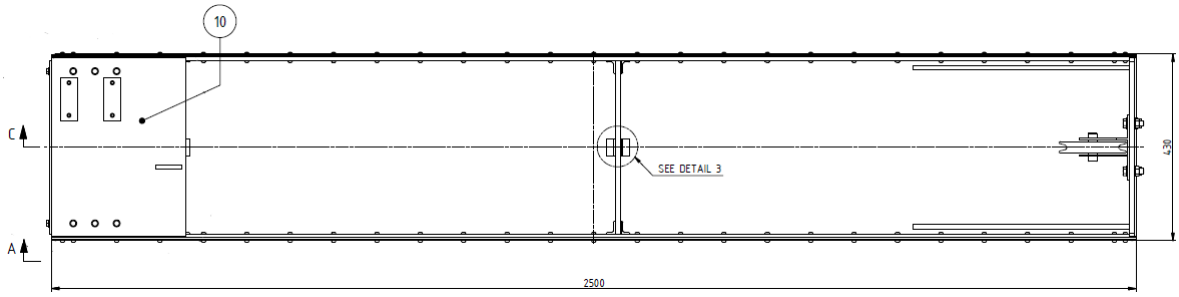

Figure C.4: Testing box after modifications - top view

Furthermore, as it can be observed by Figure C.7 the separating plates were installed with the use of steel guides that were welded on the box's sides and base. The use of these guides allowed for a secure fixation of the separating plates and easy disassembly. Also, a hole with a diameter D = 60 mm was created through the separating plates to allow the pulling of the steel pipe through all the compartments.

Item 11 is depicted in Figure C.8. This part was installed on the testing box's side wall and allowed for the installation of the two pulleys (Item 15). In addition the stiffness of the box's vertical wall was increased and bending was minimised during the pulling process. The reinforcement plate was also supported by two steel beams that were founded on the box's bottom plate.

The winch plate (Item 10) is shown in Figure C.9. As it can be observed it is constituted of a steel plate which is modified for the installation of the electric motor. Two hollow sections were welded on the indicated position and allowed for the bolting of the motor. This position was chosen with respect to the motor's geometry so that to allow the rotating drum to be situated on the box's symmetry line. In addition, the steel eye was installed parallel to the symmetry line of the box so that the pulling rope was not tangled while it was spooled in the motor's drum. Finally, six holes allowed for the bolting of the winch plate on the supporting blocks that are depicted in Figure C.10.

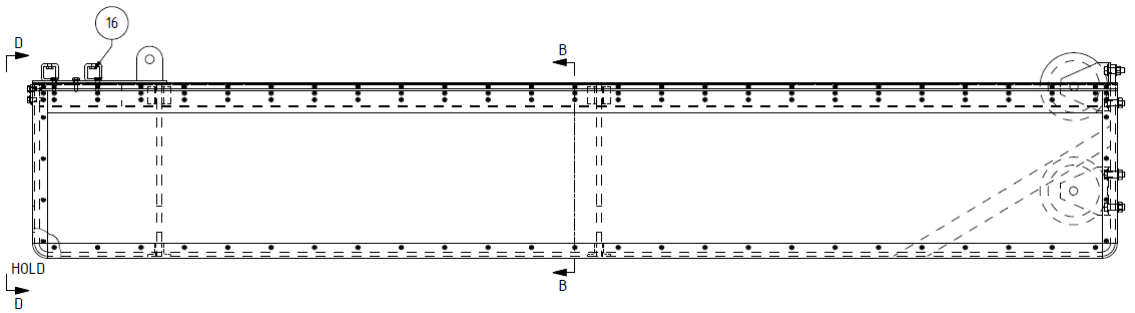

Figure C.5: Testing box after modifications - elevation AA

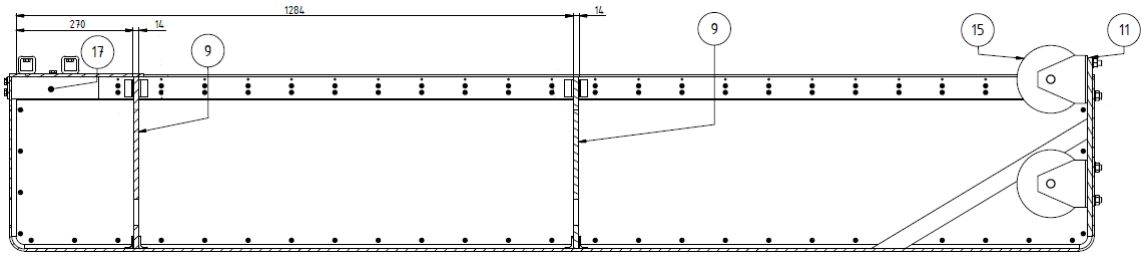

Figure C.6: Testing box after modifications - cross section CC

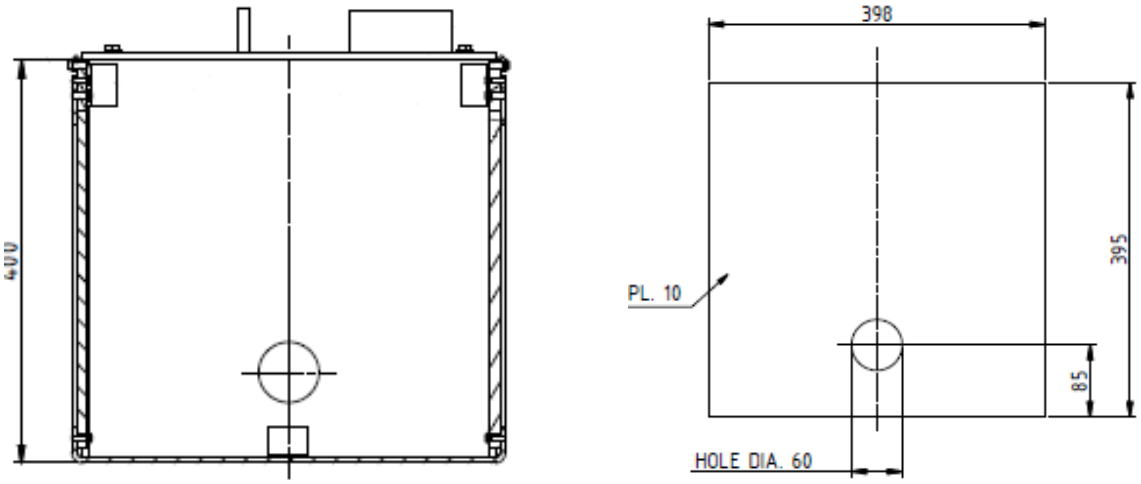

(a) Cross section BB

(b) Plate dimensions

Figure C.7: Separating plate (Item 9)

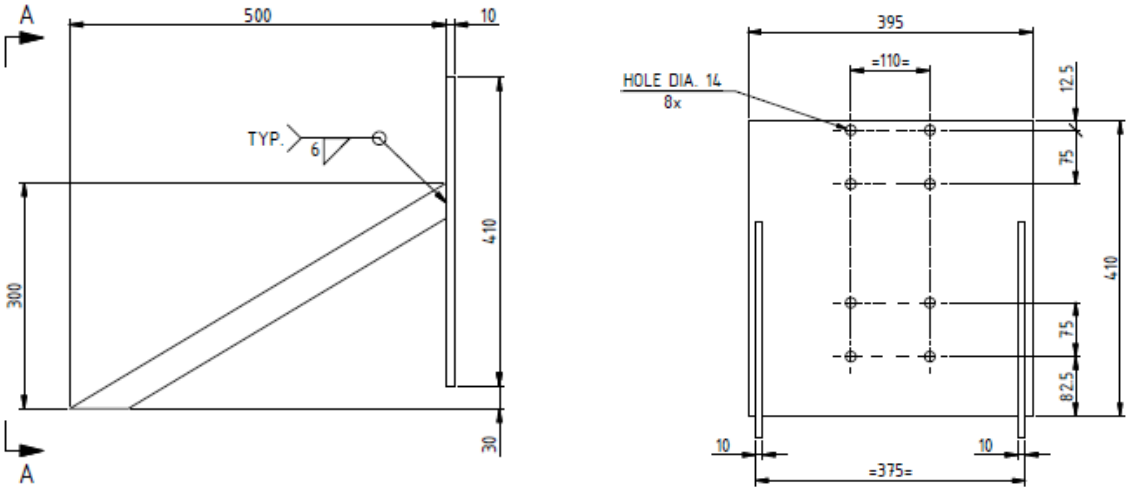

(a) Side view (b) Elevation AA

Figure C.8: Reinforcement plate (Item 11)

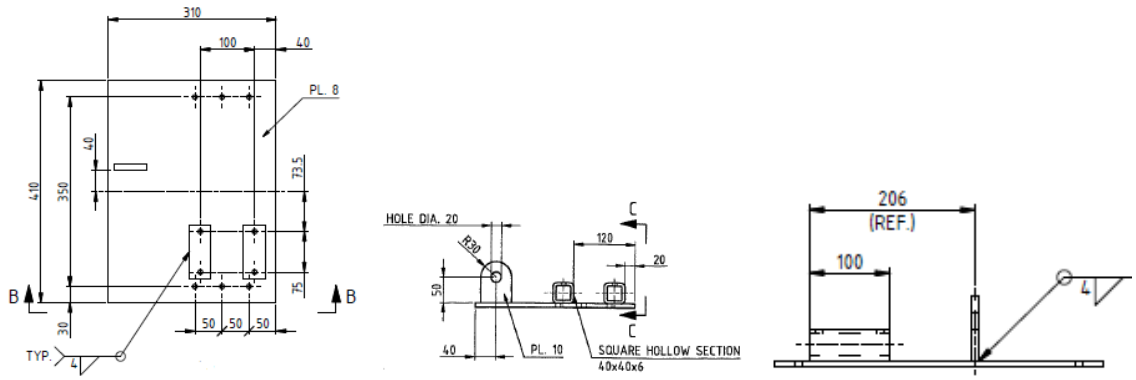

(a) Top view (b) Elevation BB (c) Elevation CC

Figure C.9: Winch plate (Item 10)

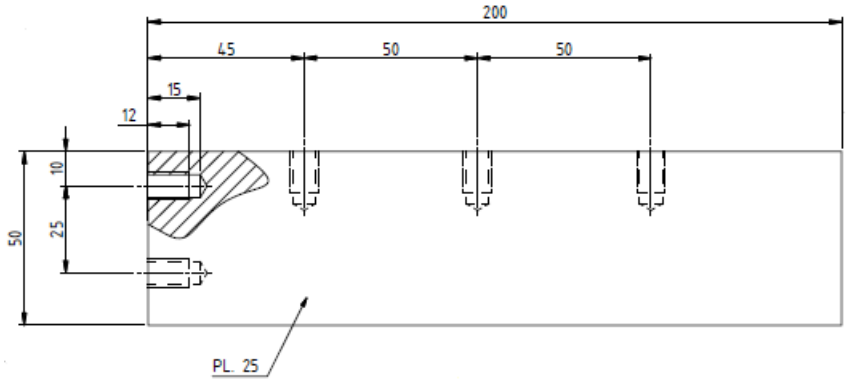

Figure C.10: Support block for the winch plate (Item 17)

C.2 Electric motor

The schematic drawings were provided by the manufacturer of the electric motor and the dimensions are presented in millimetres.

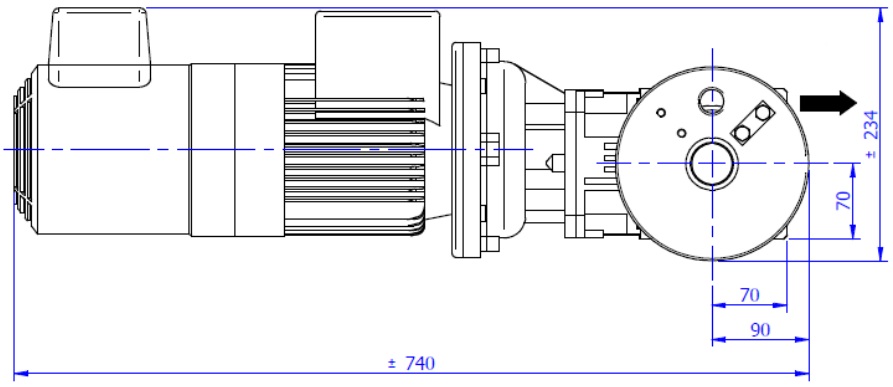

Figure C.11: Side view of electric motor (source: EMCÉ WINCHES®)

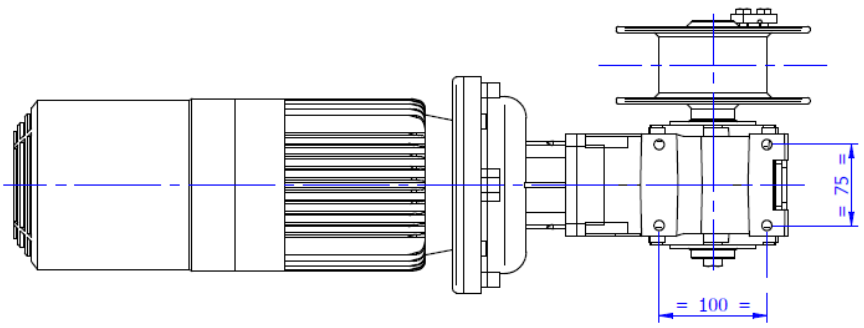

Figure C.12: Bottom view of electric motor (source: EMCÉ WINCHES®)

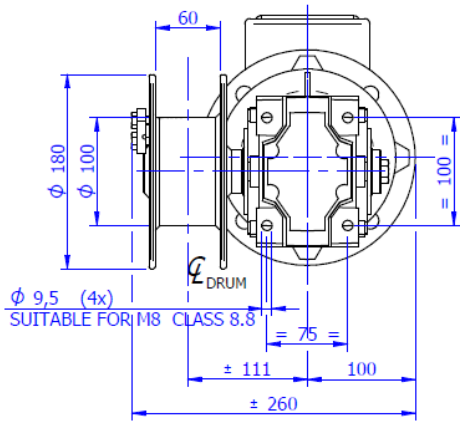

Figure C.13: Front view of electric motor (source: EMCÉ WINCHES®)

C.3 Pressure transducers

Table C.1: Technical specifications of pressure transducers

Pressure range [kPa]	Span [mV]			Sensitivity [mV/kPa]	Maximum overpressure [kPa]
	Minimum	Typical	Maximum		
±3.45	24	35	46	10.15	137.90
±103.42	165	225	285	2.18	310.26

C.4 Soil characterisation

C.4.1 Determination of particle size distribution

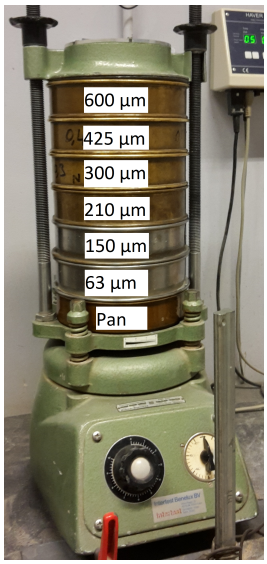

Figure C.14: Sieves assembly and vibrating table used for determining the soil's particle size distribution

C.4.2 Determination of maximum and minimum density

Figure C.15: Aparratus used for obtaining the maxiumum and minimum density of the soil based on [2]

The permeability of cohessionless materials has been studied in the past by [1] and it was shown that an the soil's permeability can be calculated with Equation C.1. In this case the soil's permeability is a function of the soil's void ratio (e), coefficient of uniformity (C_u) and D_{10}. As a result, the minimum (k_{min})and maximum (k_{max}) permeability of the soil was calculated to be 0.096 cm/s and 0.250 cm/s, respectively.

$$k(\mathrm{cm/s}) = 35 \left(\frac{e^3}{1+e} \right) C_{\mathrm{u}}^{0.6} \, D_{10}^{2.32} \tag{C.1}$$

C.4.3 Determination of shear strength (small shear box)

Specimen preparation

The preparation of test specimens for the DS tests was based on the soil parameters obtained through the density tests which can be found in Table 4.1, $e_{\max}$ and $e_{\min}$. As the limiting void ratios of the soil were known a specific value for the relative density of the specimens could be calculated with Equation C.2.

$$I_{\mathrm{D}} = \frac{e_{\max} - e}{e_{\max} - e_{\min}} \tag{C.2}$$

Then a specific void ratio (e) was extracted which was the representative void ratio for that specific value of relative density. A value of specific gravity (G_s) of 2.65 was assumed for the sand used in the current study as it is suggested by [11] for quartz sands. Using Equation C.3 the exact mass that had to be used in the DS tests was calculated, taking into account the volume available in the shear box (420 cm^3).

$$\gamma_{\mathrm{d}} = \frac{G_{\mathrm{s}} \gamma_{\mathrm{w}}}{1+e} \tag{C.3}$$

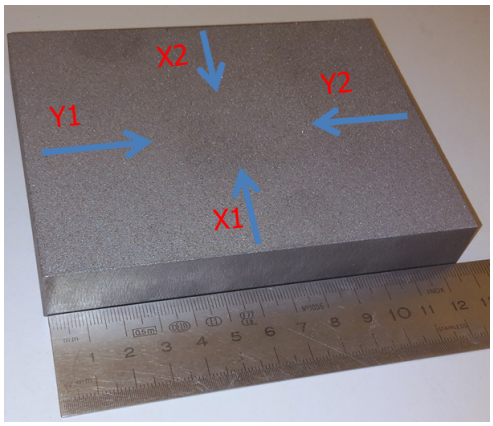

Figure C.16: Steel plate used for the modified DS box tests with sand blasted surface (positions and directions of profilometer measurements indicated with labels and arrows, respectively)

Results

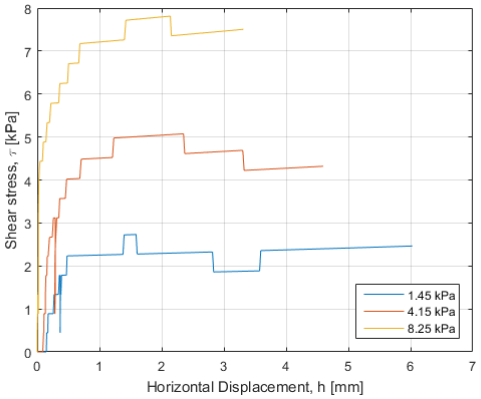

Figure C.17: Shear stress and horizontal displacement of dry specimens loaded with low normal stresses

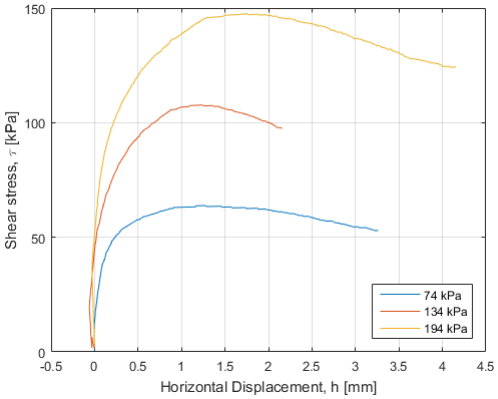

Figure C.18: Shear stress and horizontal displacement of dry specimens loaded with high normal stresses

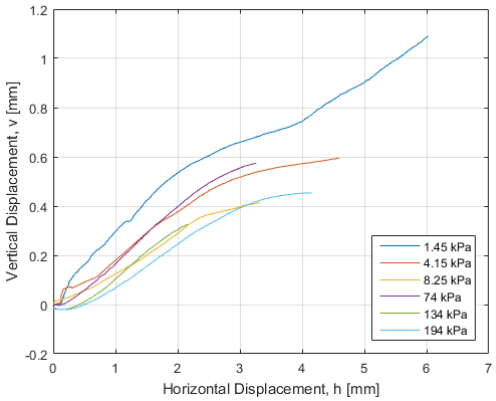

Figure C.19: Dilative response of dry specimens

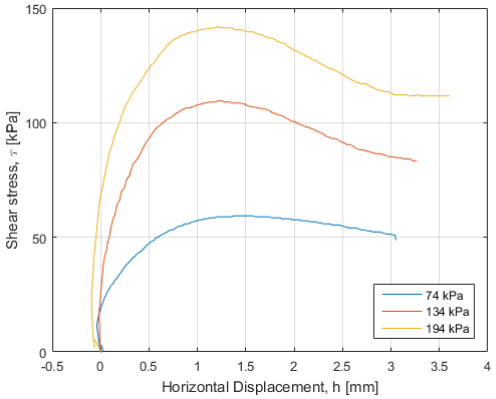

Figure C.20: Shear stress and horizontal displacement of saturated specimens loaded with low normal stresses

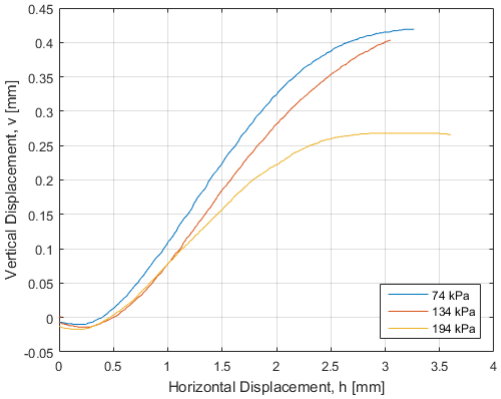

Figure C.21: Dilative response of saturated specimens

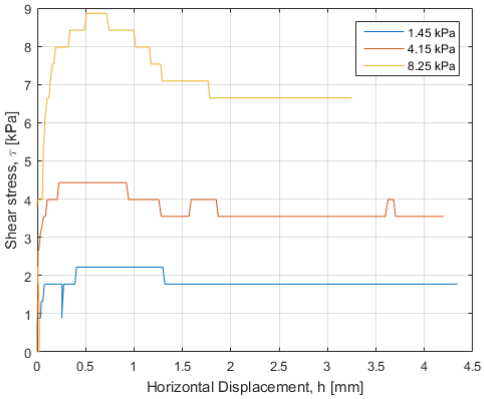

Figure C.22: Shear stress and horizontal displacement of interface tests loaded with low normal stresses

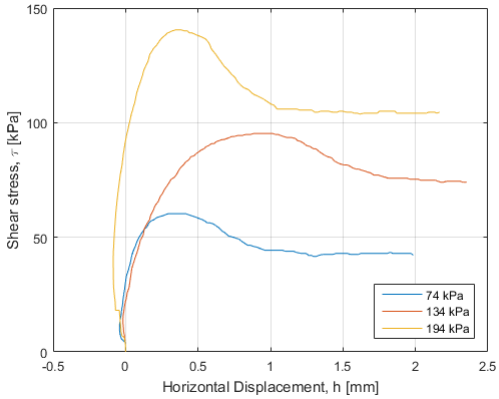

Figure C.23: Shear stress and horizontal displacement of interface tests loaded with high normal stresses

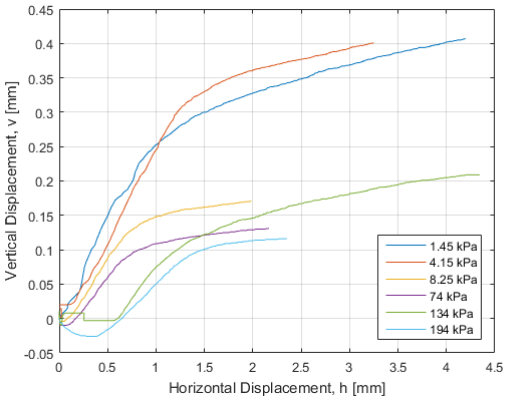

Figure C.24: Dilative response of interface tests

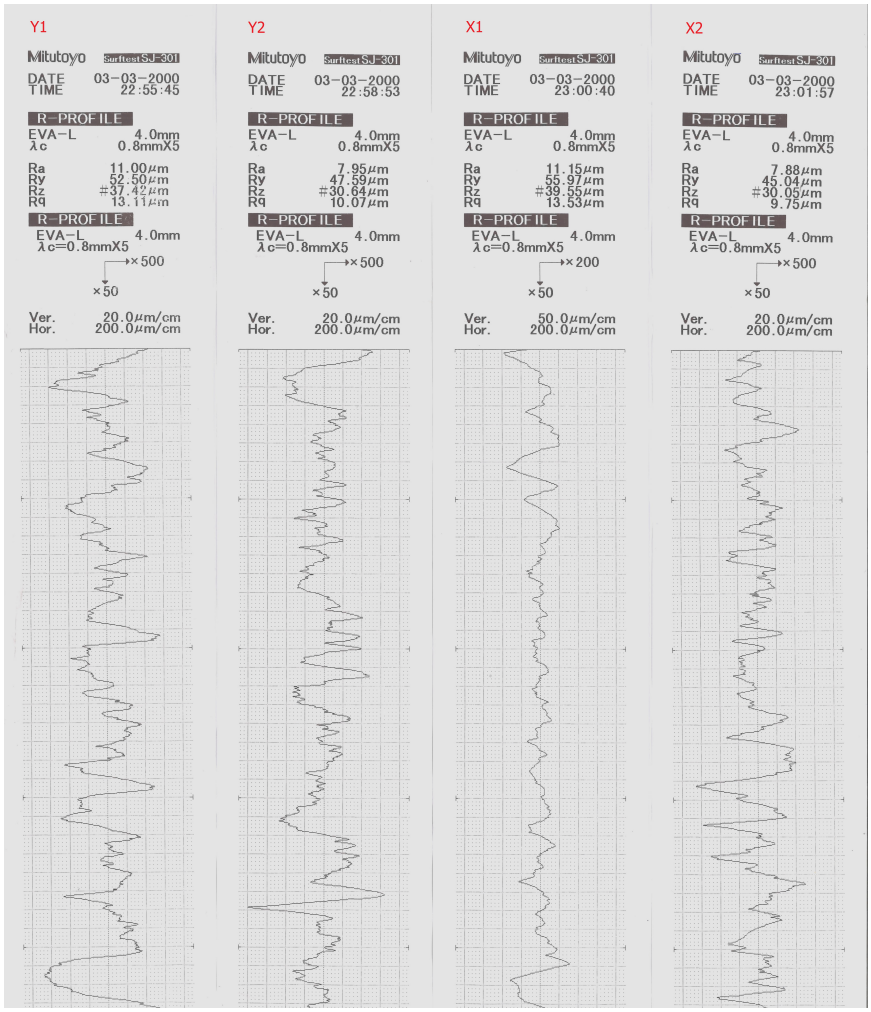

Figure C.25: Profilometer results in directions Y1, Y2, X1 and X2, as indicated in Figure C.16

C.5 Sample preparation

During the preparation of the test specimens careful attention was paid to constructing sand samples with a relative density of 80% in a layered fashion as depicted in Figure C.26. In general, the test specimens were constituted of at least two parts: the foundation (F1 and F2) and the burial (S0 - S3) layers. In the cases when burial depths greater than $3D$ were used, layers of steel plates (St1 and St2) were installed.

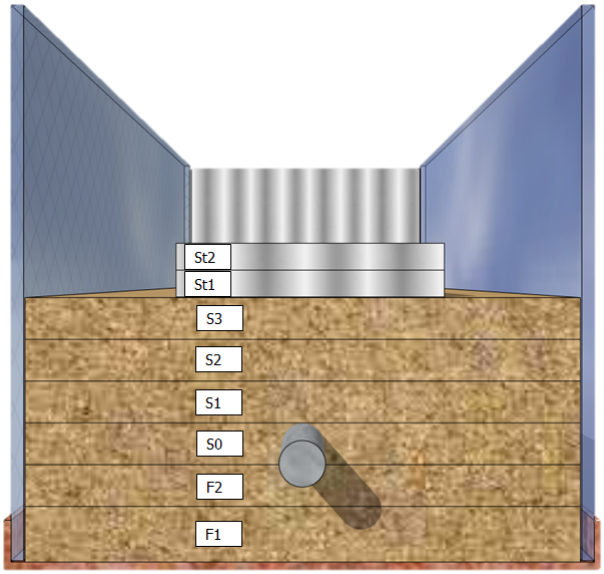

Figure C.26: Layered construction of test specimens (simulated burial depth of $10.3D$ is shown)

The full saturation of the samples was essential for simulating offshore conditions and more specifically conditions similar to the ones met during landfall operations. The method used for obtaining correct relative density was the same as the one used for the DS box tests, found in Appendix C.4.3. The constant plan area of the medium compartment in the box allowed for controlling the relative density of the specimens by the layers' height. As a consequence, guide lines were drawn on the acrylic wall which indicated the required height of each soil layer. Therefore, each soil layer was established as their exact mass was calculated in advance. The construction of the tests specimens took place with the following steps.

1. Inflow of water in the testing tank up to a height capable of covering the next soil layer
2. Careful placement of the soil mass that constitutes the first foundation layer (F1)
3. Rough levelling of the layer based on the guide line drawn on the testing tank's wall, using a scraper
4. Uniform tamping of the layer's surface until the required height is achieved
5. Fine levelling of the layer based on the guide line drawn on the testing tank's wall, using a scraper
6. Repeat tamping in case the required layer thickness was not achieved
7. Repeat steps 1-6 for the placement of the second foundation layer (F2)

8. Slide the pipe of the first compartment of the testing tank to the testing position, through the disk brush seals
9. Repeat steps 1-6 for the placement of the rest of the soil layers (S0 - S3)
10. Install layers of steel plates (St1 and St2) by slowly submerging them into the testing tank. Add water in case the water surface does not cover the steel plates

The quantity of sand required for the construction of each of the layers is included in Table C.2. This information was vital for the preparation of the test specimens and for achieving the correct relative density.

Table C.2: Layered construction - characteristics of soil layers

Layer	**Height [m]**	**Volume [L]**	**Dry mass [kg]**
F1	0.04	16.8	26.6
F2	0.03	12.6	19.9
S0	0.03	11.9	18.8
S1	0.03	12.6	19.9
S2	0.03	12.6	19.9
S3	0.03	12.6	19.9
St1	0.02	-	-
St2	0.02	-	-
Total	0.23	79.1	125.1

Figure C.27: Tamper used for compaction of the sand layers [23]

The tamper used for preparing the physical models is depicted in Figure C.27. It is constituted of a steel disk of a diameter of 0.06 m connected with a 1 m long rod. The surface of the tamper was perforated for allowing the water to flow during the tamping process and therefore avoid the development of excess pore pressures in the sand samples.

Appendix D

Physical modelling - results

D.1 Force - Time results

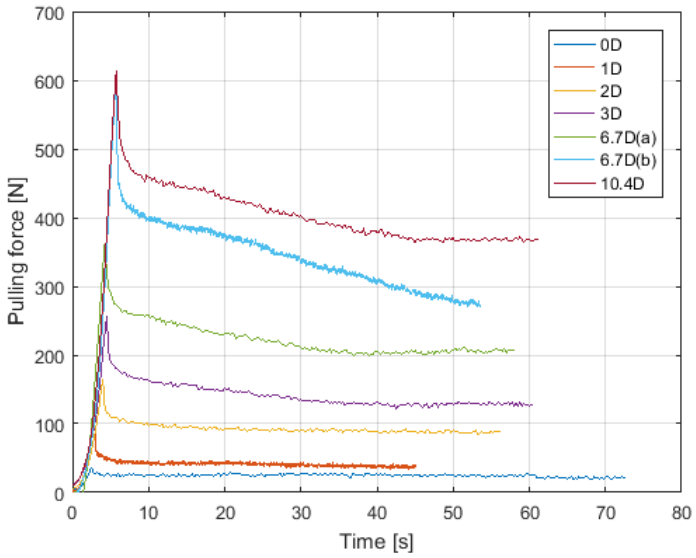

Figure D.1: Pulling force with respect to time, $v_{pull} = 1$ cm/s

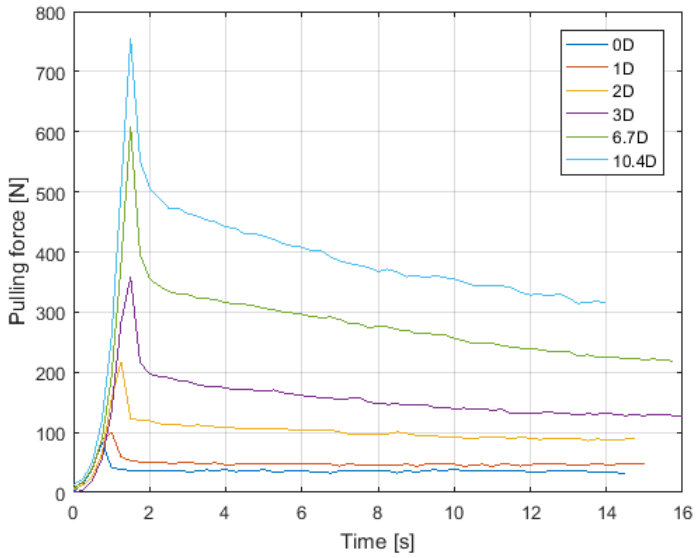

Figure D.2: Pulling force with respect to time, $v_{pull} = 4$ cm/s

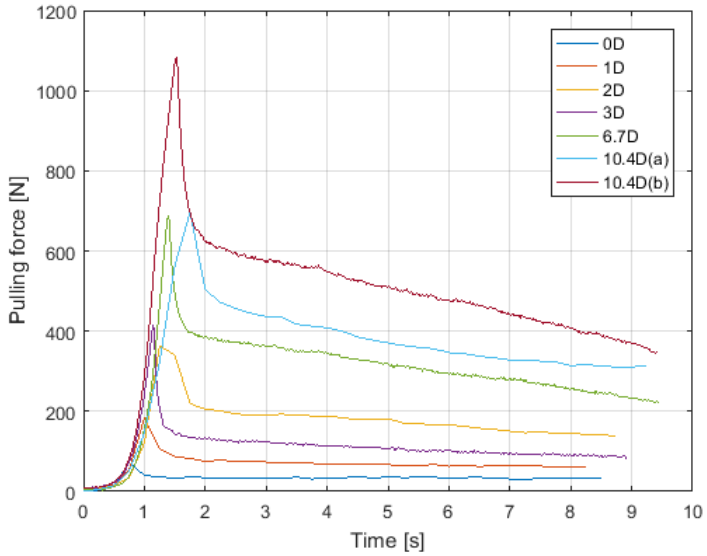

Figure D.3: Pulling force with respect to time, $v_{pull} = 7$ cm/s

D.2 Pore pressures - Time results

D.2.1 Pulling velocity = 1 cm/s

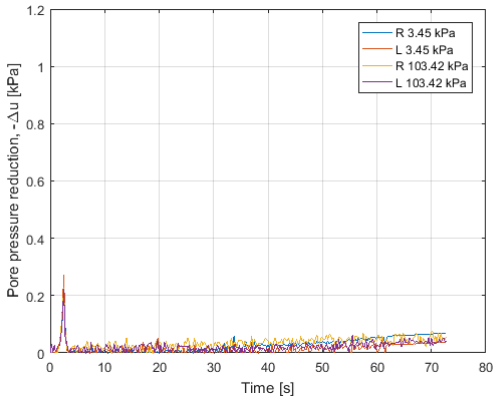

Figure D.4: Pore pressure reduction with respect to time, $d/D = 0$

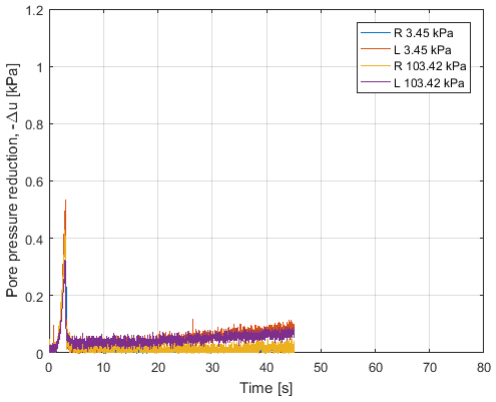

Figure D.5: Pore pressure reduction with respect to time, $d/D = 1$

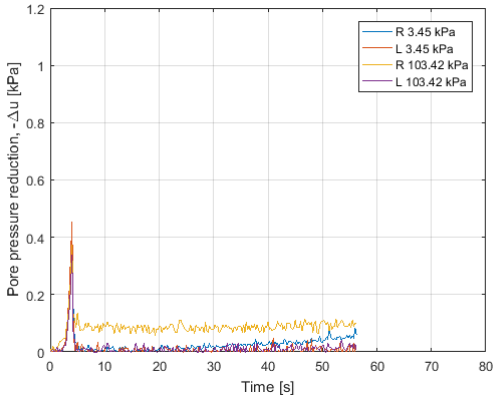

Figure D.6: Pore pressure reduction with respect to time, $d/D = 2$

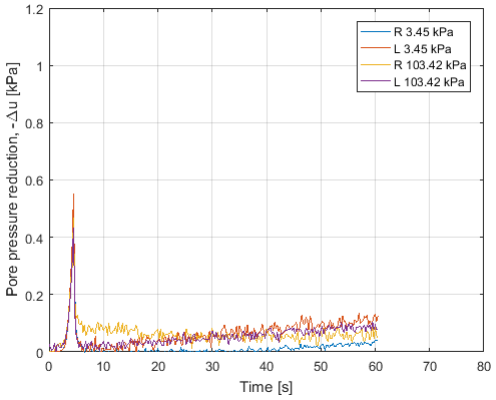

Figure D.7: Pore pressure reduction with respect to time, $d/D = 3$

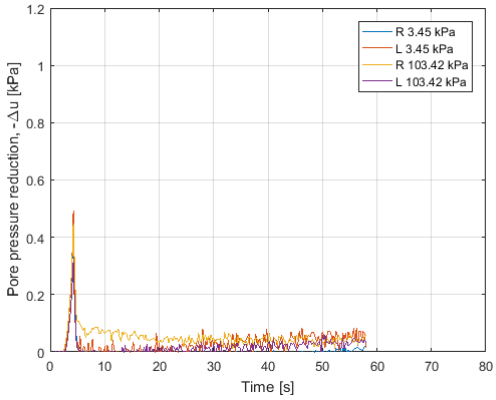

Figure D.8: Pore pressure reduction with respect to time, $d/D = 6.7$ (1^{st} trial)

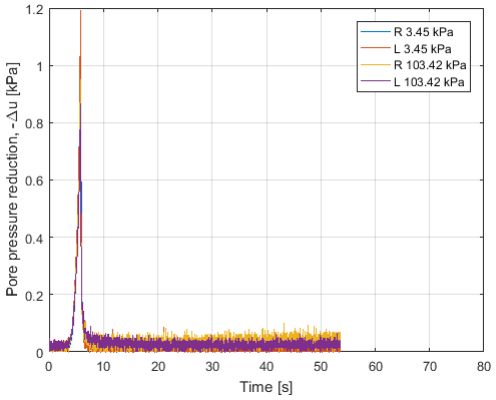

Figure D.9: Pore pressure reduction with respect to time, $d/D = 6.7$ (2^{nd} trial)

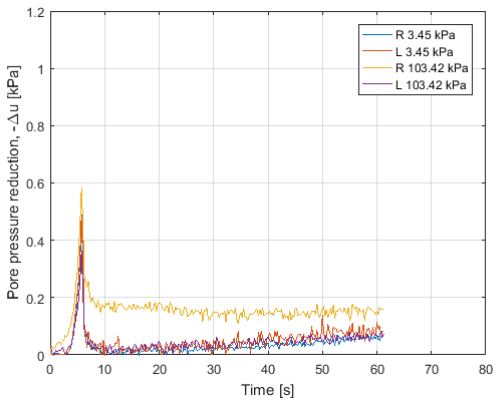

Figure D.10: Pore pressure reduction with respect to time, $d/D = 10.4$

D.2.2 Pulling velocity = 4 cm/s

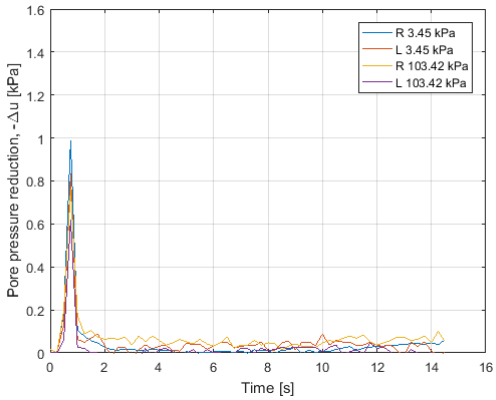

Figure D.11: Pore pressure reduction with respect to time, $d/D = 0$

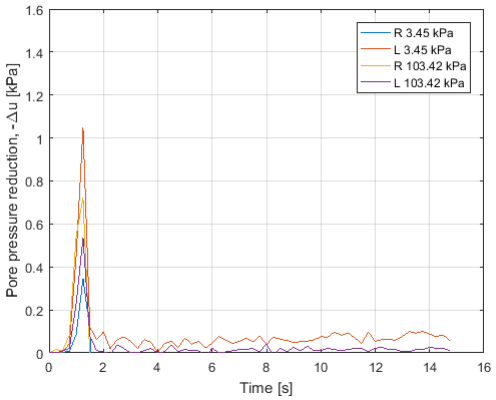

Figure D.12: Pore pressure reduction with respect to time, $d/D = 1$

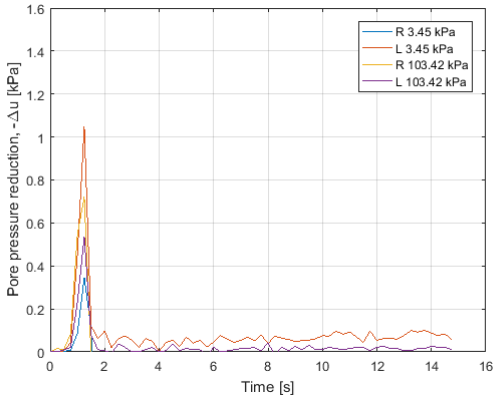

Figure D.13: Pore pressure reduction with respect to time, $d/D = 2$

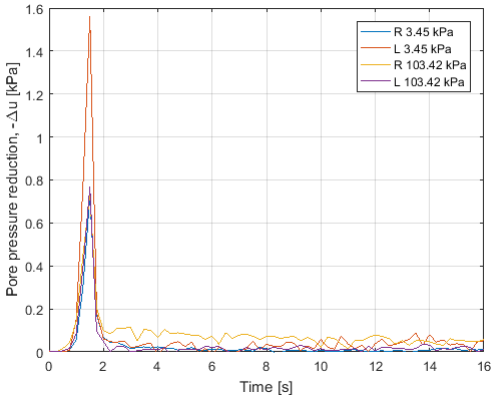

Figure D.14: Pore pressure reduction with respect to time, $d/D = 3$

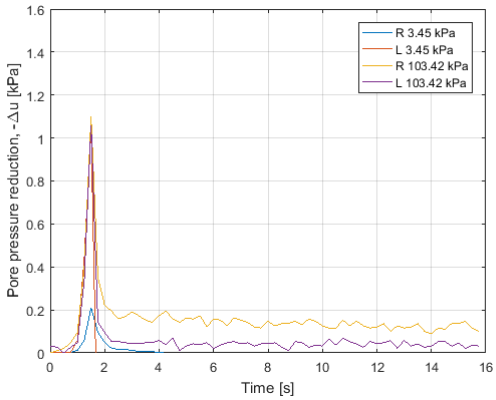

Figure D.15: Pore pressure reduction with respect to time, $d/D = 6.7$

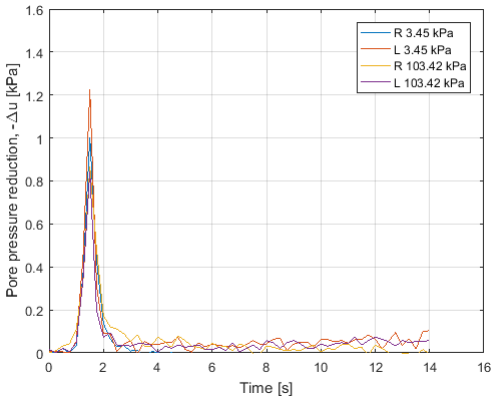

Figure D.16: Pore pressure reduction with respect to time, $d/D = 10.4$

D.2.3 Pulling velocity = 7 cm/s

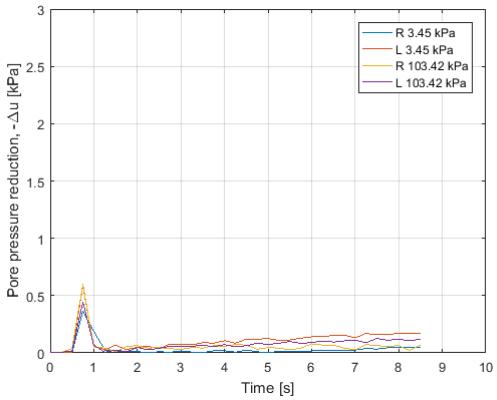

Figure D.17: Pore pressure reduction with respect to time, $d/D = 0$

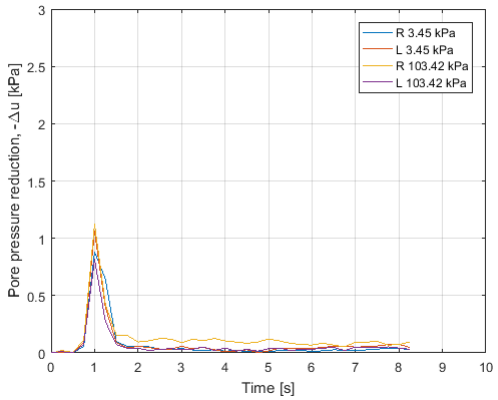

Figure D.18: Pore pressure reduction with respect to time, $d/D = 1$

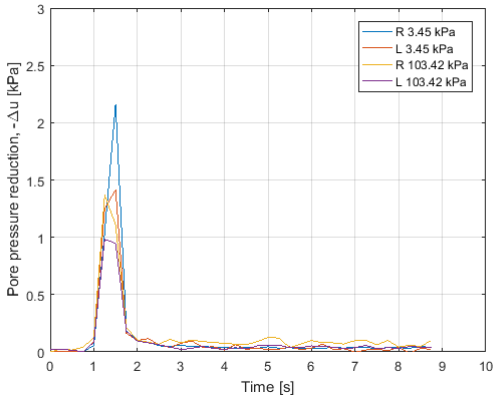

Figure D.19: Pore pressure reduction with respect to time, $d/D = 2$

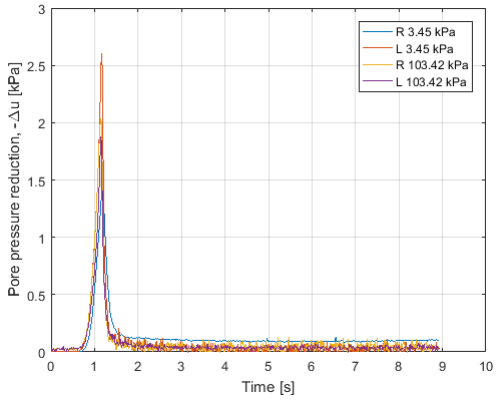

Figure D.20: Pore pressure reduction with respect to time, $d/D = 3$

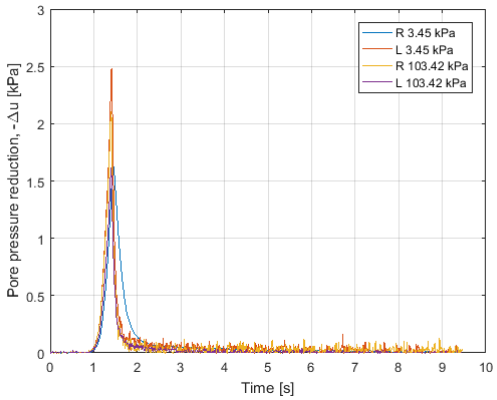

Figure D.21: Pore pressure reduction with respect to time, $d/D = 6.7$

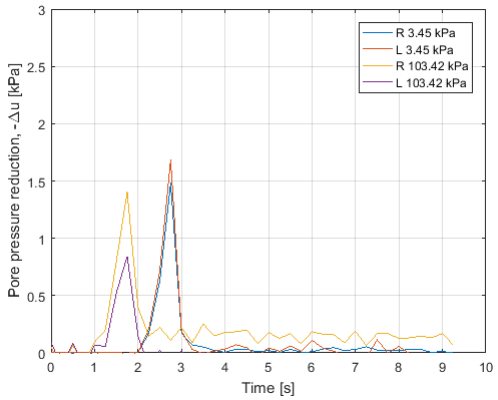

Figure D.22: Pore pressure reduction with respect to time, $d/D = 10.4$ (1^{st} trial)

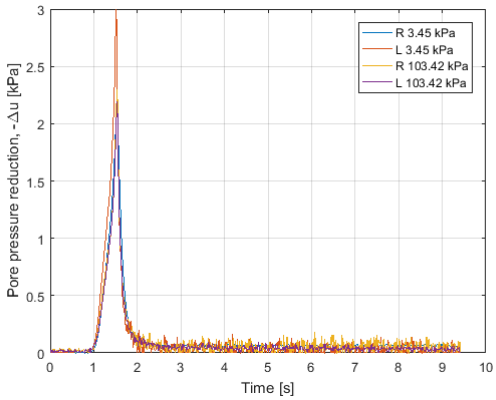

Figure D.23: Pore pressure reduction with respect to time, $d/D = 10.4$ (2^{nd} trial)

D.3 Peak pore pressure reduction - Burial depth

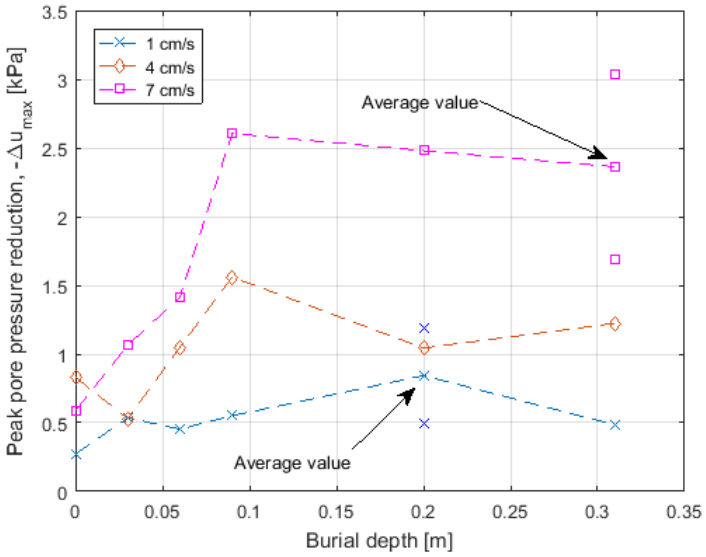

Figure D.24: Peak pore pressure reduction, sensor: L 3.45 kPa (dashed lines are linear interpolations)

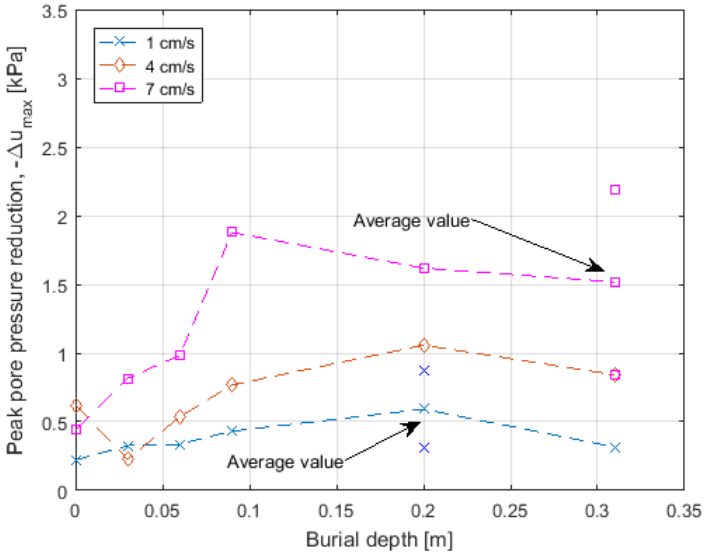

Figure D.25: Peak pore pressure reduction, sensor: L 103.42 kPa (dashed lines are linear interpolations)

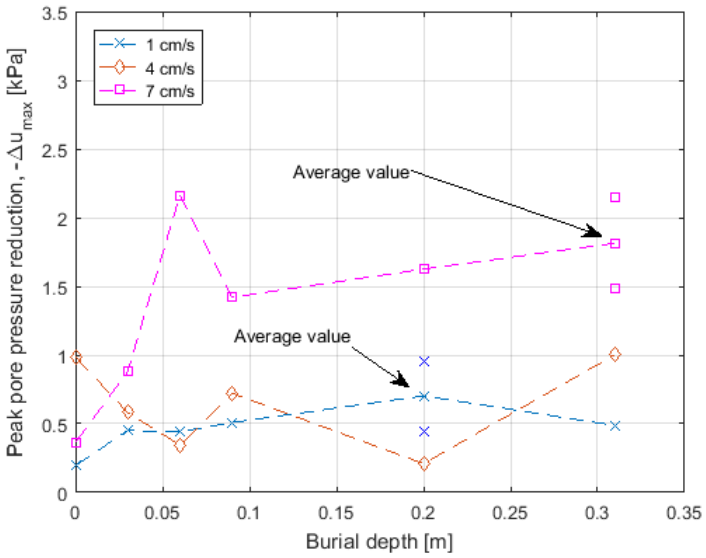

Figure D.26: Peak pore pressure reduction, sensor: R 3.45 kPa (dashed lines are linear interpolations)

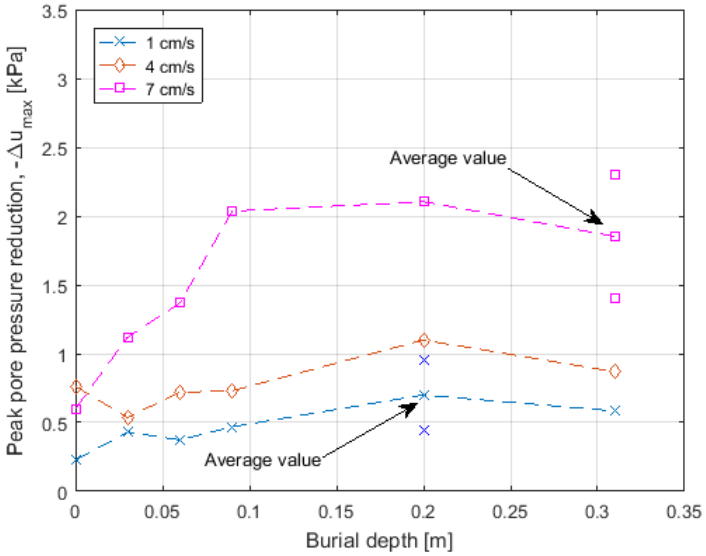

Figure D.27: Peak pore pressure reduction, sensor: R 103.42 kPa (dashed lines are linear interpolations)